Radiative Transfer in Very Strong Magnetic Fields

Thesis by

Michael Coleman Miller

In Partial Fulfillment of the Requirements

for the Degree of

Doctor of Philosophy

California Institute of Technology

Pasadena, California

1990

(Submitted May 22, 1990)

Acknowledgements

I owe a great debt to my advisor, Sterl Phinney, for his guidance and willingness to discuss any physics topic with me. By his example, I have been taught the way of research and the value of careful analysis. He has patiently corrected errors in my reasoning, suggested new avenues of research and helped me gradually become independent. He has been an invaluable resource and I hope that in some small way I may be able to emulate his style of physics.

A seminar course on neutron star physics taught by Peter Goldreich was responsible for a rekindling of my enthusiasm for the subject, and it reminded me of the usefulness of order-of-magnitude estimates.

There have been many people in the Theoretical Astrophysics group with whom I have had valuable discussions. Roger Blandford, Robert Emmering, Isaac Shlosman and Omer Blaes were all willing to field my questions, and they have contributed enormously to my academic development. In addition, I am proud to have had Paolo Coppi as both a friend and as about the best system manager one could ask for.

Financial support has been provided by the National Science Foundation, by some teaching assistantships and by research assistantships from Sterl.

An important factor in my survival at Caltech has been the friends whose humor and conversation have kept me sane through otherwise difficult times. Bob Walker, Mike Hoenk, Phil Haubert, Dan Ashlock and Mark Looper have all allowed me to expand my horizons and genuinely enjoy myself, and my discussions with Mark (whether philosophical or scatalogical) have always provided me with new insights. Donna Driscoll has not only been an excellent physics coordinator, she has frequently played the role of amateur psychologist. I am also grateful to

Kirsten Lewis, who has always believed in me even when I didn't and when things were going badly.

My parents, Lincoln and JoAnne Miller, have been more than mentors; they have been the best of friends. Whether I have needed support or prodding, they have given it. Their guidance has been invaluable and I hope that we can remain close. This thesis is dedicated to them.

Abstract

The study of the cooling of neutron stars has been undertaken by many researchers in the past twenty-five years, but this study has been made difficult by the inherent theoretical and observational uncertainties; most observations of their thermal X-ray flux have yielded only upper limits. More sensitive satellites such as ROSAT and AXAF may provide more positive flux information, and it is important to know how to interpret these data in terms of surface temperature. One of the most important factors in this interpretation is the effect of the surface magnetic field.

Young neutron stars are believed to have extremely strong magnetic fields, on the order of 10^{12}G. These fields dominate the physics of the atmosphere. In particular, atoms in the atmospheres of neutron stars have much greater binding energies than in the zero-field case, and they are constrained to move along the field lines. We use a multiconfigurational Hartree-Fock code, modified for very strong magnetic fields, to calculate wavefunctions, energies and oscillator strengths for several atoms in representative values of the magnetic field.

We then use these simulations to construct model atmospheres for neutron stars. Because of the low mass necessary for optical depth unity in the soft X-rays (typically $\approx 10^{14}\mathrm{g} \approx 10^{-19} M_{\odot}$) and because of the short time scale for gravitational separation ($\sim 1 - 100$s), the photosphere is likely to consist of a pure element. Numerous processes could cause many elements to be important, so we investigate atmospheres consisting of pure hydrogen, helium, carbon, nitrogen and silicon in magnetic fields of 9.4×10^{11}G, 2.35×10^{12}G, and 4.7×10^{12}G.

We also use the high-field energies to investigate soft X-ray lines in gamma-ray bursts. Highly ionized elements could create absorption lines in the 1-15keV range, and the identification of such lines in conjunction with cyclotron lines would

determine the magnetic field and gravitational redshift on the surface of the star, which would provide clues to the equation of state on the interior. We conclude with a discussion of the prospect of identifying these lines with future satellites.

Contents

List of Tables

List of Figures

Introduction

This thesis deals with some aspects of stars with magnetic fields high enough to modify the atomic physics in their atmospheres, which is to say white dwarfs and neutron stars. In order to give motivation for this work, it is appropriate to review the relevant properties of these objects, starting with a summary of their history.

1.1 History of compact objects

In 1915 W. S. Adams made the discovery that though Sirius B has very low luminosity, it has a color temperature of about $T = 8000$K, or roughly the same as Sirius A. This led him to the conclusion that since luminosity goes as $L \sim R^2T^4$, the radius of Sirius B must be $R < 20000$km! Since its mass had already been deduced to be about $0.75-0.95M_\odot$, where $M_\odot$ is a solar mass, this meant that its density was orders of magnitude greater than anything before observed. Because of their small size and high surface temperature, stars like Sirius B were called "white dwarfs." The puzzle of what was holding the star up against gravity was solved by Fowler (1926) with the development of Fermi-Dirac statistics; white dwarfs are supported by electron degeneracy pressure. In 1931 Chandrasekhar made the discovery that according to the laws of quantum mechanics, there existed a maximum mass for stable white dwarfs, which he calculated to be about $1.4M_\odot$. When the neutron was discovered, it was realized by Landau and others that conceivably another class of compact objects could exist, supported by neutron degeneracy pressure. These "neutron stars" would have radii of only 10km and densities of 10^{14}g/cm^3! In 1934 Baade and Zwicky made the suggestion that supernovae represented the transition from normal stars to neutron stars, and in 1939 Oppenheimer and Volkoff made calculations of neutron star models, but in general there was little theoretical interest in neutron stars for thirty years after their conceptual discovery.

The discovery of quasars in 1963 generated some interest in neutron stars as a possible source of the high redshift, but it became apparent that the redshifts were too large to be accounted for in this way. There was also a flurry of activity caused by the observation of non-solar cosmic X-ray sources, but the real frenzy was initiated by the Bell's discovery of pulsars in 1967 (Hewish *et al.* 1968). It quickly became obvious that the only known objects that could account for the properties of pulsars were rotating neutron stars (see Section 1.3). X-ray and gamma-ray bursters are also most easily explained by neutron star models, and in the past 20+ years there have been innumerable papers written about the observational and theoretical aspects of neutron stars. The launches of GRO, ROSAT and AXAF will continue to help us understand the properties of matter in this bizarre state.

1.2 The structure of neutron stars

Because of experimental and theoretical uncertainty of the equation of state of matter at post-nuclear densities, the maximum mass of a neutron star, how their radius varies with mass, and so on, are still matters of debate. However, the general structure is illustrated by Figure 1, which is taken from Shapiro and Teukolsky (1983) and shows two representative equations of state. We may say with fair confidence that the maximum mass of a neutron star is in the range $M_{\rm max} \sim 1 - 3M_{\odot}$, the radius is between 6km$< R <$20km, the magnetic field goes between $< 10^8$G and 10^{13}G, and the rotation period has a minimum of $\sim 10^{-3}$s. We will now look at the qualitative structure of neutron stars.

The surface of neutron stars, which is where this thesis has relevance, is at a density of $\rho < 1{\rm g/cm}^3$ and is gaseous. It was thought that perhaps the matter might be arranged in linear chains along the magnetic field, but recent calculations (Jones 1986; Neuhauser, Langanke and Koonin 1987) have demonstrated that the gaseous phase was energetically favorable. Because the surface gravity is so high

($g \sim 3 \times 10^{14}$ cm/s^2), the atoms on the surface are quickly stratified by density to form layers of very pure elements.

Farther down in the neutron star, at $10^6 \mathrm{g/cm^3} < \rho < 4.3 \times 10^{11} \mathrm{g/cm^3}$, the crust is solid. Here the star is held up by electron degeneracy pressure, which becomes relativistic at a few$\times 10^8 \mathrm{g/cm^3}$. Because the nuclei are in β-equilibrium with the electrons, the equilibrium nucleus changes as a function of pressure. Though the calculations of this quantity are uncertain, it is clear that as the pressure increases, so does the equilibrium value of $\frac{A}{Z}$. Thus, for example, the crust may be dominated by ^{56}Fe at low pressures. Moving deeper, to higher pressures, heavier nuclei dominate, ^{62}Ni, ^{64}Ni and so on to something like ^{118}Kr near $\rho = 4.3 \times 10^{11} \mathrm{g/cm^3}$. At this density, neutrons in the nucleus and free neutrons exist in equilibrium with each other, and the star is said to have reached the neutron drip point.

In the inner crust, where $4.3 \times 10^{11} \mathrm{g/cm^3} < \rho < 2 \times 10^{14} \mathrm{g/cm^3}$, neutron-rich nuclei exist together with an electron gas and a superfluid neutron gas. The superfluid transition temperature for the neutron gas is thought to be around 10^9K, so the gas settles into a superfluid state very soon after the creation of the neutron star (see Section 1.7). At densities higher than $\rho \approx 4 \times 10^{12} \mathrm{g/cm^3}$, the neutrons provide more pressure than the electrons, and the star may be considered to be a giant nucleus in the limit of very high density.

In the outer core, at $2 \times 10^{14} \mathrm{g/cm^3} < \rho < \rho_{\mathrm{core}}$, where ρ_{core} is the density at the center of the star, superconducting protons exist along with superfluid neutrons and normal electrons. In some models, this state extends all the way to the core.

The composition of the core is model-dependent. For "stiff" equations of state, where the pressure is a strong function of density, the maximum mass is higher, the radius is larger, the crust is thicker, and the central density is lower than for a neutron star with a "soft" equation of state. If the central density is much larger than nuclear density, where $\rho_{\mathrm{nuc}} = 2.8 \times 10^{14} \mathrm{g/cm^3}$, there may be a transition to

a different state of matter. Some possible candidates are a neutron solid, quark matter, pion condensates, or strange matter. This would have observable effects; for example, pion condensates would contract neutron stars and lower $M_{\max}$, and the presence of a different type of matter could speed up the cooling of the star (see Section 1.7). The true equation of state may be difficult to determine, because the interior composition may be determined only indirectly.

1.3 Evidence for the existence of neutron stars

Because neutron stars are so small, they have extremely low luminosities and any observation of their thermal emission is difficult (though X-ray observations of them may be possible with satellites such as ROSAT or AXAF). For example, only about $\sim 4 \times 10^{-3}$ counts/s are observed from the supernova remnant RCW 103 in the HRI detector of *Einstein* (Tuohy and Garmire 1980). Thus the observational evidence for neutron stars is based on non-thermal phenomena such as pulsars (radio and X-ray) and gamma-ray bursts.

In 1967 Pacini realized that a neutron star which had its magnetic field misaligned with its rotation axis would emit substantial radiation. Later that same year, but completely independently, Bell observed sources of regular radio pulses and the study of pulsars was born. The properties of pulsars that point to their neutron star origin are as follows:

They have periods between 1.6ms and 4.3s.

Their periods increase slowly with time, except for sharp decreases in period called "glitches."

They are stable, so much so that over long periods some pulsars are better clocks than the best atomic clocks.

Three mechanisms suggest themselves for periodic emission: rotation, pulsation, and binary orbits. Since a light travel time of 1.6ms indicates a distance of 500km,

this is the limit on the size of the emitting region. This is far too small for a main-sequence star, so it must be a white dwarf, neutron star or black hole. It is difficult to imagine how a black hole would have sufficient structure in its magnetosphere (or whatever was doing the radiating) to produce the regular, well-defined pulses seen from pulsars. We therefore turn our attention to white dwarfs and neutron stars.

A rotating sphere will break up when the centrifugal acceleration at the surface is roughly equal to the gravitational acceleration:

$$\Omega^2 R \sim \frac{GM}{R^2}, \tag{1}$$

or

$$\Omega \sim \sqrt{G\rho}. \tag{2}$$

Since the maximum density of a white dwarf is about $10^8 \mathrm{g/cm}^3$, this gives a period of $P = \frac{2\pi}{\Omega} \sim 1\mathrm{s}$. This is too long to account for the shorter-period pulsars. An estimate for pulsating white dwarfs gives roughly the same value, and since white dwarfs in a binary system must have $R > R_{\mathrm{WD}}$, this cannot explain the short periods either. Pulsating neutron stars have periods of order $10^{-3}\mathrm{s}$, but this does not explain the longer-period pulsars. Also, the pulsations will not be stable enough to account for the observations. Neutron stars in binary systems may have their parameters adjusted to give periods between $10^{-3}\mathrm{s}$ and 4s, but the system's lifetime against gravitational radiation would be

$$\tau \sim 10^{-3}\mathrm{yr} \left(\frac{P}{1\mathrm{s}}\right)^{8/3} \tag{3}$$

(which is obviously far too short), and the period would decrease as a function of time. We are therefore left with a rotating neutron star model, which can account for all observations.

Given this hypothesis, we may deduce some properties of neutron stars. If the pulsar spins down by magnetic dipole torque, then the surface magnetic field is given by

$$B_{12} \approx (P\dot{P}_{-15})^{-1/2}\mathrm{G}, \tag{4}$$

(Gunn and Ostriker 1970), where $\dot{P}$ is expressed in units of $10^{-15}\mathrm{ss}^{-1}$ and B_{12} is the magnetic field measured in units of 10^{12}G. Using this formula, we find that many pulsars have fields in excess of $B = 10^{12}$G, and this has received some confirmation by the observation of what appear to be cyclotron lines in X-ray pulsars. The mass of binary pulsars such as 1913+16 (which is probably two neutron stars) may be estimated from Doppler shifts, and turns out to be about $1.4M_{\odot}$ each, which means that the equation of state cannot be too soft. Further information may be gleaned from the properties of pulses (such as their angular diameter, energy, spectral characteristics, etc.), which then give clues about the neutron star and its magnetic field and magnetosphere.

Another class of objects that is probably related to neutron stars is the X-ray pulsars. These have periods between 0.1s and 1000s and have spectral features in the 2-20keV range, and two of them have cyclotron lines at about 10keV, corresponding to a magnetic field of about 10^{12}G. These objects, along with X-ray bursters, are fairly well modeled by a neutron star in a binary orbit around a main-sequence companion or a dwarf. However, there is still much theoretical uncertainty about the exact process of accretion and how it translates into the observed spectrum.

Gamma-ray bursts have several characteristics that make an association with neutron stars natural, if not unequivocal:

Their rise times are short, as little as <1ms. This requires an emission area $\sim$300km, which is consistent with neutron star dimensions.

Though diligent searches have been made, no unambiguous quiescent counterparts for the sources have been found. Thus, the non-burst luminosity is low. This

does not provide any difficulties for neutron star models, but it does put constraints on other possibilities.

Within observational error, the distribution of gamma-ray bursts on the sky has been found to be isotropic. This means that either the sources are near-galactic sources with a small scale height, or they are cosmologically distant. When GRO goes up it should resolve this by detecting a slight anisotropy, which there should be if GRB's are galactic neutron stars.

Several of the bursts have had emission features at 400-450keV (see, e.g., Golenetskii *et al.* 1986 or Mazets *et al.* 1981). These have been interpreted as redshifted electron-positron annihilation lines. This is consistent with the predicted neutron star gravitational redshift, but some people have expressed doubt about this interpretation of the lines.

Russian researchers have claimed to see cyclotron features from as much as ~20% of gamma-ray bursts at energies indicative of ~few$\times 10^{12}$G fields (Mazets *et al.* 1981). While these results have been questioned, the recent Ginga data, which show lines at 19.5keV and 39keV, seem much more solid (Murakami *et al.* 1988). However, it is somewhat worrisome that lines at the same energies have been seen in two supposedly separate bursts.

Though not all of the data are uncontroversial, on balance they appear to support the conclusion that GRB's come from neutron stars.

1.4 Supernovae as progenitors of neutron stars

Ever since Baade and Zwicky made the suggestion in 1934 that supernovae represent the transition from normal stars to neutron stars, the two objects have been considered to be closely related. However, the association may not be as intimate as was once thought. Some relatively recent observations (Helfand 1983) have indicated that although all compact X-ray sources in supernova remnants

(SNRs) are associated with observable pulsars, only about 20% of SNRs have a compact X-ray source. If it is assumed that about 50% of supernovae are Type I (accretion- induced nuclear runaway on a white dwarf, which should leave no remnant), then only 40% of Type IIs produce neutron stars. If the birth rate of pulsars is the same as the rate of supernovae, this may mean that another, quiescent mechanism exists for the production of neutron stars.

Regardless of this, a supernova origin for neutron stars would explain some of their properties, and in the rest of this introduction we will implicitly assume that neutron stars are produced by supernovae. One hypothesis about the origin of the spin rate of a neutron star starts from the observation that many of the stars that become Type II supernovae (O and B stars) are rotating near break-up velocity. For typical masses and radii of O and B stars this gives a period of

$$P = \frac{2\pi}{\Omega} \sim \frac{2\pi}{\sqrt{G\rho}} \sim \text{hours.} \tag{5}$$

It is believed that just before the supernova occurs, the star consists of a white dwarf core and a hydrogen envelope extending out to several astronomical units. Since the core is primarily heavy elements such as iron, it has a much higher mean molecular weight than the envelope, and this may make it difficult for the core to transfer angular momentum to the envelope. If this is true, then the core rotates with the original period of the star, on the order of hours. When the core collapses to form a neutron star, if angular momentum is conserved, the neutron star will have a period of

$$P \sim \text{hours} \times \left(\frac{10\text{km}}{\sim 10000\text{km}}\right)^2 \sim 0.001\text{s} - 0.01\text{s}. \tag{6}$$

This estimate must be taken with a grain of salt, because it neglects possibly important effects. For example, magnetic braking has been ignored, and this could cause the initial period to be substantially higher than a few milliseconds. The

observationally deduced initial spin rate of neutron stars is somewhat uncertain. Vivekanand and Narayan (1981) suggested, on the basis of statistical analysis, that the majority of pulsars may be born with periods of a few hundred milliseconds. However, the evidence for this is by no means overwhelming and the data may be fit by initial periods less than 0.1s (Emmering and Chevalier 1989). Nonetheless, the association of neutron stars with supernovae received a boost when neutrinos were detected from SN 1987A. If a black hole had been created, no neutrinos would have been detected, so it is very likely that this event created a neutron star. We can look forward to learning a great deal about the properties of young neutron stars when the remnant clears away enough to observe this object.

1.5 The surface layers of neutron stars

This thesis deals with the thermal spectra of neutron stars, so it is important to know what the composition of the surface is. This is fairly uncertain because there are a variety of effects that may be important.

The pre-supernova structure of the progenitor star is schematically shown in Figure 2. Because of thermonuclear burning and density stratification, the core is expected to be primarily iron. We define the mass cut to be the boundary between the material that is pushed outward and that which is pushed inward in the supernova explosion. From numerical simulations we expect the mass cut to occur in the iron core (Woosley and Weaver 1986), so we might expect that the surface of neutron stars would be primarily iron. However, there are several complicating factors. There might be fall-back from the outer shells of the star, which from the diagram we see could mean that silicon, aluminum, magnesium, neon, oxygen, nitrogen, carbon, helium or hydrogen could contribute significantly. This is further muddied by the probability that there is significant mixing of the shells because of a Rayleigh-Taylor instability at the shell boundaries. Additionally, elements

with lower atomic number might be created by spallation, since the gravitational potential at the surface of a neutron star is on the order of 100MeV per nucleon.

Once the neutron star is clear of the supernova remnant, it will start to accrete from the interstellar medium (ISM). Since the ISM is primarily hydrogen, it might seem that after sufficient time hydrogen would dominate the surface. However, if neutron stars have magnetic fields in the 10^{12}G range, the accretion will be funneled to the magnetic polar caps. This material may be prevented from diffusing across field lines to the rest of the star's surface. However, if the magnetic field is initially small, then this would not be as strong an effect, and even if the star were born with very high fields, it is possible that the material could fall "between the field lines" and thus spread out over the surface of the star (see, e.g., Arons and Lea 1980).

If a sufficiently thick layer of hydrogen is built up on the surface, then low-temperature or "pycnonuclear" fusion might transform the hydrogen into helium, so that helium would be the dominant element. This could also be true of the helium→carbon reaction, or any of the other reactions in the fusion progression, or it could be that the heat generated would cause the hydrogen to fuse through to iron and we would end up with iron as the primary element again. In any case, the surface gravity of a neutron star is so large that density stratification will take place in $\sim 1 - 100$s. In addition, for the energy range considered in my papers, 10eV-10keV, only $\sim 10^{14}$g$= 10^{-19} M_\odot$ of matter is necessary for optical depth unity. Therefore, the thermal X-ray spectrum will be that of a pure element, and in my simulations I have produced model atmospheres of pure hydrogen, helium, carbon, nitrogen and silicon.

1.6 The magnetic fields of neutron stars

As was indicated before, the determination of the surface magnetic fields of neutron stars from cyclotron lines and $B_{12} = \sqrt{P\dot{P}_{-15}}$ gives fields between 10^8G and 10^{13}G. Old pulsars (determined by scale height in the galaxy) tend to have weaker fields than young pulsars, and there seems to be fairly good evidence that the magnetic field decays on a timescale of 10^7yr. However, it seems that during the time when the star might be detected as a thermal X-ray source ($\sim 10^4$yr–see Section 1.7) its magnetic field will still be fairly high. There have also been a few white dwarfs detected with fields in excess of 10^8G, so it is interesting to consider the effects of very strong magnetic fields, and in particular the effect of strong fields on atoms.

In weak fields, such as those that can be generated in laboratories, atoms may be considered to be spherical, and the magnetic field may be considered a perturbation. In this limit, energy levels of atoms are split by the Zeeman effect, so the change from the zero-field energy is

$$\Delta E = gM\frac{e\hbar B}{2mc}, \tag{7}$$

where M is the magnetic quantum number and

$$g = 1 + \frac{J(J+1) - L(L+1) + S(S+1)}{2J(J+1)} \tag{8}$$

is the Landé g factor, with J being the total angular momentum, S being the spin angular momentum and L being the orbital angular momentum. This effect has been used to measure the magnetic fields of white dwarfs, where it is useful down to a minimum of about 10^4G.

In very strong fields, atoms are cylindrical and the Coulomb force is a perturbation to the magnetic field. In this limit, the electrons are in Landau levels, and the major effect of the nucleus is along the field, where the field exerts no force. To get an idea of when these limits apply, we consider scaling arguments.

The cyclotron frequency is defined as the frequency of (circular) motion of a charged particle in a uniform magnetic field of magnitude B. The expression for the cyclotron frequency may be derived by considering the classical force balance equation

$$\frac{eBv_\phi}{c} \sim M\omega^2\rho, \tag{9}$$

where e is the electric charge, v_ϕ is the azimuthal velocity, c is the speed of light, M is the mass of the electron, ω is the frequency and ρ is the radius of the circular motion. Since $v_\phi = \omega\rho$, this gives the cyclotron frequency as

$$\omega_c = \frac{eB}{Mc} \approx 11.5\text{keV}\frac{B}{10^{12}\text{G}}. \tag{10}$$

Another interesting quantity is the scale length across the field. This may be calculated using the Bohr-Sommerfeld quantization rule

$$L_z = M\omega\rho^2 \sim m\hbar, \tag{11}$$

where $m = 0, \pm1, \pm2, \ldots$ is the azimuthal quantum number. Therefore, it follows that the radius of the mth orbital is

$$\rho_m \sim \hat{\rho}\sqrt{|m|}, \tag{12}$$

where $\hat{\rho}$ is the Landau radius,

$$\hat{\rho} = \left(\frac{\hbar c}{eB}\right)^{1/2} = 2.5 \times 10^{-10} B_{12}^{-1/2}\text{cm} \tag{13}$$

and $B_{12} \equiv \frac{B}{10^{12}\text{G}}$. A more exact expression, given by the maxima of the Landau functions, is

$$\rho_m = \hat{\rho}\sqrt{2m+1}. \tag{14}$$

We may now get an idea of the critical field at which magnetic and Coulomb effects are comparable. This occurs when the two forces are equal, so

$$\frac{Ze^2}{\rho_m^2} = \frac{ev_mB}{c} = \frac{e\omega_c\rho_mB}{c}. \tag{15}$$

Solving for B gives the critical field as

$$B_c = \frac{Z^2}{(2m+1)^3} B_0, \tag{16}$$

where B_0, the critical field for hydrogen, is

$$B_0 = \frac{M^2 c e^3}{\hbar^3} \approx 2.35 \times 10^9 \mathrm{G}. \tag{17}$$

The high-field cylindrical approximation is strictly valid for $B \gg B_c$, but may be used with reasonable accuracy whenever $B > B_c$. This means that for young neutron stars with $B > 10^{12}$G this approximation is applicable for elements up to iron (Z=26). It also means that for states with $m > 0$ and magnetic fields typical of the most magnetic white dwarfs, $B > 10^8$G, hydrogen must be treated in this limit.

The coordinate system used in the high-field limit is cylindrical, with the coordinates being ρ for the radial direction, ϕ for the azimuthal direction, and z along the field. The quantum numbers for these coordinates are, respectively, n, m and ν. Since $n > 0$ states have large energies, $E = n\hbar\omega_c \approx 11.5\mathrm{keV}nB_{12}$, we will assume that at a typical surface temperature $T = 10^5\mathrm{K} - 10^6\mathrm{K} \approx 10\mathrm{eV} - 100\mathrm{eV}$ (see Section 1.7), these levels are not excited, and $n = 0$. However, $n > 0$ states must be considered when B is smaller. For hydrogen, the ground state (m=0, ν=0) wavefunction may be modeled by a cylinder of radius $\hat{\rho}$ and length l, where l is to be determined. In this limit, the Coulomb functions have energy

$$E \sim \frac{\hbar^2}{2Ml^2} - \frac{Ze^2}{l} \ln\left(\frac{l}{\hat{\rho}}\right). \tag{18}$$

Minimization with respect to l gives

$$l \sim \left(\frac{a_0/Z\hat{\rho}}{\ln(a_0/Z\hat{\rho})}\right)\hat{\rho} \tag{19}$$

and

$$E \sim Z^2 \frac{\hbar^2}{M a_0^2} \ln^2 \left(\frac{a_0}{Z\hat{\rho}} \right)$$
$$\sim Z^2 \frac{\hbar^2}{M a_0^2} \ln^2 \left(\frac{20 B_{12}^{1/2}}{Z} \right) \quad (20)$$

where $a_0 = 5.1 \times 10^{-9}$cm is the Bohr radius. For a hydrogenic atom in a state $m = 0, \nu > 0$ it can be shown (Landau and Lifshitz 1977) that in the limit of large B, the energy of these excited states is almost constant, with

$$E_\nu \sim -Z^2 \frac{13.6\text{eV}}{((\nu+1)/2)^2}. \quad (21)$$

While this approximation and the approximation for the ground state energy are strictly valid only for hydrogenic atoms, they are fairly close to the ground and excited state energies of the outer electron of a many-electron atom (because the magnetic field breaks the degeneracy between atoms in the same orbital, there will be a unique outer electron). However, the inner electrons are subject to interelectronic forces, and in order to compute their wavefunctions and energy spectra, one needs a more complicated treatment. In the first paper of this thesis, I apply the Hartree-Fock method, modified for very strong magnetic fields, to determine the wavefunctions, energies and cross sections of interaction with photons for hydrogen, helium and carbon in the expected field strengths of neutron stars. In the second paper, I continue this work by generating energies and cross sections for hydrogen, helium, carbon, nitrogen and silicon and their ions in three magnetic fields, and in the fourth paper I investigate some of the properties of highly ionized elements in strong fields, as might be found in the polar caps of neutron stars during gamma-ray bursts.

1.7 The cooling of neutron stars

The third paper in this thesis deals with the atmospheres of neutron stars and their relevance to cooling curves of neutron stars. In order to get an idea of why it is important to consider the impact of atmospheres, it is worthwhile to outline briefly some of the theory of cooling neutron stars. The following is largely taken from Shapiro and Teukolsky (1983).

Immediately after a supernova, a neutron star will have an interior temperature in excess of 10^{11}K. It will cool down very rapidly by emission of neutrinos via the "URCA" processes:

$$n \rightarrow p + e^- + \bar{\nu}_e, \qquad e^- + p \rightarrow n + \nu_e. \tag{22}$$

These processes cool the star down to about 10^9K very quickly. However, when the nucleons become degenerate at 10^9K, the URCA reactions are suppressed because they turn out not to conserve momentum. The dominant processes then become the "modified" URCA reactions

$$\begin{aligned} n + n &\rightarrow n + p + e^- + \bar{\nu}_e, \\ n + p + e^- &\rightarrow n + n + \nu_e. \end{aligned} \tag{23}$$

For a uniform density star with no muons, the modified URCA processes give a luminosity of

$$L_\nu^{\rm URCA} = (5.3 \times 10^{39}{\rm ergs}^{-1}) \frac{M}{M_\odot} \left(\frac{\rho_{\rm nuc}}{\rho} \right)^{1/3} T_9^8, \tag{24}$$

where $\rho_{\rm nuc} = 2.8 \times 10^{14}{\rm g/cm}^3$ is the nuclear density, and T_9 is the temperature measured in units of 10^9K. This may be compared with the blackbody photon luminosity for a neutron star with radius R and effective surface temperature T_e:

$$L_\gamma = 4\pi R^2 \sigma T_e^4 = 7 \times 10^{36}{\rm ergs}^{-1} \left(\frac{R}{10{\rm km}} \right)^2 T_{e,7}^4, \tag{25}$$

where σ is the Stefan-Boltzmann constant and $T_{e,7}$ is the temperature in units of 10^7K. We see by comparing the neutrino luminosity to the photon luminosity

that neutrino emission dominates the cooling for high temperatures, while photon radiation takes over at lower temperatures. We can get an idea of the boundary temperature by substituting in the relation

$$T_e \approx 9 \times 10^5 g_{14}^{0.25} T_{i,8}^{0.55}, \tag{26}$$

where $T_{i,8}$ is the interior temperature in units of 10^8K, g_{14} is the surface gravity in units of 10^{14}cm/s^2, and this expression is a fit to the calculation of Gudmundsson, Pethick and Epstein (1983). It should be noted that the relation of interior temperature to effective temperature is one that strongly depends on the conductive opacities in the transition region. Substituting this in and equating the two luminosities, one finds that photon cooling is more important for $T_i < 10^8$K.

The assumption that the URCA and modified URCA processes and photon radiation are the only important effects in the cooling of neutron stars is called the standard cooling model. If the central density of neutron stars is not much beyond nuclear, this has a good chance of being correct. However, if at the core of neutron stars different types of matter exist, the cooling rate may be drastically modified. For example, if pion condensates exist, then there will be cooling by the decay of free pions:

$$\pi^- + n \rightarrow n + e^- + \bar{\nu}_e, \tag{27}$$

$$\pi^- + n \rightarrow n + \mu^- + \bar{\nu}_\mu, \tag{28}$$

and the inverse processes

$$n + e^- \rightarrow n + \pi^- + \nu_e, \tag{29}$$

$$n + \mu^- \rightarrow n + \pi^- + \nu_\mu. \tag{30}$$

The luminosity for these reactions has been calculated as

$$L_\nu^\pi = (1.5 \times 10^{46}\text{ergs}^{-1})\theta^2 \frac{M}{M_\odot} \frac{\rho_{\text{nuc}}}{\rho} T_9^6, \tag{31}$$

where $\theta \sim 0.3$ is an angle measuring the degree of pion condensation. Since this is much larger than the modified URCA rates, if there is a substantial amount of pion condensate in the interior, the star will cool much faster than in the standard model. Another possible effect is quark beta decay involving relativistic quarks:

$$\begin{aligned} d &\rightarrow u + e^- + \bar{\nu}_e, \\ u + e^- &\rightarrow d + \nu_e. \end{aligned} \tag{32}$$

The luminosity for a uniform density star composed of quark matter works out to be

$$L_\nu^{\text{quark}} \approx (1.3 \times 10^{44} \text{ergs}^{-1}) \frac{M}{M_\odot} T_9^6, \tag{33}$$

so if quark matter is a significant fraction of the mass of neutron stars, the cooling rate will be greatly enhanced.

Standard cooling models predict that the surface temperatures of neutron stars should remain at $T > 10^6$K for 10^4yrs (Nomoto and Tsuruta 1981). X-ray observations of hot neutron stars in supernova remnants have not provided any unambiguous detections of thermal flux, so at the present we have only upper limits on the temperatures of neutron stars. In order to interpret these negative results, it is important to consider the effects of the atmosphere of neutron stars. While an atmosphere will not significantly affect the total luminosity of the star (Hernquist 1985), it may modify the star's emission in the sensitivity ranges of X-ray detectors. In 1987 Romani generated spectra from model atmospheres using cross section data for $B = 0$ and compared them with what could be seen by the Einstein X-ray satellite in the energy range 0.5keV to 5keV. He found that if the surface were dominated by low-Z elements, the temperature inferred from the count rate in the Einstein band would be much higher than its effective surface temperature. This meant that the upper limits on surface temperature were much more stringent than previously thought, and cooling would have to take place very rapidly. In the

second paper of this thesis, model atmospheres are generated using cross sections calculated for high magnetic fields. The result is that in the sensitivity ranges of Einstein and ROSAT, the inferred blackbody temperature is roughly equal to the effective surface temperature. Therefore, we will have to wait until more sensitive X-ray satellites such as ROSAT and AXAF are launched before we can make any definitive statements about neutron star cooling.

References

Adams, W. S. 1915, *Pub. Astron. Soc. Pac.*, **27**, 236.

Arons, J., and Lea, S. M. 1976, *Ap. J.*, **235**, 1016.

Baade, W., and Zwicky, F. 1934, *Phys. Rev.*, **45**, 138.

Blandford, R. D., Applegate, J. H., and Hernquist, L. 1983, *Mon. Not. R. astr. Soc.*, **204**, 1025.

Chandrasekhar, S. 1931, *Ap. J.*, **74**, 81.

Emmering, R. T., and Chevalier, R. A. 1989, *Ap. J.*, **345**, 931.

Fowler, R. H. 1926, *Mon. Not. R. astr. Soc.*, **87**, 114.

Golenetskii, S. V., Guryan, Yu. a., Dumov, G. B., Dyatchkov, A. V. *et al.* 1986. Preprint 1026, Fiz. Tekh. Inst. Ioffe, 31pp. Leningrad: Akad. Nauk SSSR.

Gudmundsson, E. H., Pethick, C. J., and Epstein, R. I. 1983, *Ap. J.*, **272**, 286.

Gunn, J. E., and Ostriker, J. P. 1970, *Ap. J.*, **160**, 979.

Helfand, D. J. 1983, *Supernova Remnants and Their X-ray Emission*, ed. J. Danziger and P. Gorenstein (Dordrecht: Reidel), p. 471.

Hernquist, L. 1985, *Mon. Not. R. astr. Soc.*, **213**, 313.

Hewish, A., Bell, S. J., Pilkington, J. D. H., Scott, P. F., and Collins, R. A. 1968, *Nature*, **217**, 709.

Jones, P. B. 1986, *Mon. Not. R. astr. Soc.*, **218**, 477.

Landau, L. D., and Lifshitz, E. M. 1977, *Quantum Mechanics: Non-Relativistic Theory*, 3rd ed., (New York: Pergamon, Elmsford).

Mazets, E. P., Golenetskii, S. V., Aptekar, R. L., Guryan, Yu. A., and Illinskii, V. N. 1981, *Nature*, **290**, 378.

Murakami, T. *et al.* 1988, *Nature*, **335**, 234.

Neuhauser, D., Langanke, K., and Koonin, S. E. 1987, *Phys. Rev. A*, **33**, 2084.

Nomoto, K., and Tsuruta, S. 1981, *Ap. J. (Letters)*, **250**, L19.

Oppenheimer, J. R., and Volkoff, G. M. 1939, *Phys. Rev.*, **55**, 374.

Pacini, F. 1967, *Nature*, **216**, 567.

Shapiro, S. L., and Teukolsky, S. A. 1983, *Black Holes, White Dwarfs and Neutron Stars* (Wiley:New York).

Tsuruta, S. 1979, *Phys. Rept.*, **56**, 237.

Tuohy, I., and Garmire, G. 1980, *Ap. J. (Letters)*, **239**, L107.

Vivekanand, M., and Narayan, R. 1981, *J. Ap. Astr.*, *2*, 315.

Woosley, S. E., and Weaver, T. A. 1986, *Ann. Rev. Astron. Astrophys.*, **24**, 205.

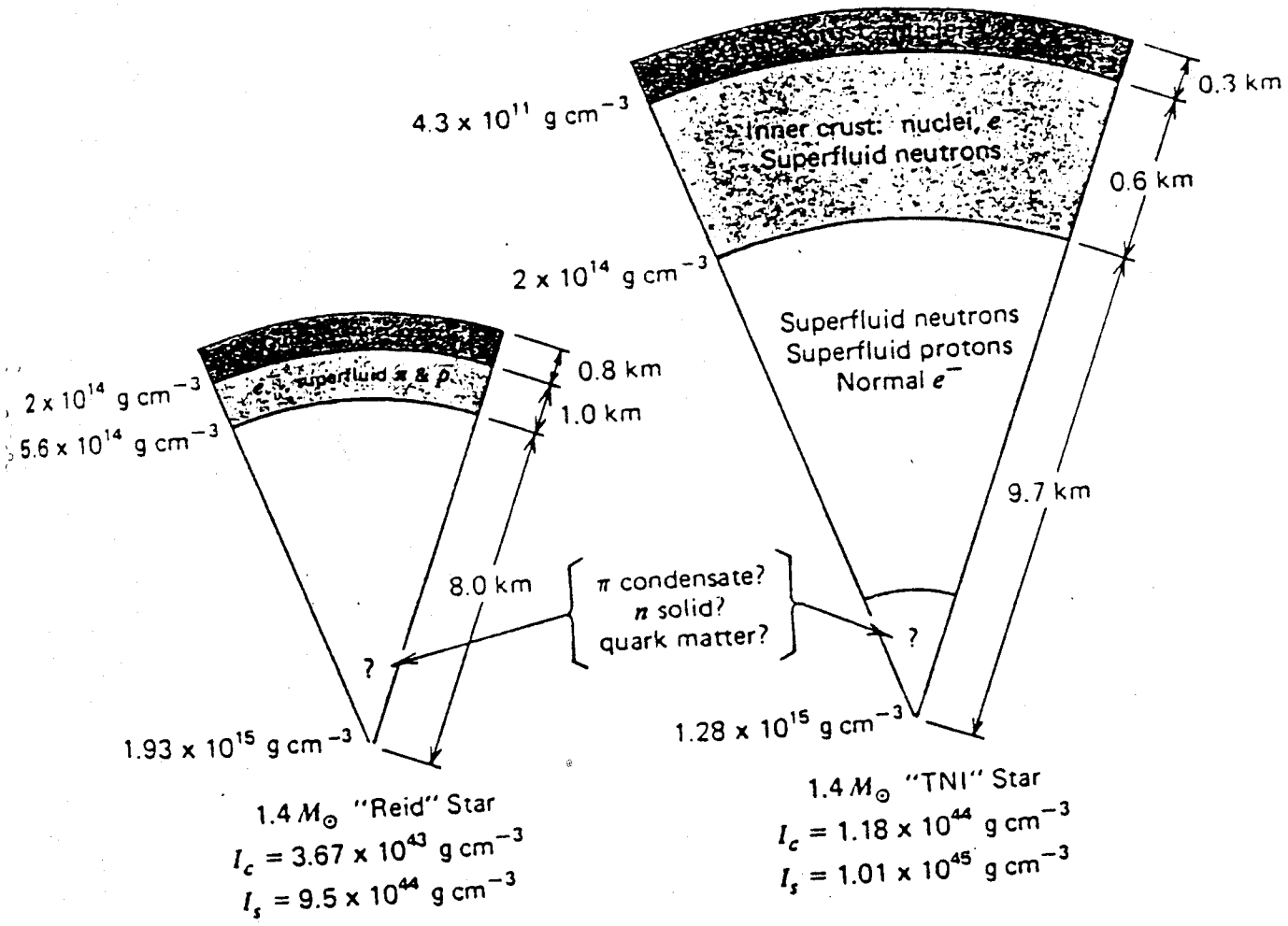
Outer crust: nuclei, e
Inner crust: nuclei, e
Superfluid neutrons
4.3 x 10^11 g cm^-3
0.3 km
0.6 km
2 x 10^14 g cm^-3
Superfluid neutrons
Superfluid protons
Normal e^-
9.7 km
2 x 10^14 g cm^-3
5.6 x 10^14 g cm^-3
e, superfluid n & p
0.8 km
1.0 km
8.0 km
π condensate?
n solid?
quark matter?
?
?
1.93 x 10^15 g cm^-3
1.28 x 10^15 g cm^-3
1.4 M⊙ "Reid" Star
I_c = 3.67 x 10^43 g cm^-3
I_s = 9.5 x 10^44 g cm^-3
1.4 M⊙ "TNI" Star
I_c = 1.18 x 10^44 g cm^-3
I_s = 1.01 x 10^45 g cm^-3

Figure 1

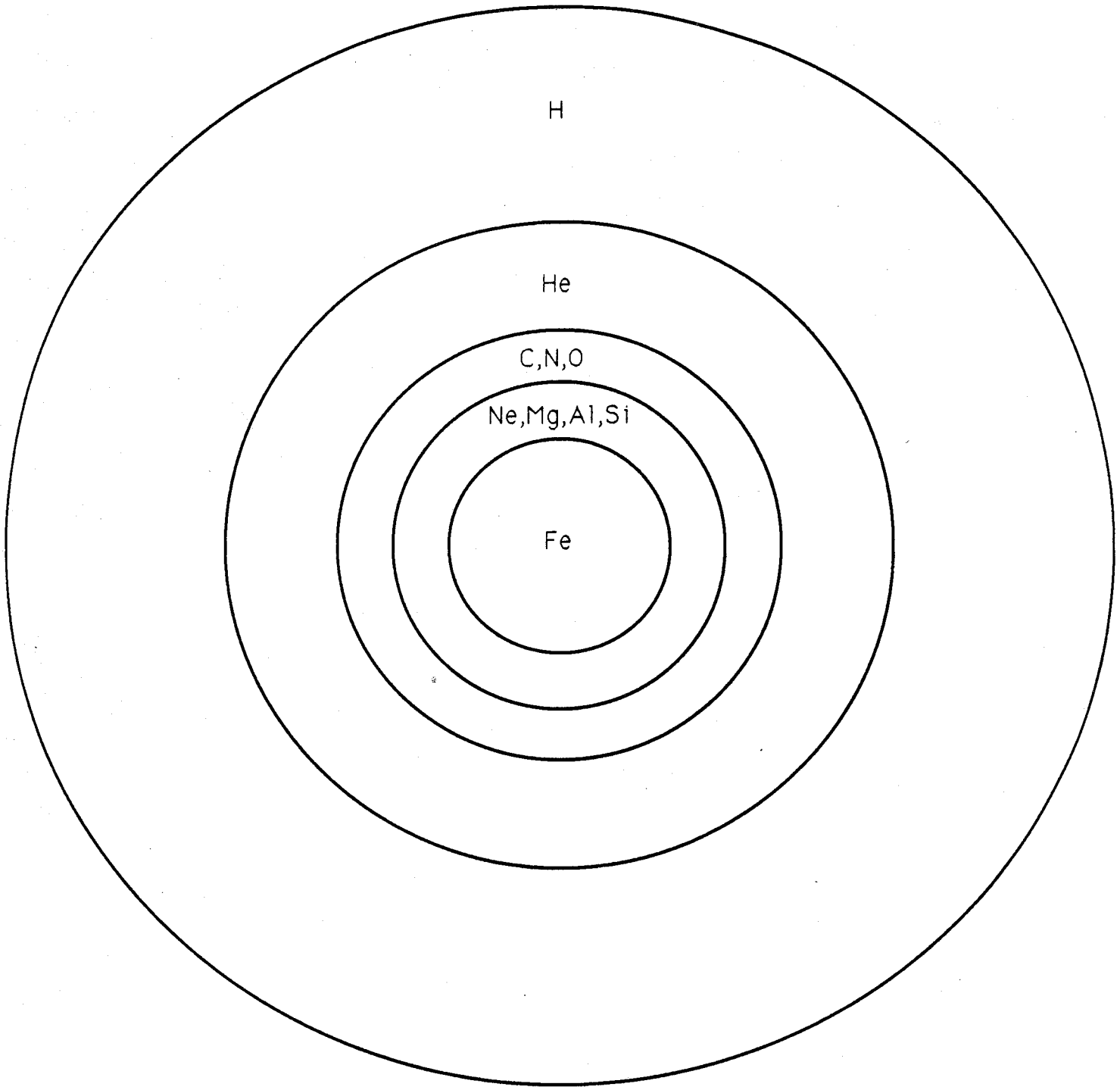

Figure 2

Chapter 1: Atoms in Very Strong Magnetic Fields

M. C. Miller†and D. Neuhauser‡

†Theoretical Astrophysics, California Institute of Technology, Pasadena, California 91125 USA

‡W. K. Kellogg Radiation Laboratory, California Institute of Technology, Pasadena, California 91125 USA

Abstract. The X-ray spectra of neutron stars are expected to be determined by the opacities of atoms with $Z > 2$ in strong magnetic fields. We calculate the energy levels, wavefunctions and transition rates of hydrogen, helium and carbon in the very strong ($B > 4.7 \times 10^9 Z^2$G) magnetic fields expected in neutron stars. The wavefunctions are represented in terms of Landau states, and are calculated with a high-field multiconfigurational Hartree-Fock code. We compare our results for hydrogen with previous work and use our wavefunctions to compute bound-bound and bound-free oscillator strengths for heavier elements. The techniques developed here can be extended to elements heavier than carbon.

1. Introduction

The existence of sensitive, imaging X-ray satellites has made the detection of thermal flux from neutron stars a realistic possibility. Recent research (see Tsuruta 1986 for a review) has indicated that the effective surface temperature of neutron stars should remain above $\approx 10^5$K=10eV for 10^5 yrs, barring the presence of pion condensates or other exotic matter. The star should remain a detectable X-ray source during that period. While white dwarfs have magnetic fields B small enough ($B < 5 \times 10^8$G) that energy levels may be computed by perturbation theory (Zeeman splittings) with errors of <2%, observed neutron stars typically have fields in the range of 10^9 to 5×10^{12}G (Taylor and Stinebring 1986, Joss and Rappaport 1984), so that the magnetic interaction may no longer be treated as a perturbation, and atomic structure is drastically changed, modifying the opacity. While the changes in the opacity will not change the total energy radiated (Hernquist 1985), they will result in a redistribution of the emergent power among frequencies (see, e.g., Mihalas 1978). This redistribution affects the flux in the bandpasses of different detectors differently, and may give rise to detectable spectral features. Work has been done (Romani 1987) on radiative transfer in neutron star atmospheres, but this work has used opacity tables computed for $B = 0$.

A prerequisite to further work on predictions and interpretations of X-ray spectra of neutron stars is accurate atomic data for atoms in strong magnetic fields. In recent years, much research has been done (Simola and Virtamo 1978; O'Connell 1979; Kara and McDowell 1980; Wunner *et al.* 1981; Rösner *et al.* 1983; Rösner *et al.* 1984; Forster *et al.* 1984; Ruder *et al.* 1985; Wunner 1986; Wunner and Ruder 1987; Wunner *et al.* 1987) on the properties of hydrogen in very large magnetic fields. However, comparatively little has been done on helium or other elements, which could be important in determining the spectrum. Current models of supernovae indicate that the mass cut should occur within the iron layer. However, it is possible that significant amounts of nickel or other

heavy elements could be produced by the shock wave, and in the event of an asymmetrical explosion, the neutron star could accrete large amounts of any of the elements in the fusion cycle. An optical depth of unity in X-rays occurs at a depth of only $\approx$1 cm, which at a density of 1g/cm^3 is only $\approx 10^{13}$g $\approx 10^{-20} M_\odot$ over the surface of the neutron star, so the very top layer of the atmosphere will dominate the opacity. Since the surface gravity is so high, gravitational separation will be very rapid, on the order of $\sim$1-100s for a helium photosphere of typical temperature and density (Alcock and Illarionov 1980), and the lightest element present will rise to the top. A similar situation occurs in white dwarfs (Liebert 1980), where stars with virtually pure hydrogen and helium atmospheres have been detected. Another factor is that if the column depth of, e.g., hydrogen becomes large enough, nuclear reactions may convert it to helium, and so on. For an overview of these processes, see Shapiro and Teukolsky 1983 Chapter 3 Section 7.

The conclusion is that since the surface of observable neutron stars could have almost any composition (elements heavier than helium being perhaps the most likely in isolated neutron stars), we should investigate many possibilities. Astrophysical calculations ultimately need X-ray opacity tables similar to the zero-field tables in Saloman *et al.* 1988, but as a function of B from 0 to 10^{13} Gauss. This paper is a first step in the production of such opacity tables. We use a multiconfigurational Hartree-Fock code as a general method for determining the energy levels and wavefunctions of any atom in very high fields, and also compute the bound-bound and bound-free transition strengths for such atoms. In Section 2, we discuss the physics of atoms in high magnetic fields and the Hartree-Fock method, and also derive the bound-bound and bound-free cross sections in a high field. In Section 3, we describe the convergence tests of our program and compare our results with previous results for hydrogen and helium. In Section 4 we present our new results for the energy levels and transition probabilities for helium and carbon.

2. Method

2.1. Generation of the wavefunctions

In the following sections we will use the convention that the length scale will be the Landau scale

$$\hat{\rho} = \sqrt{\frac{\hbar c}{eB}} = 2.5 \times 10^{-10} B_{12}^{-1/2} \text{cm}, \tag{1}$$

where $B_{12} = B/10^{12}$G, and the magnetic field will be measured in terms of the reference field

$$B_0 = \frac{2\alpha^2 m_e^2 c^2}{e\hbar} = 4.7 \times 10^9 \text{G}, \tag{2}$$

which is the field at which the Coulomb and magnetic energies are equal for hydrogen.

The Hamiltonian of a neutral atom in a uniform magnetic field is

$$\begin{aligned} H &= H_B + V_{en} + V_{ee} \\ &= \sum_i \frac{1}{2M}(\mathbf{p}_i + \frac{e}{c}\mathbf{A}_i)^2 + \sum_i \frac{e}{mc}\mathbf{B}\cdot\mathbf{S}_i - Ze^2 \sum_i \frac{1}{r_i} + e^2 \sum_{i<j} \frac{1}{r_{ij}}, \end{aligned} \tag{3}$$

where

$\mathbf{p}_i$ is the momentum of the ith electron,

$\mathbf{A}$ is the vector potential of a constant magnetic field, $\mathbf{A} = \frac{1}{2}\mathbf{B} \times \mathbf{r}$

$\mathbf{S}$ is the spin,

Z is the atomic number,

r_i is the position of the ith electron,

r_{ij} is the separation between the ith and jth electrons,

H_B is the single-particle magnetic Hamiltonian,

V_{en} is the electron-nucleus potential and

V_{ee} is the electron-electron potential.

Since we are dealing with very strong magnetic fields ($B \gg Z^2 B_0$), a cylindrical expansion

$$\Psi_{m\nu}(z,\rho,\phi) = \sum_n f_{nm\nu}(z)\Phi_{nm}(\rho,\phi) \tag{4}$$

will be used, where ν, m and n are, respectively, the z, ϕ (azimuthal) and ρ (radial) quantum numbers, and the Φ_{nm} are the Landau states

$$\Phi_{nm}(\rho,\phi) = \frac{\sqrt{n!}}{\sqrt{2\pi(n+|m|)!\hat{\rho}^2}}\left(\frac{\rho}{\sqrt{2}\hat{\rho}}\right)^{|m|} e^{-\rho^2/4\hat{\rho}^2} L_n^{|m|}\left(\frac{\rho^2}{2\hat{\rho}}\right) e^{-im\phi}, \tag{5}$$

where $L_n^{|m|}$ are the associated Laguerre polynomials. In this paper we will deal only with n=0 states, because $n \neq 0$ states have much higher energy, on the order of the cyclotron energy $\hbar\omega_c = \frac{\hbar eB}{Mc} \approx 11.5 B_{12}$keV. Strictly speaking, this expansion is valid only for $B \gg Z^2 B_0$, but in practice (Rösner *et al.* 1984) accurate energy values may be generated for $\frac{B}{Z^2 B_0} \gtrsim 1$, though near the critical field more terms ($n > 0$) need to be kept. At the critical field and below, a spherical expansion

$$\Psi_m(\mathbf{r}) = \sum_l \frac{1}{r} f_l(r) Y_{lm}(\theta,\phi)$$

should be used, and the combination of the two regimes allows the structure of atoms to be calculated in arbitrary fields. For additional comments on the validity of these methods, see Rösner *et al.* 1984.

The technique that we have chosen for determining the wavefunctions is the Hartree-Fock method, which is equivalent to solving the variational equation

$$\frac{\delta}{\delta\chi}\left(\frac{<\Psi|H|\Psi>}{<\Psi|\Psi>}\right) = 0, \tag{6}$$

where χ is the total wavefunction

$$\chi = \Psi|S_z>,$$

$|S_z>$ is the spin wavefunction, and the wavefunction Ψ is approximated by a one-particle Slater determinant.

In strong fields, the wavefunctions are approximately separable into components perpendicular to the B-field ($\hat{\rho}, \hat{\phi}$) and the component parallel to the field ($\hat{z}$), with the only unknowns being the one-dimensional functions $f_{0m\nu}(z)$, so the Hartree-Fock equations reduce to the one-dimensional coupled equations

$$\frac{\delta}{\delta f_{0m\nu}(z)}\left(\frac{<\Psi|H|\Psi>}{<\Psi|\Psi>}\right) = 0. \tag{7}$$

For further details about the behavior of the Hartree-Fock equations, see Froese Fischer 1977.

There has been a debate about whether a renormalization of the wavefunctions should be applied to compensate for screening effects for $B = 0$ and $Z < 55$ (Pratt 1960; Pratt and Tseng 1972). This renormalization is done by replacing the nuclear charge Z in the wavefunction with an effective charge Z_{eff}, where $Z_{eff} = Z - S$, and S is a screening parameter (e.g. S=0.3 for the K shell, S=4.15 for the L shell). This procedure would most greatly affect the outer shells, and would typically alter the cross section by less than 10%. However, comparisons with experimental results (Saloman *et al.* 1988) indicate that the unrenormalized wavefunctions give better agreement. Besides errors that are due to truncation of the configuration space (which can be eliminated by using more powerful computers), most of the error in zero-field Hartree-Fock calculations is caused by the symmetrization of the spatial wavefunction of electrons in a spin-singlet state. In the full wavefunction, the electron–electron repulsion causes a depletion of the wavefunction for small relative distances (Coulomb hole); naive symmetrization of the orbitals causes the opposite effect. For electrons in a spin-triplet state, the antisymmetrization of the spatial wavefunction creates a hole that imitates the Coulomb hole. In strong fields, the spins are all aligned antiparallel to the field; all electron-pairs are in a spin-triplet state, and the Slater determinant reduces to a totally antisymmetric spatial determinant. The error is therefore significantly smaller than the 1% error associated with zero-field calculations (Weissbluth 1978, *Atoms and Molecules*, p. 400). In our program, the main source of error

is the assumption that $n = 0$; for a comparison with the multiterm expansion of Rösner *et al.*, (see Section 3.2).

Treating the nucleus as infinitely massive, the expectation value of the Hamiltonian is

$$E =< H >=< H_B > + < V_{en} > + < V_{ee} >, \tag{8}$$

where

$$\begin{aligned}
< H_B > =< H_z > &= \frac{\hbar^2}{2M} \sum_{m\nu} \int |f'_{m\nu}(z)|^2 dz \\
< V_{en} > &= -\frac{Ze^2}{\hat{\rho}} \sum_{m\nu} \int V_m(z) |f_{m\nu}(z)|^2 dz \\
< V_{ee} > &= \frac{e^2}{\hat{\rho}} \sum_{m\nu m'\nu'} \Big(\iint D_{mm'}(z-z') |f_{m\nu}(z)|^2 |f_{m'\nu'}(z')|^2 \\
&\quad - E_{mm'}(z-z') f_{m\nu}(z) f_{m'\nu'}(z') f^*_{m'\nu'}(z) f^*_{m\nu}(z') \Big) dz\, dz',
\end{aligned} \tag{9}$$

with the nuclear, direct and exchange kernels

$$\begin{aligned}
V_m(z) &= \int \frac{|\Phi_{m0}(\rho)|^2}{\sqrt{\rho^2+z^2}} \rho d\rho d\phi = \int \frac{e^{-\rho^2/2} \rho^{2m+1}}{2^m m! \sqrt{\rho^2+z^2}} d\rho \\
D_{mm'}(z-z') &= \int \frac{e^{-(\rho^2+\rho'^2)/2} \rho^{2m+1} \rho'^{2m'+1}}{2^{m+m'} m! m'! \sqrt{(\rho-\rho')^2+(z-z')^2}} d\rho\, d\rho' \\
E_{mm'}(z-z') &= \iiint \frac{e^{-(\rho^2+\rho'^2)/2} (\rho\rho')^{m'+m+1} e^{-i(m-m')(\phi-\phi')}}{2^{m+m'} m! m'! \sqrt{(\rho-\rho')^2+(z-z')^2}} d\rho\, d\rho' \frac{d\phi}{2\pi} \frac{d\phi'}{2\pi},
\end{aligned}$$

and we used the fact that for the n=0 orbitals, $< H_z >= - < H_\perp >$. The Hartree-Fock equations (6) for the ground-state orbitals are equivalent to

$$\frac{\delta < \Psi|H|\Psi >}{\delta f^*_{m\nu}(z)} = \epsilon_{m\nu} \frac{\delta < \Psi|\Psi >}{\delta f^*_{m\nu}(z)}, \tag{10}$$

where the Lagrange multipliers, $\{\epsilon_{m\nu}\}$, ensuring the orthogonality relations, are the single particle energies. It can be shown that these equations are

$$\Big[-\frac{\hbar^2}{2M} \frac{d^2}{dz^2} - \frac{Ze^2}{\hat{\rho}} V_m(z) + \frac{e^2}{\hat{\rho}} K_m(z) - \epsilon_{m\nu} \Big] f_{m\nu}(z) = \frac{e^2}{\hat{\rho}} J_{m\nu}(z), \tag{11}$$

where

$$K_m(z) \equiv \sum_{m'\nu'} \int D_{mm'}(z-z')|f_{m'\nu'}|^2 dz'$$
$$J_{m\nu}(z) \equiv \sum_{m'\nu'} f_{m'\nu'}(z) \int E_{mm'}(z-z') f^*_{m'\nu'}(z') f_{m\nu}(z') dz'. \tag{12}$$

The initial wavefunctions, taken from restricted variational studies (Flowers *et al* 1977; Lee 1976), were of the form

$$f_{m\nu} \propto z^\nu e^{-a_{m\nu}|z|/\hat{\rho}}. \tag{13}$$

In this equation, the coefficients $a_{m\nu} \approx 1$ (see Lee 1976 for a table of values), but the final solution is insensitive to wide variation in the parameters. These wavefunctions are generated for all of the states of interest, then Equation (11) is solved for the new wavefunctions, which are orthonormalized, and the procedure is repeated until the total energy (8) converges. The orthonormalization property,

$$\iiint \Psi^*_{nm\nu}(z,\rho,\phi)\Psi_{n'm'\nu'}(z,\rho,\phi)\rho d\rho d\phi dz = \delta_{nn'}\delta_{mm'}\delta_{\nu\nu'}, \tag{14}$$

is guaranteed for states of different n or m by the properties of the Landau function (5), while for states of different ν the Gram-Schmidt procedure is used.

The program may be represented in algorithm form as follows:

(*i*) Take a set of quantum numbers, $\{m\nu\}$,large enough to include those of all occupied states.

(*ii*) Guess the wavefunctions, f, and guess which states are occupied.

(*iii*) From (12) and the wavefunctions of the occupied states, obtain the integrals $\{K_m, J_{m\nu}\}$.

(*iv*) Calculate the total energy (9).

(*v*) Calculate the single particle energies by taking the scalar products of Equation (11) with the wavefunctions $f_{m\nu}$. The Z states with the lowest energy will be the occupied states.

(*vi*) With the kernels and the single-particle energies, solve (11) for the new wavefunctions. With K and J, the equations are uncoupled and inhomogeneous; they are easily solved by the Green's function method (Koonin 1986, p. 49).

(*vii*) Orthonormalize the new wavefunctions.

(*viii*) Iterate *iii–vii* until the total energy converges.

This algorithm will produce the ground state of the atom; it is also possible to generate any excited state by specifying that state as occupied.

In addition to the initial wavefunction, the program accepts as input the length of the integration box L (in units of $\hat{\rho}$) and the number of integration points N.

The ground state orbitals are the Z states with the lowest energy, and as a general rule states with (m=0,...,$Z-1$;ν=0) will be occupied. For example, for $B_{12}=1$ and $Z \leq 12$, there are no occupied states with $\nu > 0$, though for iron ($Z=26$), $m=0$ through $m=5$ with $\nu=1$ are all occupied. For B_{12}=5, and $Z < 19, \nu > 0$ states are unoccupied, while for $Z=26$, $m=0$ and 1 with $\nu=1$ are occupied. We can understand this preference for $\nu=0$ states qualitatively by replacing the probability distribution of the electrons with that of a long cylinder with radius $\hat{\rho}$ and length l (Ruderman 1971), so the energy is roughly

$$E \approx \frac{\hbar^2}{2Ml^2} - \frac{Ze^2}{l}\log\left(\frac{l}{\hat{\rho}}\right) \tag{15}$$

and minimization with respect to l yields

$$l = l_g \approx \left(\frac{a_0/Z\hat{\rho}}{\log(a_0/Z\hat{\rho})}\right)\hat{\rho} \tag{16}$$

for the ground state, where a_0 is the Bohr radius, $a_0 = 0.5 \times 10^{-8}$cm. For a state $\nu > 0$, the typical distance from the nucleus to the electron is greater than l_g, so the binding energy is $|E| \leq \frac{Ze^2}{l_g}$. For a state with $m > 0$, the dependence of E on ρ is logarithmic, so

the energy is almost unchanged and $m > 0$ states have lower energy than $\nu > 0$ states. Further details are contained in Neuhauser (1986).

2.2. Transition strengths and cross sections

The radiative transitions of hydrogen have been treated in great detail in, e.g., Forster *et al.* 1984, and a good discussion of the fundamental quantum mechanics may be found in Clayton 1983. The bound-bound cross section as a function of frequency is

$$\sigma(\omega) = \frac{4\pi^2\alpha}{M^2\omega_{ks}} \left| < k| \exp(i\frac{\omega_{ks}}{c}\mathbf{n}\cdot\mathbf{r})\pi\cdot\epsilon|s> \right|^2 \mathcal{L}(\omega-\omega_{ks}), \tag{20}$$

where

$\hbar\omega_{ks}$ is the energy difference between the k and s states,

s is the initial state

k is the final state

α is the fine structure constant, $\alpha \approx \frac{1}{137}$

$\mathbf{n}$ is the unit vector in the propagation direction of the photon,

$\pi = \mathbf{p} + \frac{e}{c}\mathbf{A}$,

ϵ is the polarisation vector of the photon, and

$\mathcal{L}$ is the Lorentz profile,

$$\mathcal{L}(\omega-\omega_{ks}) = \frac{\Gamma/2\pi}{(\omega-\omega_{ks})^2 + (\Gamma/2)^2}, \tag{21}$$

where

$$\Gamma = \frac{2e^2\omega_{ks}^2}{3mc^3} f_{ks}, \tag{22}$$

and f_{ks} is the oscillator strength.

For the frequencies that dominate the opacities of cool neutron stars (T$< 10^6$K), it is a good approximation to assume $\exp(i\frac{\omega_{ks}}{c}\mathbf{n}\cdot\mathbf{r}) \approx 1$. For the hydrogen ground state

at $B/B_0 = 1000$, the frequency of a bound-bound transition is less than $\omega \approx 250\text{eV} \approx 1.3 \times 10^7 \text{cm}^{-1}$, while the wavefunction has a scale length of $r \approx 15\hat{\rho} \approx 1.7 \times 10^{-9}\text{cm}$, so that $e^{i\frac{\omega_{ks}}{c}\mathbf{n}\cdot\mathbf{r}} \approx e^{i(0.02)} \approx 1$. The dipole approximation will be worse for helium and carbon, since the frequencies involved are higher, but even for carbon at $B/B_0 = 1000$, the exponent is only 0.05, so the dipole approximation is valid to within 5% over the entire range of parameters considered.

Substituting $\exp(i\frac{\omega_{ks}}{c}\mathbf{n}\cdot\mathbf{r}) = 1$ in (20), using the identity

$$\pi = [\frac{\pi^2}{2M}, \mathbf{r}]\frac{i}{\hbar} \tag{23}$$

and simplifying, we find that the integral of the cross section over the line width Γ is

$$\int_\Gamma \sigma(\omega)d\omega = 4\pi^2\alpha\omega_{ks} \sum_{i=+,-,z} |< k|\mathbf{r}\cdot\epsilon_i|s >|^2 \cdot \gamma_i, \tag{24}$$

where γ_i is the fraction of the light polarised in direction i.

To get an idea of the selection rules for polarization, we will look at the case of right circular polarization, $\epsilon_i = \epsilon_+$. Here we are defining "right circular" with respect to the magnetic field, not $\mathbf{n}$. Thus, if the photon is propagating parallel to the field, the convention is as usual, whereas if the two are antiparallel, the convention is opposite to the one normally used.

$$< m'\nu'|\mathbf{r}\cdot\epsilon_+|m\nu >= \int f_{m\nu}f_{m'\nu'}dzI, \tag{25}$$

where

$$I = \int -\frac{\rho e^{i\phi}}{\sqrt{2}}\Phi_{0m}(\rho,\phi)\Phi^*_{0m'}(\rho,\phi)\rho d\rho d\phi. \tag{26}$$

Substituting in (5) and integrating, we find that

$$I = -\sqrt{m}\delta(m' + 1 - m)\hat{\rho}, \tag{27}$$

(δ is the Dirac delta) so that the right circular polarization gives transitions with $\Delta m = -1, \Delta\nu =$even. Similarly, the $-$ (left circular) polarization gives transitions with $\Delta m = +1, \Delta\nu =$even and the z polarization has $\Delta m = 0, \Delta\nu =$odd.

Therefore, the explicit expression for the bound-bound cross section is

$$\sigma(\omega) = 4\pi^2\alpha\omega \sum_{m\nu\nu'} \Big[\gamma_+\mathcal{L}(\epsilon_{m\nu}+\omega-\epsilon_{(m-1)\nu'})m\hat{\rho}^2\Big|\int f_{m\nu}f_{(m-1)\nu'}dz\Big|^2$$

$$+\gamma_-\mathcal{L}(\epsilon_{m\nu}+\omega-\epsilon_{(m+1)\nu'})(m+1)\hat{\rho}^2\Big|\int f_{m\nu}f_{(m+1)\nu'}dz\Big|^2$$

$$+\gamma_z\mathcal{L}(\epsilon_{m\nu}+\omega-\epsilon_{m\nu'})\Big|\int f_{m\nu}f_{m\nu'}zdz\Big|^2\Big] \tag{28}$$

where $\epsilon_{m\nu}$ is the energy of the $m\nu$ orbital. The bound-free, or ionization, cross section is similar, except that the cross section is

$$\sigma(\omega) = 4\pi^2\alpha\omega|< k|\mathbf{r}\cdot\epsilon|s >|^2\frac{\Delta n}{\Delta\omega}, \tag{29}$$

where Δn is the number of eigenstates in a frequency interval $\Delta\omega$ about the kinetic energy $E_k = \hbar\omega - \epsilon_{m\nu}$. For a particle in a one-dimensional box of length L (appropriate for photon energies $\hbar\omega \ll \hbar\omega_c$, so the electron remains in the $n = 0$ Landau state), we have

$$\Delta n(E) = \frac{Ldp}{h} \tag{30}$$

or, using $p = \sqrt{2EM}$ and $dE = \hbar d\omega$, we get

$$\frac{\Delta n}{\Delta\omega} = \frac{L\sqrt{2M}}{2\pi\sqrt{E}}. \tag{31}$$

In this box the normalized free wavefunction is $\frac{g(p,z)}{\sqrt{L}}$, where $g(p,z)$ is the free wavefunction for momentum p, determined from the Schrödinger equation

$$-\frac{\hbar^2}{2M}\nabla^2 g + Vg = Eg,$$

where V is the atomic potential, $E = \frac{p^2}{2M}$ and $g(p,z) \equiv e^{\frac{ipz}{\hbar}}$ at infinity. Therefore, the bound-free cross section becomes

$$\sigma(\omega) = 2\pi\alpha\omega \sum_{m\nu} \Theta(\omega + \epsilon_{m\nu}) \sqrt{\frac{M}{E}} \Big[\gamma_+ m\hat{\rho}^2 \Big| \int f_{m\nu} g(p,z) dz \Big|^2$$

$$+\gamma_-(m+1)\hat{\rho}^2 \Big| \int f_{m\nu} g(p,z) dz \Big|^2$$

$$+\gamma_z \Big| \int f_{m\nu} g(p,z) z dz \Big|^2 \Big], \tag{32}$$

where Θ is the step function,

$$\begin{aligned} \Theta(x) &= 0 \text{ for } x < 0, \\ &= 1 \text{ for } x \geq 0, \end{aligned} \tag{33}$$

M is the mass of the electron, and E is the kinetic energy of the electron.

3. Tests of the program

3.1 Convergence

As indicated in section 2.1, the program integrates using an integration box of length L and a number of grid points N. We have tested the program to determine if the value of the energy converges in a small number of iterations; if in the limit of large N the energy converges; and if in the limit of large L the energy converges. Figure 1 shows that for hydrogen, given L and N, the energy converges rapidly. In all of the cases tested, the energy varies by less than 0.01eV after the third iteration. Next, in Figure 2, the dependence of final energy on N with L constant is shown. Because of systematic integration error, the magnitude of the energy decreases with decreasing N for ν=0 or 2, while for ν=1 it increases with decreasing N. Finally, in Figure 3, the energy as a function of L with N constant is shown. Since for $\nu \neq 0$ the wavefunction can extend past $L = 100\hat{\rho}$, there is significant error in the ν=1 and 2 energies, especially for high B. In all of the graphs, the ground state 000 is shown, since it is most perturbed by the Coulomb attraction; the excited states converge even more rapidly.

3.2. Comparison with previous results

Using a highly accurate multiconfigurational Hartree-Fock code, Rösner *et al.* (1984) and Forster *et al.* (1984) produced energies and transition strengths for hydrogen in arbitrary magnetic fields. The difference in the calculations of that paper and ours is that while they considered mixing of states with $n > 0$, we restricted n to be 0. We did this in the interest of simplicity, as the inclusion of $n \neq 0$ states would considerably increase the difficulty of evaluating equations (9). More accurate computations will, however, have to take the mixing into account. Liu and Starace (1987) produced upper and lower bounds on the energy levels of hydrogen using a single-configuration method. While this is an excellent method for estimating the energies of hydrogenic elements, it is unfortunately difficult to generalize to $Z > 1$ because of the effects of electron-electron interactions. The results for hydrogen below were generated by a simplified method for comparison purposes, to give an idea of the magnitude of errors expected for elements with $Z > 1$. Table 1 shows the comparison between the high-field energy values of Rösner *et al.* 1984 and the values found in this paper. The largest difference in E, 3.4%, occurs for the 000 state at $B/B_0 = 10$, as might be expected, since the lower the field and the more centrally condensed about the spherical nuclear potential the state, the less accurate is the (cylindrical) assumption that n=0. Table 2 gives the oscillator strengths for different transitions. The accuracy of the strengths of the transitions in which Δm=1 is less than the accuracy of those for which Δm=0, but even for Δm=1 there are only two transitions for which the discrepancy in A is greater than 20%. As was shown in Wunner *et al.* 1980, transitions with Δm=1 will be affected by finite proton mass, which affects the energy levels of states with different m. However, since this effect is proportional to the cyclotron frequency of the nucleus, it will be less important for helium and carbon. In Table 3, our results for the ground-state binding energies of helium in fields ranging from 2×10^{10} to 5×10^{13} Gauss are compared with those of Pröschel *et al.* (1982). Here again we see a close correspondence, with by far the greatest difference (1.9%) coming at B=5x10^{13} Gauss. The reason for this difference is that (as we can see from (16) combined with (1)), the higher B is, the greater l is in

units of $\hat{\rho}$, so that the contribution from the ends of the grid becomes more important. Table 4 shows the bound-free oscillator strengths A from the ground state of hydrogen. It is apparent that the higher the field, the more important are bound-free transitions. This is because as the field increases, the ground-state energy decreases logarithmically, while the energies of the other states stay roughly constant, so that the bound-bound transition energies become more nearly equal to each other and to the ionization energy, and as a result they become closer in transition strength as well. Therefore, transitions to highly excited states and bound-free transitions become relatively more important. Another test is that the oscillator strengths should obey the Thomas-Rieche-Kuhn sum rule: From a given initial state s of an electron,

$$\sum_k f_{ks} = 1 \qquad (36),$$

where the sum is over all final states. Therefore, for an atom with Z electrons, the sum of the oscillator strengths of one-electron transitions will be Z. In Table 5 we see a list of the sum of the bound-free and the first few bound-bound oscillator strengths for hydrogen. Clearly, while individual transition strengths to highly excited states might be small, their contribution as a whole is important, especially for high fields.

3.3. Error Analysis for $Z > 1$

We find empirically that most of the differences between our computations for hydrogen and helium and previous adiabatic calculations can be removed by increasing the resolution and size of the grid. A determination of the scaling of these two types of error with Z will allow us to predict the errors in helium, carbon, etc. from those in hydrogen. The errors that are due to grid resolution can be estimated as follows. The integrations in (9) can be thought of as performed using Simpson's rule, so that the error in an integral of the form

$$\int_b^a h(z)dz,$$

with N steps, is

$$\delta \sim \frac{(b-a)^5}{N^4} h^{(4)}(\xi),$$

where ξ is some value between a and b. In an atom with $Z > 1$, most of the error in energy will come from computing the energy of the innermost electron, as for this electron the Coulomb force has greater effect and consequently, the wave function is most concentrated at the origin and the effective grid resolution lowest. For this electron, the fourth derivative of the function $h(z)$ is of order

$$\frac{h(\xi)}{(z/\hat{\rho})^4},$$

evaluated at a characteristic value of z, $z = l$, where l is given by (16). Therefore, the error depends only on the ratio $l/\hat{\rho}$, not Z. Since for atomic number Z at magnetic field B this ratio is equal to that for hydrogen at magnetic field B/Z^2, we may estimate the error for higher atoms from the error for hydrogen at corresponding values of B/Z^2. For instance, for hydrogen at 2.35×10^{11}G, the ground-state energy estimate is 100.1eV with 1024 grid points and an integration box of length $800\hat{\rho}$. With 2048 grid points and the same integration box, the estimate is 101.5eV, for a difference of 1.4%. For helium at $2.35 \times 10^{11} \times 2^2 = 9.4 \times 10^{11}$G, the corresponding difference is 5.4eV/561.4eV, or about 1.0%. As another example, hydrogen at 1.41×10^{11}G has a difference of 0.4eV out of a total of 85.5eV (or about 0.5%) between $N = 2048$, $L = 800\hat{\rho}$ and $N = 4096$, $L = 800\hat{\rho}$. Carbon at $1.41 \times 10^{11} \times 6^2 \approx 4.7 \times 10^{12}$G has a difference of 10eV/1712eV$\approx$0.6% between calculations on those same grids. For excited states, the wavefunction is not as concentrated at the origin, so that it is not as important to have a finely spaced grid. In addition, for a neutral atom, excited states are influenced by an effective charge of $Z_{eff} = 1$ (because they are far away from the nucleus), so that excited state errors are roughly the same as the errors for the equivalent hydrogen states at the same magnetic field. We conclude that the technique of scaling from hydrogen allows us to make accurate estimates of the errors

that are due to grid resolution for atoms with $Z > 1$. Exactly the same argument may be applied to transition probabilities.

The magnitude of the second type of error, truncation of the integration box, may be estimated from (9) by noting that the size of the potential terms (which dominate over the kinetic term) is proportional to $|f_{m\nu}(z)|^2$. We find from experience that for states with $\nu = 0$, it is necessary to extend the integration to $L = 100\hat{\rho}$ for an accuracy of 0.1%, while for excited states ($\nu > 0$), $L = 800\hat{\rho}$ may be required. This can necessitate a compromise, as in carbon in the (00, 10, 20, 30, 40, 51) state, where it is necessary to have both an extended integration box and a fine grid at the origin. Perhaps in future calculations an adaptive step size may take care of this problem.

The adiabatic calculations are exact only in the $B \to \infty$ limit, so it is also important to estimate the error that is due to assuming that $n = 0$. This error is related to the ratio of Coulomb force to magnetic force, so that we may estimate the correction by comparing an atom with $Z > 1$ at magnetic field B to the exact calculations of Rösner *et al.* for hydrogen at a field strength of B/Z^2. We have placed error estimates based on the above effects in the tables for helium and carbon. In general, the integration box is large enough that truncation errors contribute a negligible amount to the total error, while below $\frac{B}{Z^2 B_0} = 50$, non-adiabatic effects dominate and above $\frac{B}{Z^2 B_0} = 50$, grid resolution errors are the most important.

4. Results

The binding energies for a variety of states of helium in several field strengths are presented in Table 6. Also listed are the binding energies for the first and second orbitals. It can be seen that while the $\nu = 0$ orbitals of hydrogen and helium are quite different in energy, the binding energies of the excited states are asymptotically equal (this is also true for the non-magnetic case, since the farther the electron is from the nucleus, the more the nucleus and inner $Z - 1$ electrons look like a point charge of Z=1). Figure 4 also

illustrates this; when the state is tightly bound, the wavefunctions of hydrogen and helium differ significantly near the nucleus, while for loosely bound orbitals the wavefunctions are essentially identical. Table 7 gives the oscillator strengths from the helium ground state to several excited states. It can be seen that as with hydrogen, transitions to highly excited states become relatively more important for higher B. In Table 8 we give the binding energies of orbitals for carbon in magnetic fields of $B = 200B_0$, $B = 500B_0$ and $B = 1000B_0$. In each case the ground-state energy of the whole atom is listed, along with the binding energies of various states. For the excited ($\nu \neq 0$) states, all electrons other than the excited electron are assumed to be in their ground states. Again we see (Figure 4) that while for the ground state the binding energies of carbon and hydrogen orbitals are radically different, for excited states they are very close. In Table 9 bound-bound oscillator strengths are listed, and in Table 10 bound-free oscillator strengths are given. It can be seen that while bound-free transitions become weaker with increased field, the relative importance of the ionization process increases. In order to estimate the magnitude of errors in these computations, we calculated a few of the energies and oscillator strengths for helium and carbon with greater accuracy (i.e., more integration points). The result was that none of the energies changed by more than $\sim 1\%$, and none of the oscillator strengths changed by more than $\sim 2\%$.

These values are a step toward the construction of realistic model atmospheres for neutron stars. We are constructing opacity tables with various temperatures and surface compositions, and following Romani 1987 we are using (e.g.,Mihalas 1978) techniques to calculate model atmospheres and spectra of emerging radiation. We hope that these calculations will be accurate enough that for the first time it will be possible to deduce, reliably, parameters such as magnetic field, surface temperature and surface composition from X-ray observations of neutron stars.

Acknowledgements

We thank E. S. Phinney for proposing the problem, as well as for his guidance and many helpful suggestions. This work was supported in part by National Science Foundation grants AST84-51725 and PHY85-05682. M C M was partially supported by an NSF Graduate Fellowship.

References

Alcock, C., and Illarionov, A. 1980 *Ap. J.*, **235**, 534.

Clayton, D. 1983 *Principles of Stellar Evolution and Nucleosynthesis* (Chicago:The University of Chicago Press).

Flowers, E. G., Lee, J. F., Ruderman, M. A., Sutherland, P. G., Hillbrandt, W., and Muller, E. 1977 *Astrophys. J.*, **215**, 291.

Forster, H., Strupat, W., Rösner, W., Wunner, G., Ruder, H., and Herold, H. 1984 *J. Phys. B: At. Mol. Phys.*, **17**, 1301.

Froese Fischer, C. 1977 *The Hartree-Fock Method for Atoms: A Numerical Approach* (New York: Wiley).

Hernquist, L. 1985 *Ph.D. thesis*, California Institute of Technology.

Joss, P. C., and Rappaport, S. A. 1984 *Ann. Rev. Astron. Astrophys.*, **22**, 537.

Kara, S. M., and McDowell, M. R. C. 1980 *J. Phys. B: At. Mol. Phys.*, **13**, 1337.

Koonin, S. E. 1986 *Computational Physics* (Menlo Park, California: Benjamin/Cummings).

Lee, J. F. 1976 *Ph.D. thesis*, Columbia University.

Liebert, J. 1980 *Ann. Rev. Astron. Astrophys.*, **18**, 363.

Liu, C-R., and Starace, A. F. 1987 *Phys. Rev. A*, **35**, 647.

Mihalas, D. 1978 *Stellar Atmospheres* (San Francisco: Freeman).

Neuhauser, D. 1986 *Ph.D. thesis*, California Institute of Technology

Neuhauser, D., Langanke, K., and Koonin, S. E. 1986 *Phys. Rev. A*, **33**, 2084.

O'Connell, R. F. 1979 *Phys. Lett.*, **70A**, 389.

Pratt, R. H. 1960 *Phys. Rev.*, **119**, 1619.

Pratt, R. H., and Tseng, H. K. 1972 *Phys. Rev. A*, **5**, 1063.

Pröschel, P., Rösner, W., Wunner, G., Ruder, H., and Herold, H. 1982 *J. Phys. B: At. Mol. Phys.*, **15**, 1959.

Romani, R. W. 1987 *Astrophys. J.*, **313**, 718.

Rösner, W., Herold, H., Ruder, H., and Wunner, G. 1983 *Phys. Rev.*, A **28**, 2071.

Rösner, W., Wunner, G., Herold, H., and Ruder, H. 1984 *J. Phys. B: At. Mol. Phys.*, **17**, 29.

Ruder, H., Herold, H., Rösner, W., and Wunner, G. 1985 *Physica B and C*, **127**, 11.

Ruderman, M. A. 1971 *Phys. Rev. Lett.*, **27**, 1306.

Saloman, E. B., Hubbell, J. H., and Scofield, J. H. 1988 *At. Dat. Nuc. Dat. Tab.*, **38**, 1.

Shapiro, S., and Teukolsky, S. 1983 *Black Holes, White Dwarfs and Neutron Stars* (New York: Wiley).

Simola, J., and Virtamo, J. 1978 *J. Phys. B: At. Mol. Phys.*, **11**, 3309.

Taylor, J. H., and Stinebring, D. R. 1986 *Ann. Rev. Astron. Astrophys.*, **24**, 285.

Tsuruta, S. 1986 *Comments Ap.*, **11**, 151.

Weissbluth, M. 1978 *Atoms and Molecules*, (New York: Academic Press).

Wunner, G. 1986 *J. Phys. B: At. Mol. Phys.*, **19**, 1623.

Wunner, G., Geyer, F., and Ruder, H. 1987 *Astro. Sp. Sc.*, **131**, 595.

Wunner, G., and Ruder, H. 1987 *Phys. Scr.*, **36**, 291.

Wunner, G., Ruder, H., and Herold, H. 1980 *Phys. Lett.*, **79A**, 159.

— 1981 *J. Phys. B: At. Mol. Phys.*, **14**, 765.

Table 1. Energies for hydrogen in several magnetic fields, in units of eV. The states are listed by their m and ν quantum numbers, with $n = 0$ assumed. The energies in parentheses are from Rösner *et al.* The number of grid points is N=2048, and the integration box extends out to L=800$\hat{\rho}$.

Table 2. Oscillator strengths for hydrogen. The values in parentheses are from Forster *et al.* 1984. In the columns, the initial state is on the left and the final state is on the right.

Table 3. Ground state energies for helium. The values in parentheses are from Pröschel *et al.* 1982. The number of grid points is N=1024, and the integration box extends out to L=800$\hat{\rho}$. The magnetic field is measured in Gauss, and the energy is given in electron volts.

Table 4. Bound-free oscillator strengths, $f_{\rm bf}$, for hydrogen.

Table 5. Sum of oscillator strengths, $\sum f$, for hydrogen. This table lists the sum of the transition strengths from the ground state, 00, to the excited states 01, 03, 10, 12 and the bound-free oscillator strength.

Table 6. Energy values for helium. The magnitude of the total energy is listed, as well as the energies of the individual orbitals, where e1 is the energy of the first orbital listed and e2 is the energy of the second orbital. Energies are given in electron volts. The estimated errors are in brackets, and are measured in eV. The number of grid points is N=1024, and the integration box extends out to L=800$\hat{\rho}$.

Table 7. Oscillator strengths for helium. In each case, the transition is from the ground state (00,10) to the state listed. The estimated errors are in brackets.

Table 8. Energies for carbon. The magnetic field is measured in units of $B_0 = 4.7 \times 10^9$G, and when an excited state is listed, it is assumed that the other electrons are in their ground state (i.e., $\nu = 0$). The number of grid points is $N = 1024$, and the integration box extends out to $L = 800\hat{\rho}$, except for the ground state, which has $N = 512$ and $L = 100\hat{\rho}$. Energies are given in electron volts. The estimated errors are in brackets, and are measured in eV.

Table 9. Bound-bound oscillator strengths for carbon. Magnetic field is in units of $B_0 = 4.7 \times 10^9$G, and all transitions have their m-value listed in Column 1. The estimated errors are in brackets.

Table 10. Bound-free oscillator strengths for carbon. Magnetic field is given in units of $B_0 = 4.7 \times 10^9$G.

Figure 1. Convergence of hydrogen ground-state energy as a function of the number of iterations of the Hartree-Fock algorithm. The number of grid points is N=2048, and the integration box extends out to L=800$\hat{\rho}$. The magnetic field is in units of $B_0 = 4.7 \times 10^9$G.

Figure 2. Final energy (after five iterations) of hydrogen ground state, with the number of grid points N varying and the size of the integration box held constant at 400$\hat{\rho}$. The magnetic field is in units of $B_0 = 4.7 \times 10^9$G.

Figure 3. Final energy (after five iterations) of hydrogen ground state, with the size of the integration box L varying and the number of grid points held constant at 1024. The magnetic field is in units of $B_0 = 4.7 \times 10^9$G, and L is in units of $\hat{\rho} = \sqrt{\frac{\hbar c}{eB}}$.

Figure 4a. Comparison of the z-component of the wavefunction, $f_{m\nu}(z)$, for hydrogen, helium and carbon in a magnetic field of $B = 200B_0 = 9.4\times10^{11}$G. The solid line represents hydrogen, the short dashes represent helium, and the long dashes represent carbon. The graphs are labelled with the z quantum number, ν.

Figure 4b. Comparison of the z-component of the wavefunction, $f_{m\nu}(z)$, for hydrogen, helium and carbon in a magnetic field of $B = 500B_0 = 2.35 \times 10^{12}$G. The solid line represents hydrogen, the short dashes represent helium, and the long dashes represent carbon. The graphs are labelled with the z quantum number, ν.

Figure 4c. Comparison of the z-component of the wavefunction, $f_{m\nu}(z)$, for hydrogen, helium and carbon in a magnetic field of $B = 1000B_0 = 4.7 \times 10^{12}$G. The solid line represents hydrogen, the short dashes represent helium, and the long dashes represent carbon. The graphs are labelled with the z quantum number, ν.

Figure 5. Energy levels and sample allowed transitions of carbon in a $B = 200B_0 = 9.4 \times 10^{11}$G magnetic field. In this diagram, m and ν are taken to have the same meaning as in hydrogen, and where an excited state is drawn it is assumed that the other electrons are in their ground state (i.e., $\nu = 0$). The selection rule for transitions is that $\Delta m + \Delta\nu$ must be odd.

Table 1

	B/B_0							
$m\nu$	10	20	30	50	100	200	500	1000
00	58.2	74.3	85.5	101.5	127.2	157.9	207.2	251.9
	(60.26)	(76.19)	(87.18)	(103.0)	(128.6)	(159.2)	(208.4)	(253.1)
01	11.24	11.93	12.27	12.61	12.96	13.18	13.34	13.35
	(11.25)	(11.93)	(12.27)	(12.61)	(12.96)	(13.21)	(13.40)	(13.48)
02	6.03	6.44	6.66	6.93	7.28	7.59	7.93	8.12
	(6.09)	(6.47)	(6.70)	(6.96)	(7.32)	(7.64)	(8.05)	(8.32)
10	39.5	51.3	59.5	71.4	90.8	114.5	153.3	189.0
	(39.7)	(51.6)	(59.8)	(71.7)	(91.0)	(114.7)	(153.4)	(189.1)
11	10.23	11.11	11.56	12.04	12.55	12.91	13.18	13.26
	(10.23)	(11.12)	(11.56)	(12.05)	(12.56)	(12.93)	(13.25)	(13.39)
12	5.39	5.83	6.07	6.37	6.74	7.09	7.48	7.69
	(5.41)	(5.84)	(6.09)	(6.39)	(6.77)	(7.14)	(7.59)	(7.90)

Table 2

B/B_0	$00 \rightarrow 01$	$01 \rightarrow 02$	$10 \rightarrow 00$	$12 \rightarrow 00$
10	0.553 (0.560)	1.426 (1.477)	6.706(−2) (6.876(−2))	8.757(−4) (8.206(−4))
20	0.488 (0.499)	1.387 (1.435)	4.137(−2) (4.328(−2))	4.132(−4) (4.010(−4))
30	0.449 (0.461)	1.365 (1.409)	3.123(−2) (3.284(−2))	2.645(−4) (2.604(−4))
50	0.402 (0.413)	1.331 (1.376)	2.174(−2) (2.317(−2))	1.491(−4) (1.496(−4))
100	0.340 (0.351)	1.284 (1.327)	1.318(−2) (1.444(−2))	6.790(−5) (6.949(−5))
200	0.284 (0.293)	1.234 (1.274)	7.871(−3) (9.062(−3))	3.052(−5) (3.196(−5))
500	0.219 (0.227)	1.173 (1.201)	3.919(−3) (5.055(−3))	1.047(−5) (1.142(−5))
1000	0.179 (0.186)	1.126 (1.144)	2.290(−3) (3.398(−3))	4.613(−6) (5.295(−6))

Table 3

B	E
2×10^{10}	137.42 (137.61)
5×10^{10}	196.47 (196.74)
1×10^{11}	255.23 (255.59)
2×10^{11}	328.97 (329.45)
5×10^{11}	454.28 (455.05)
1×10^{12}	575.14 (575.30)
2×10^{12}	719.27 (721.04)
5×10^{12}	955.74 (958.80)
1×10^{13}	1173.6 (1177.5)
2×10^{13}	1433.0 (1433.4)
5×10^{13}	1870.1 (1834.8)

Table 4

B/B_0	f_{bf}
10	0.150
20	0.184
30	0.199
50	0.224
100	0.264
200	0.293
500	0.341
1000	0.374

Table 5

B/B_0	$\sum f$
10	0.770
20	0.673
30	0.679
50	0.648
100	0.617
200	0.585
500	0.564
1000	0.555

Table 6

B/B_0	$m_1\nu_1, m_2\nu_2$	E_{tot}	E_1	E_2
50	00,10	343.0 [20]	173.4 [10]	95.69 [0.5]
	00,11	258.8 [16]	225.7 [14]	11.40 [0.01]
	00,12	254.1 [15]	236.0 [14]	6.64 [0.01]
	01,10	183.7 [0.9]	12.19 [0.01]	147.8 [0.7]
	02,10	178.8 [0.9]	7.26 [0.01]	158.8 [0.8]
	00,01	260.9 [16]	225.1 [14]	13.49 [0.01]
	00,02	255.1 [15]	235.0 [14]	7.65 [0.01]
	10,11	184.9 [1.0]	150.8 [0.8]	13.40 [0.01]
	10,12	178.6 [0.9]	160.4 [0.8]	7.06 [0.01]
200	00,10	556.0 [16]	274.7 [8]	156.2 [0.6]
	00,11	412.2 [12]	376.8 [11]	11.83 [0.01]
	00,12	407.8 [13]	387.3 [12]	7.39 [0.01]
	01,10	297.0 [1]	11.80 [0.01]	261.1 [1]
	02,10	293.1 [1]	7.92 [0.01]	271.0 [1]
	00,01	413.7 [12]	377.1 [11]	13.34 [0.01]
	00,02	408.8 [13]	386.5 [12]	8.41 [0.01]
	10,11	298.6 [1]	262.6 [1]	13.39 [0.01]
	10,12	293.1 [1]	272.5 [1]	7.87 [0.01]
1000	00,10	931.2 [19]	447.3 [9]	264.5 [0.5]
	00,11	680.4 [14]	643.9 [13]	11.97 [0.01]
	00,12	676.5 [14]	653.6 [13]	8.04 [0.01]
	01,10	503.5 [1.0]	11.65 [0.01]	467.6 [0.9]
	02,10	500.4 [1.0]	8.51 [0.01]	476.1 [0.9]
	00,01	681.5 [14]	644.7 [13]	13.08 [0.01]
	00,02	677.5 [14]	653.0 [13]	9.05 [0.01]
	10,11	504.9 [10]	468.5 [9]	13.09 [0.01]
	10,12	500.5 [11]	477.4 [10]	8.60[0.01]

Table 7

B/B_0	01,10	00,11	03,10	00,13	00,02	10,12
50	0.206[5(-3)]	0.381[1(-2)]	2.74(-2)[5(-4)]	4.27(-2)[8(-4)]	8.56(-4)[2(-5)]	1.36(-3)[1(-4)]
200	0.113[3(-3)]	0.235[6(-3)]	1.51(-2)[4(-4)]	2.80(-2)[7(-4)]	1.66(-4)[4(-6)]	2.94(-4)[1(-6)]
1000	5.58(-2)[2(-3)]	0.125[5(-3)]	1.07(-2)[3(-4)]	1.99(-2)[6(-4)]	2.42(-5)[1(-6)]	4.84(-5)[3(-6)]

Table 8

$B/B_0 = 200$
ground 4087.2

m	$\nu = 0$	$\nu = 1$	$\nu = 2$	$\nu = 3$
0	1011 [35]	11.522 [0.01]	8.047 [0.01]	3.101 [0.01]
1	499 [4]	10.575 [0.01]	7.652 [0.01]	2.945 [0.01]
2	331 [1]	10.361 [0.01]	7.414 [0.01]	2.907 [0.01]
3	247 [1]	10.316 [0.01]	7.236 [0.01]	2.897 [0.01]
4	193 [1]	10.290 [0.01]	7.074 [0.01]	2.891 [0.01]
5	144 [1]	10.089 [0.01]	6.858 [0.01]	2.854 [0.01]

$B/B_0 = 500$
ground 5783.7

m	$\nu = 0$	$\nu = 1$	$\nu = 2$	$\nu = 3$
0	1373 [40]	9.952 [0.01]	8.348 [0.01]	2.695 [0.01]
1	693 [3]	9.875 [0.01]	8.054 [0.01]	2.945 [0.01]
2	466 [1]	9.936 [0.01]	7.858 [0.01]	2.691 [0.01]
3	350 [1]	10.036 [0.01]	7.705 [0.01]	2.707 [0.01]
4	275 [1]	10.129 [0.01]	7.562 [0.01]	2.721 [0.01]
5	208 [1]	10.099 [0.01]	7.363 [0.01]	2.715 [0.01]

$B/B_0 = 1000$
ground 7448.4

m	$\nu = 0$	$\nu = 1$	$\nu = 2$	$\nu = 3$
0	1712 [35]	9.741 [0.01]	8.593 [0.01]	2.508 [0.01]
1	880 [3]	9.783 [0.01]	8.335 [0.01]	2.517 [0.01]
2	597 [1]	9.885 [0.01]	8.115 [0.01]	2.533 [0.01]
3	452 [1]	10.005 [0.01]	8.010 [0.01]	2.552 [0.01]
4	357 [1]	10.119 [0.01]	7.873 [0.01]	2.569 [0.01]
5	272 [1]	10.147 [0.01]	7.684 [0.01]	2.573 [0.01]

Table 9

$B/B_0 = 200$

m	$m0 \rightarrow m1$	$m0 \rightarrow m3$	$m1 \rightarrow m2$
0	3.969(-2)[1(-3)]	6.19(-3)[2(-4)]	0.94295[0.03]
1	5.672(-2)[2(-3)]	9.16(-3)[3(-4)]	0.94519[0.03]
2	7.996(-2)[2(-3)]	1.283(-2)[4(-4)]	1.01724[0.03]
3	0.10893[3(-3)]	1.716(-2)[6(-4)]	1.09588[0.03]
4	0.14450[3(-3)]	2.216(-2)[7(-4)]	1.15936[0.04]
5	0.19306[5(-3)]	2.817(-2)[9(-4)]	1.17476[0.04]

$B/B_0 = 500$

m	$m0 \rightarrow m1$	$m0 \rightarrow m3$	$m1 \rightarrow m2$
0	1.108(-2)[2(-4)]	1.79(-3)[6(-5)]	0.52859[0.02]
1	2.307(-2)[4(-4)]	3.68(-3)[1(-4)]	0.62992[0.02]
2	3.804(-2)[8(-4)]	5.97(-3)[2(-4)]	0.73442[0.02]
3	5.646(-2)[1(-3)]	8.68(-3)[3(-4)]	0.83148[0.03]
4	7.943(-2)[2(-3)]	1.191(-2)[4(-4)]	0.91552[0.03]
5	0.11250[2(-3)]	1.622(-2)[6(-4)]	0.97148[0.03]

$B/B_0 = 1000$

m	$m0 \rightarrow m1$	$m0 \rightarrow m3$	$m1 \rightarrow m2$
0	5.71(-3)[2(-4)]	8.9(-4)[4(-5)]	0.37876[0.01]
1	1.353(-2)[3(-4)]	2.08(-3)[1(-4)]	0.49172[0.02]
2	2.362(-2)[6(-4)]	3.56(-3)[2(-4)]	0.59544[0.02]
3	3.619(-2)[9(-4)]	5.36(-3)[3(-4)]	0.69025[0.02]
4	5.205(-2)[1(-3)]	7.55(-3)[4(-4)]	0.77605[0.03]
5	7.553(-2)[2(-3)]	1.061(-2)[5(-4)]	0.84587[0.03]

Table 10

$B/B_0 = 200$

$m\nu$	A
00	0.485
10	0.463
20	0.453
30	0.447
40	0.481
50	0.478

$B/B_0 = 500$

$m\nu$	A
00	0.429
10	0.419
20	0.423
30	0.427
40	0.431
50	0.411

$B/B_0 = 1000$

$m\nu$	A
00	0.399
10	0.400
20	0.399
30	0.397
40	0.403
50	0.405

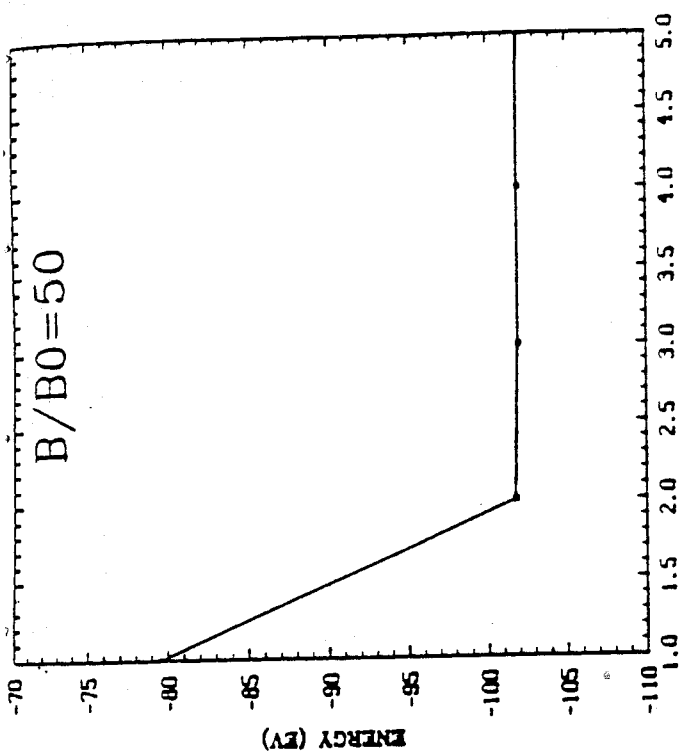
B/B0=50
ENERGY (EV)
ITERATION

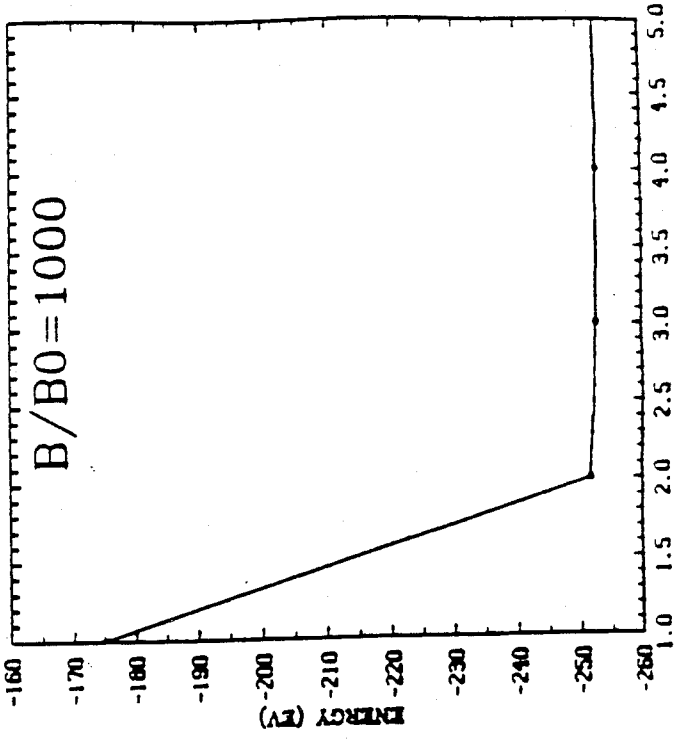
B/B0=1000
ENERGY (EV)
ITERATION

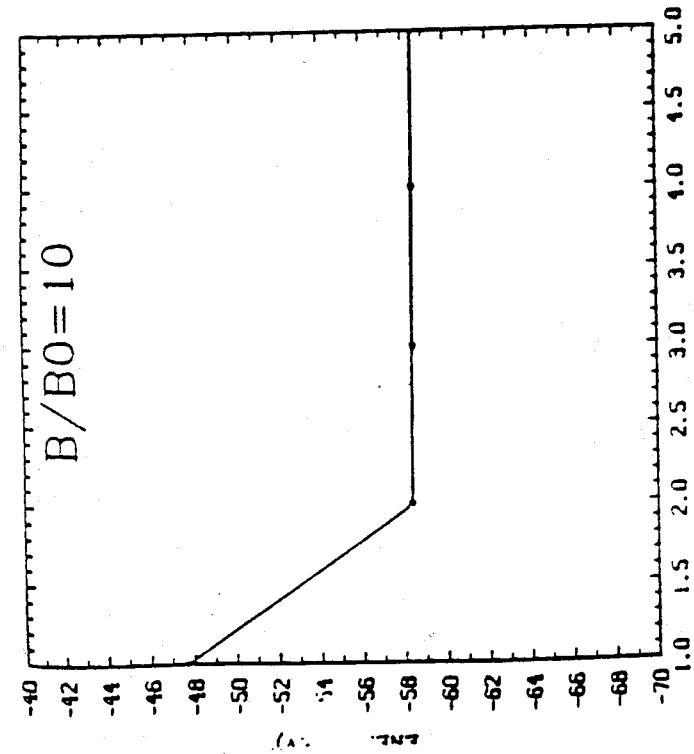
B/B0=10
ITERATION

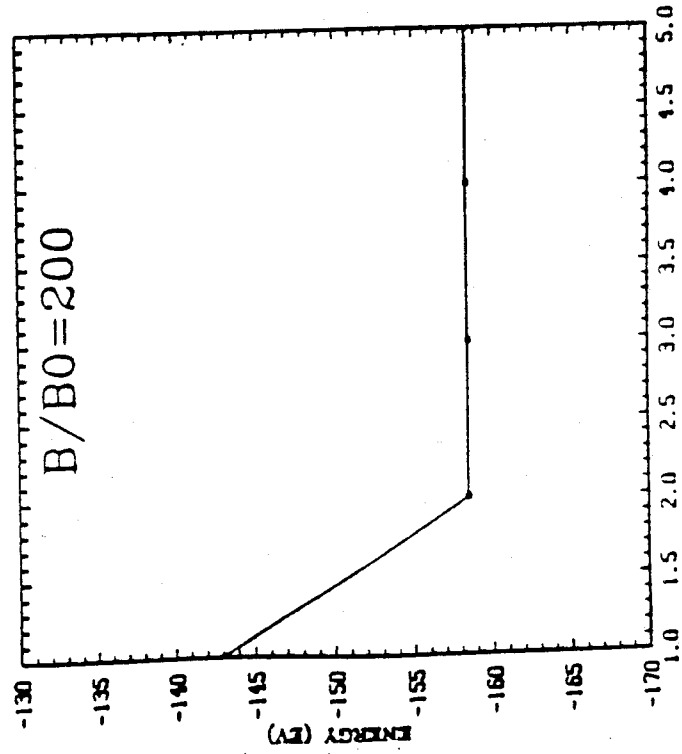
B/B0=200
ENERGY (EV)
ITERATION

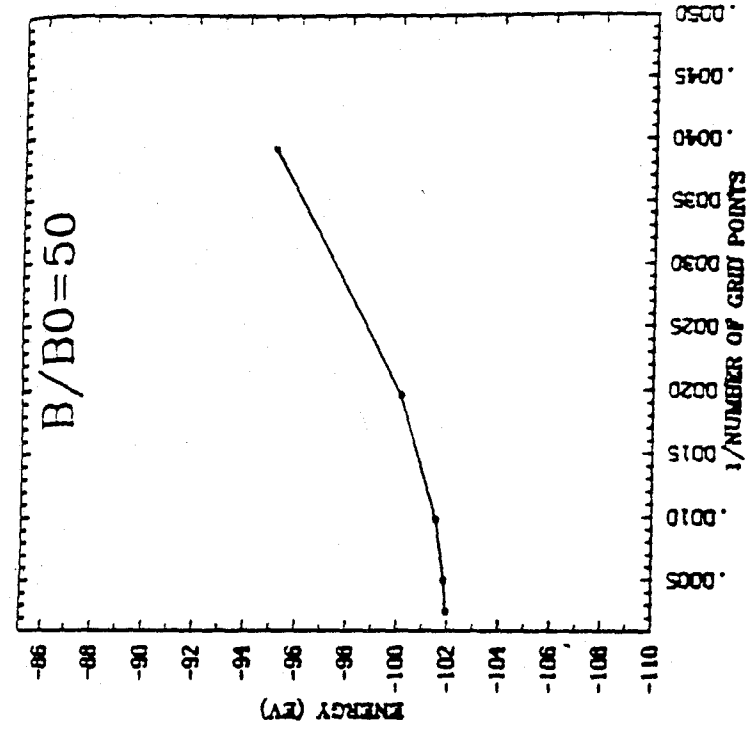
B/B0=50
ENERGY (EV)
1/NUMBER OF GRID POINTS

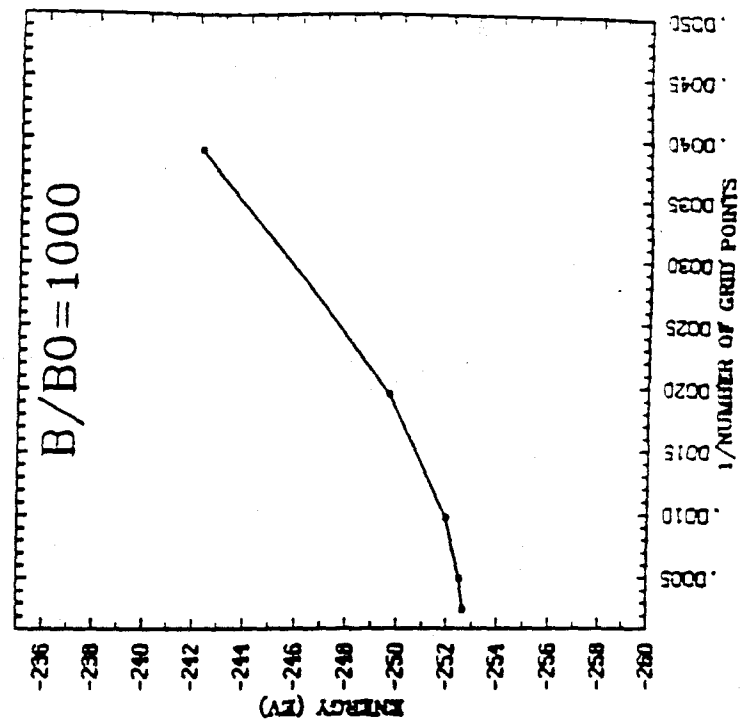
B/B0=1000
ENERGY (EV)
1/NUMBER OF GRID POINTS

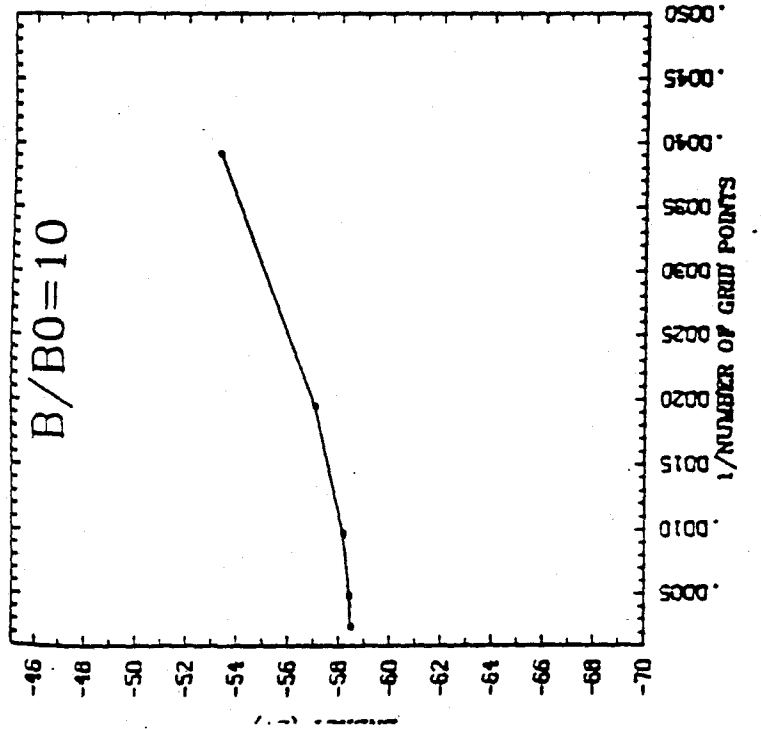
B/B0=10
1/NUMBER OF GRID POINTS

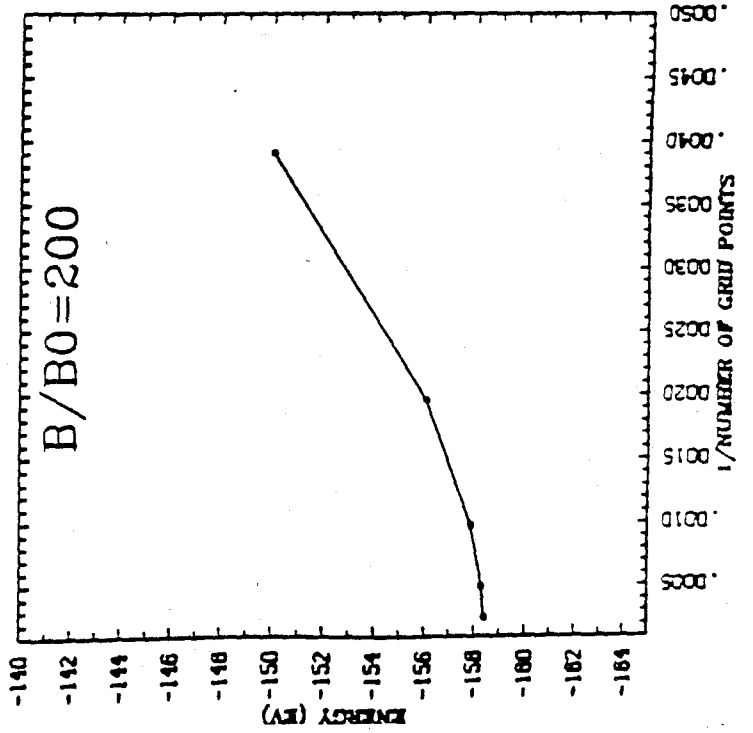
B/B0=200
ENERGY (EV)
1/NUMBER OF GRID POINTS

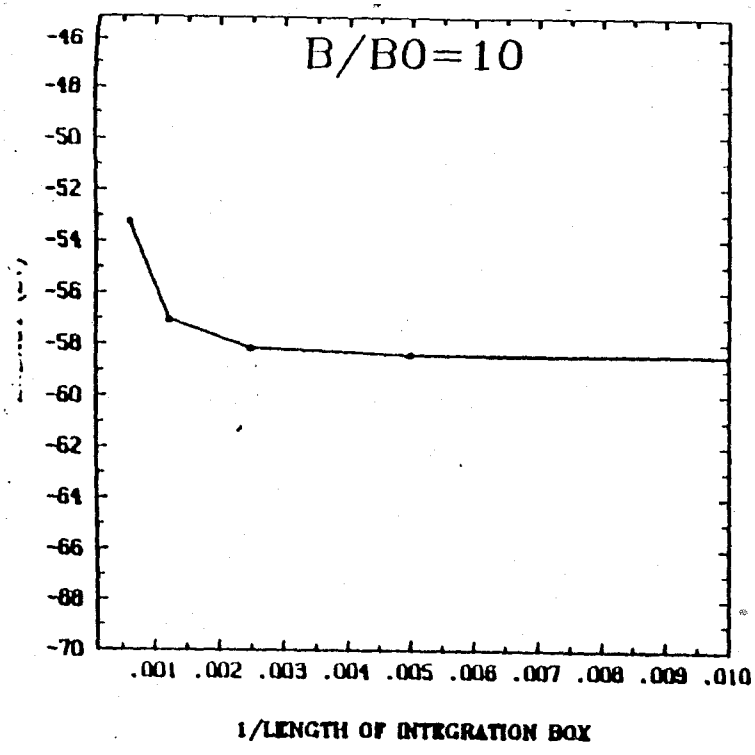
B/B0=10
-46
-48
-50
-52
-54
-56
-58
-60
-62
-64
-66
-68
-70
.001 .002 .003 .004 .005 .006 .007 .008 .009 .010
1/LENGTH OF INTEGRATION BOX

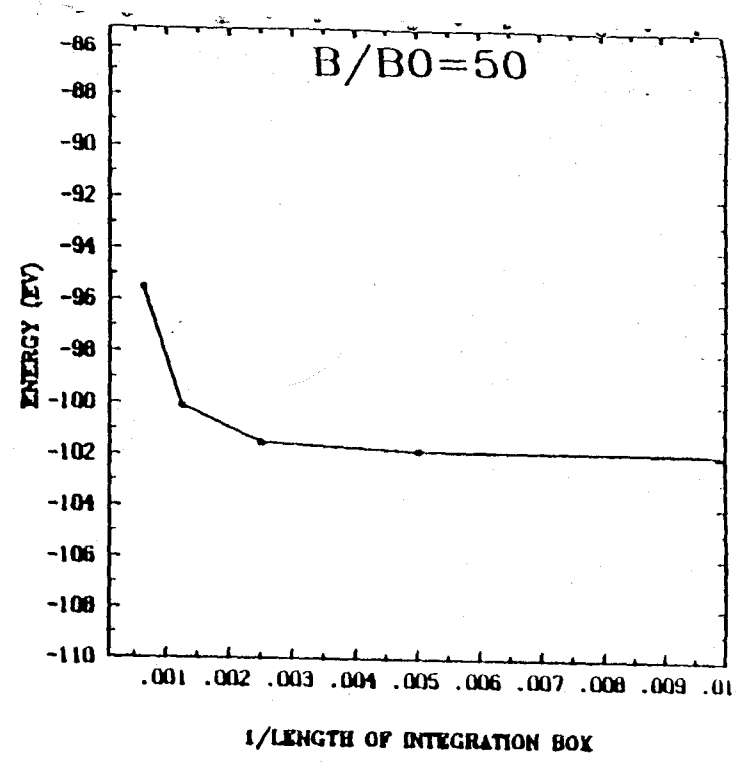
B/B0=50
ENERGY (EV)
-86
-88
-90
-92
-94
-96
-98
-100
-102
-104
-106
-108
-110
.001 .002 .003 .004 .005 .006 .007 .008 .009 .010
1/LENGTH OF INTEGRATION BOX

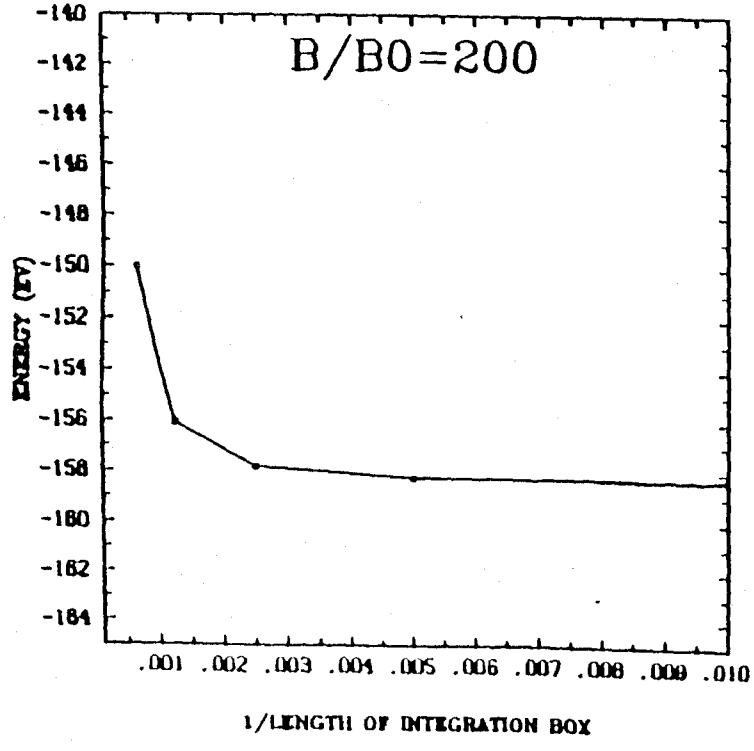
B/B0=200
ENERGY (EV)
-140
-142
-144
-146
-148
-150
-152
-154
-156
-158
-160
-162
-164
.001 .002 .003 .004 .005 .006 .007 .008 .009 .010
1/LENGTH OF INTEGRATION BOX

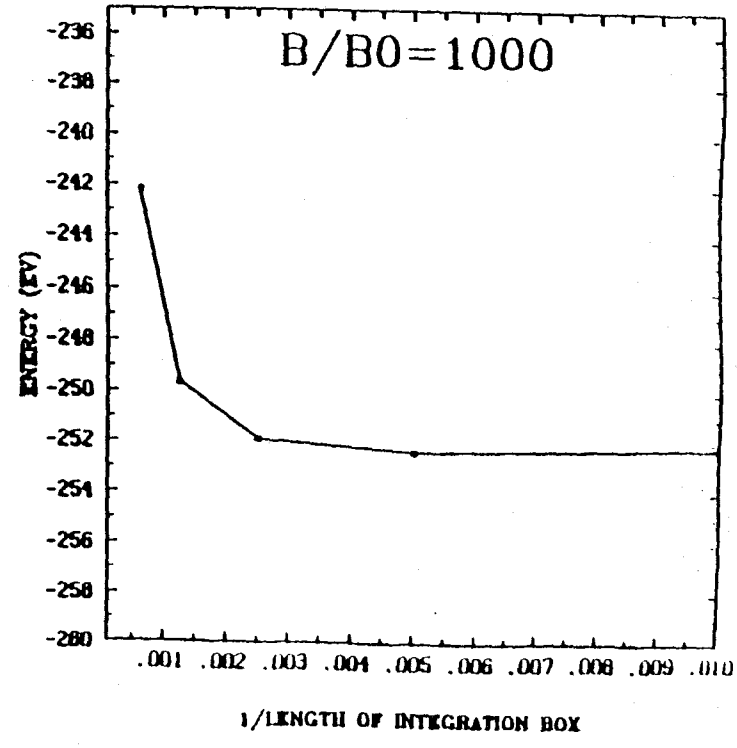
B/B0=1000
ENERGY (EV)
-236
-238
-240
-242
-244
-246
-248
-250
-252
-254
-256
-258
-260
.001 .002 .003 .004 .005 .006 .007 .008 .009 .010
1/LENGTH OF INTEGRATION BOX

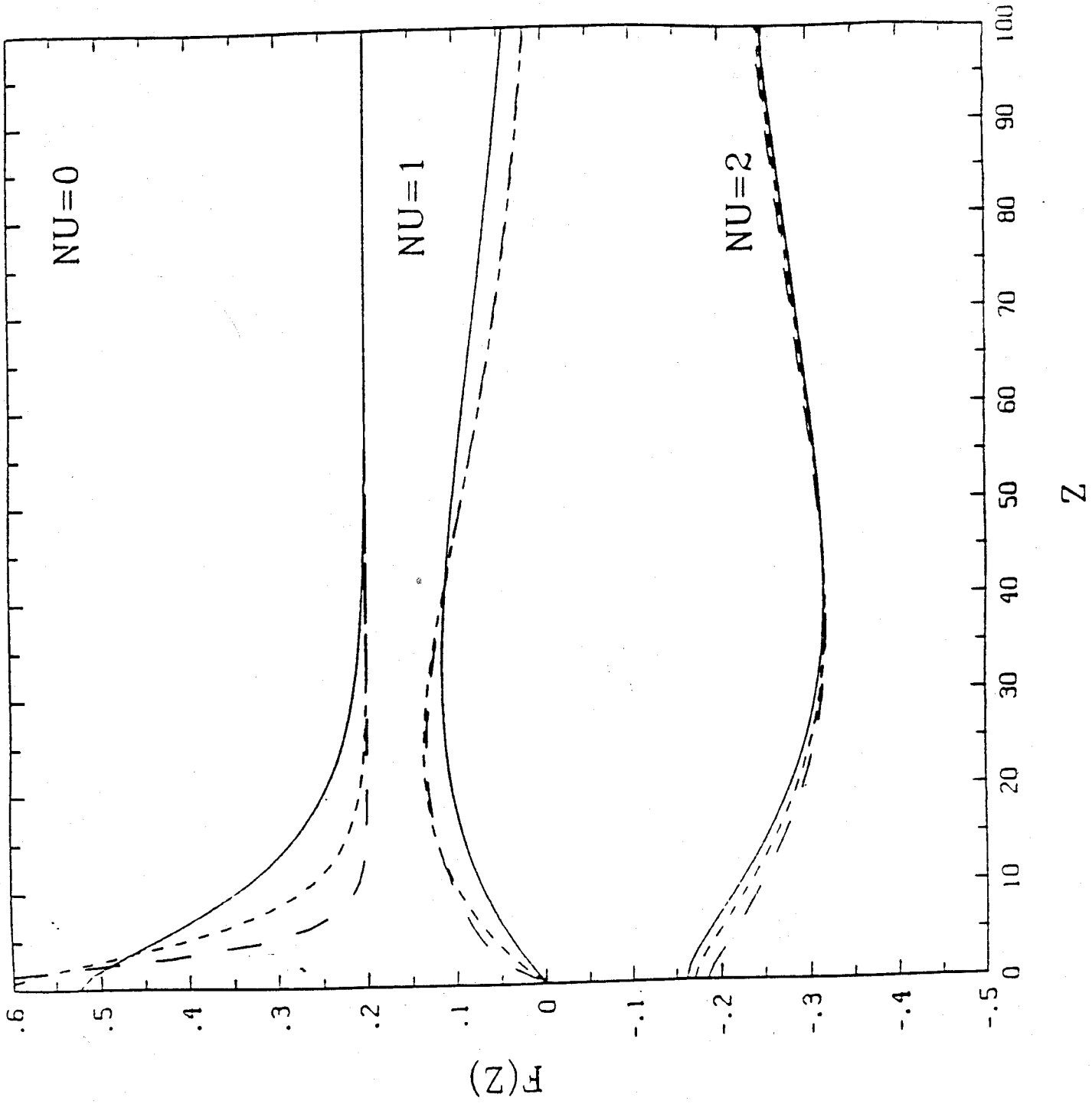
NU=0
NU=1
NU=2
F(Z)
Z
.6
.5
.4
.3
.2
.1
0
-.1
-.2
-.3
-.4
-.5
0
10
20
30
40
50
60
70
80
90
100

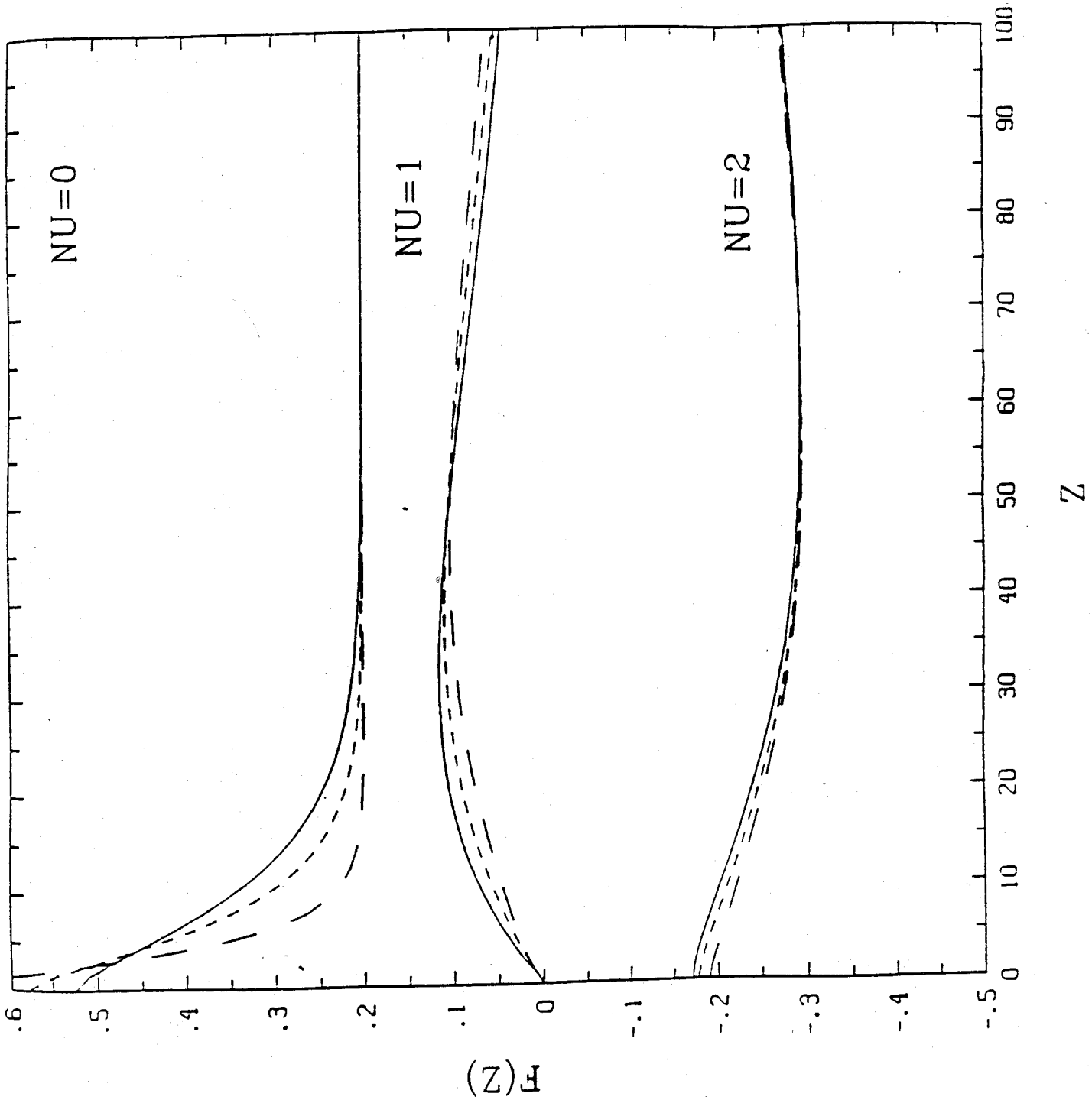
NU=0
NU=1
NU=2
F(Z)
Z
.6
.5
.4
.3
.2
.1
0
-.1
-.2
-.3
-.4
-.5
0
10
20
30
40
50
60
70
80
90
100

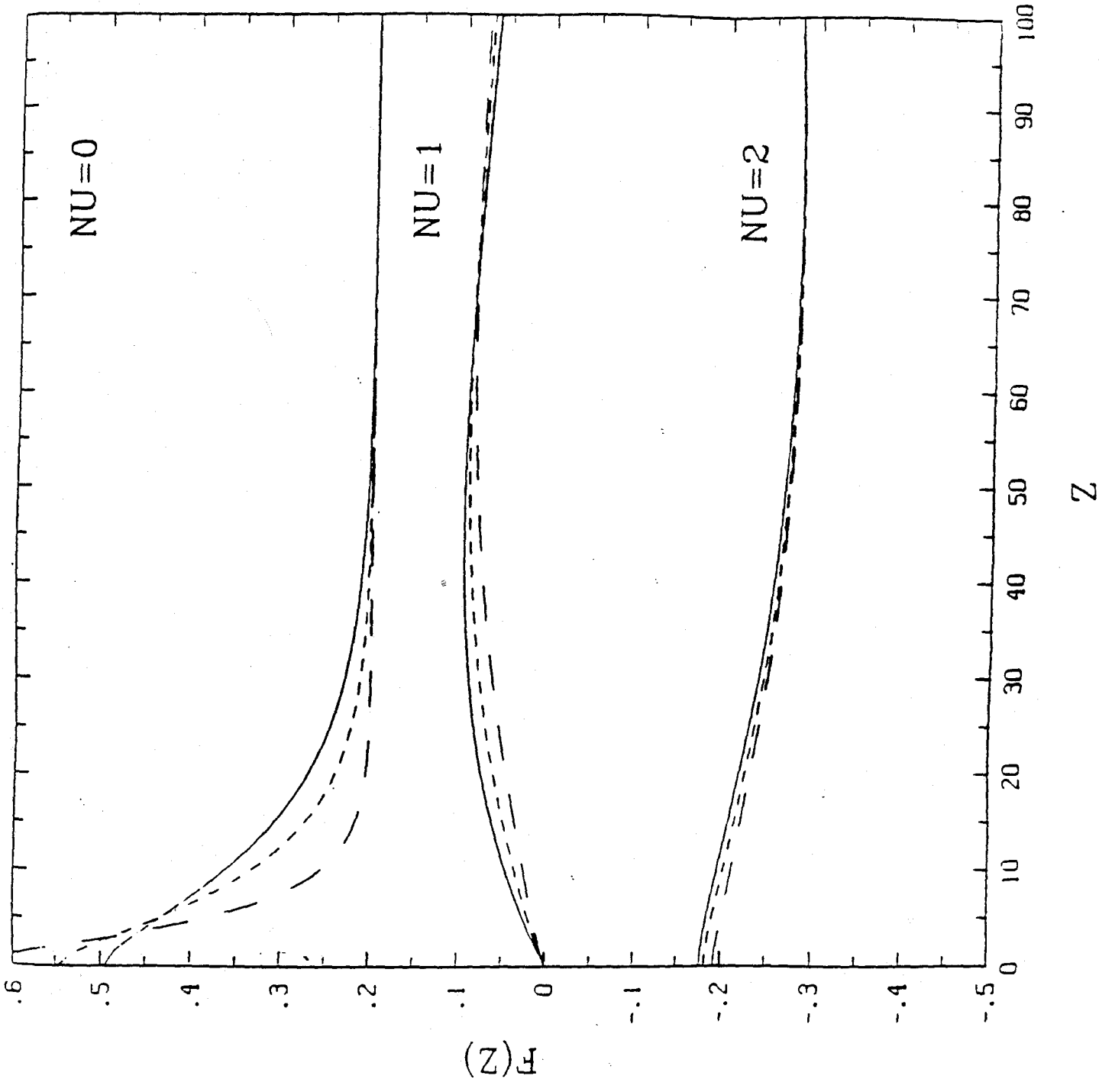
NU=0
NU=1
NU=2
.6
.5
.4
.3
.2
.1
0
-.1
-.2
-.3
-.4
-.5
0
10
20
30
40
50
60
70
80
90
100
F(Z)
Z

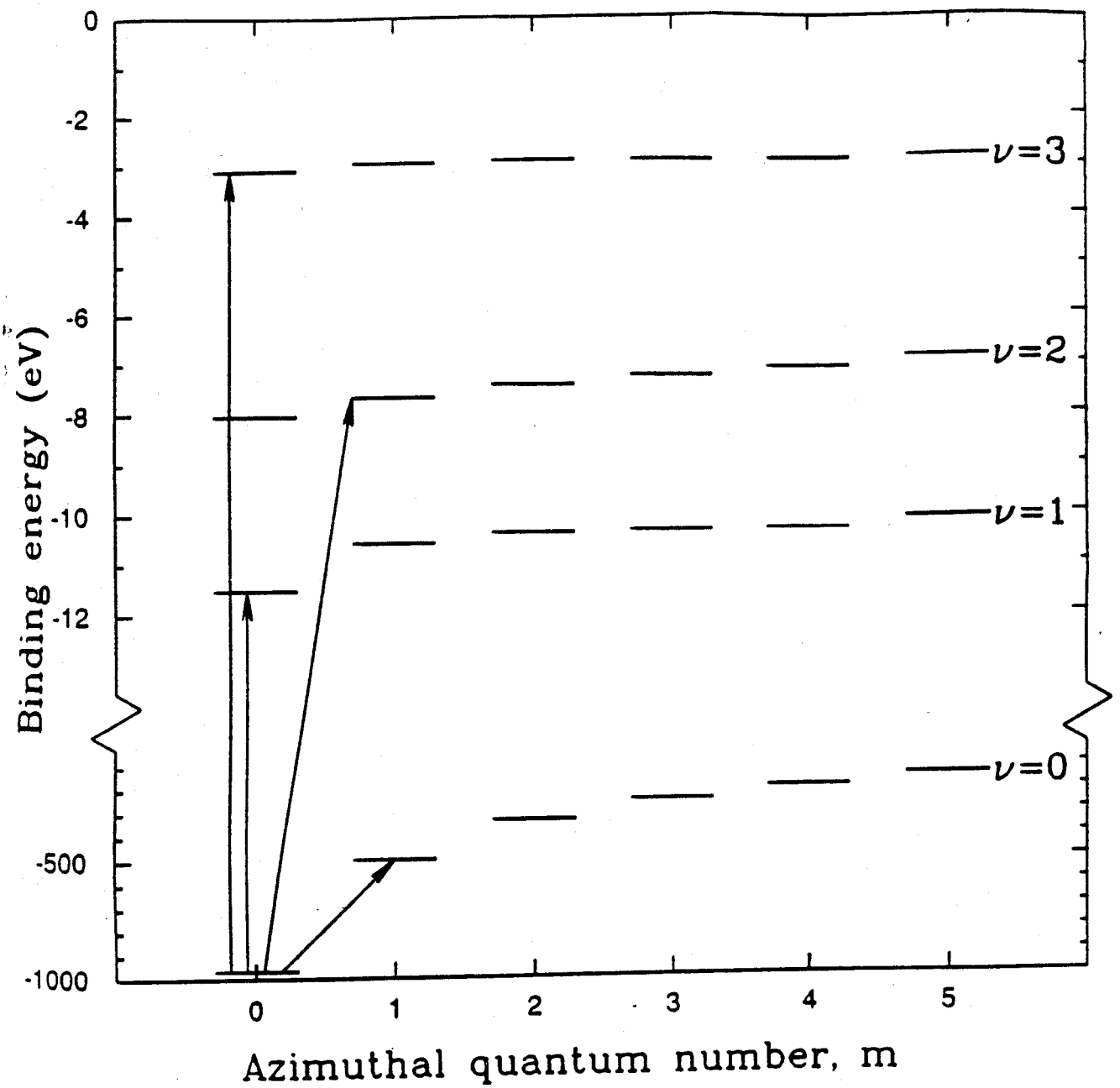
0
-2
-4
-6
-8
-10
-12
-500
-1000
Binding energy (eV)
ν=3
ν=2
ν=1
ν=0
0
1
2
3
4
5
Azimuthal quantum number, m

Chapter 2: Atomic Data for Neutron Star Model Atmospheres

M. C. Miller†

†Theoretical Astrophysics, California Institute of Technology, Pasadena, California 91125 USA

Abstract. In order to construct model atmospheres for neutron stars and predict their thermal X-ray spectra, it is necessary to generate high magnetic field atomic data for several atoms. We calculate the energy levels, wavefunctions and transition rates of hydrogen, helium and carbon, nitrogen and silicon and their ions in three representative magnetic fields ($B = 9.4 \times 10^{11}$G, $B = 2.35 \times 10^{12}$G and $B = 4.7 \times 10^{12}$G), as might be expected in neutron stars. The wavefunctions are represented in terms of Landau states, and are calculated with a high-field multiconfigurational Hartree-Fock code as described in Miller and Neuhauser 1990. We compare our results for hydrogen with previous work and use our wavefunctions to compute bound-free oscillator strengths for heavier elements. These data will be used to compute model atmospheres in a future paper.

1. Introduction

Ever since it was derived from magnetic dipole models that many pulsars have magnetic field strengths in excess of 10^{12}G, it has been realized that very strong magnetic fields are of astrophysical importance. This impression has been strengthened by the recent detection of cyclotron lines indicative of $\sim 2 \times 10^{12}$G fields in two gamma-ray bursts (Murakami *et al* 1988), which are believed to be associated with neutron stars. One question which has been raised is what effect fields of this strength have on the atmosphere of neutron stars. This question is of some importance in constructing cooling curves, because though the presence of an atmosphere will not significantly modify the total emission from a neutron star (Hernquist 1985), it may affect the emission in the sensitivity bands of satellites such as Einstein or ROSAT (Romani 1987). A first step is to consider the effect of high fields on atoms.

In the past decade a good deal of study has been done on the behavior of atoms in strong magnetic fields. Most of this work has concentrated on hydrogen, with semianalytic and numerical work being done by Simola and Virtamo 1978, O'Connell 1979, Kara and McDowell 1980, Wunner *et al* 1981, Rösner *et al* 1983, Rösner *et al* 1984, Forster *et al* 1984, Ruder *et al* 1985, Wunner 1986, Wunner and Ruder 1987, and Wunner *et al* 1987 among others. However, hydrogen is not the only element which may be present on a neutron star's surface. Because of thermonuclear burning and density stratification, the core of the pre-supernova star is expected to be primarily iron. The mass cut is defined to be the boundary between the material which is pushed outward and that which is pushed inward in the supernova explosion. From numerical simulations we expect the mass cut to occur in the iron core, so we might expect that the surface of neutron stars would be primarily iron. However, there are several complicating factors. There might be fall-back from the shells of the star, which could mean that silicon, aluminum, magnesium, neon, oxygen, nitrogen, carbon, helium or hydrogen could contribute

significantly. This is further muddied by the probability that there is significant mixing of the shells due to a Rayleigh-Taylor instability at the shell boundaries. Additionally, elements with higher atomic number might be created by spallation, since the gravitational potential at the surface of a neutron star is on the order of 100MeV per nucleon.

Once the neutron star is clear of the supernova remnant, it will start to accrete from the interstellar medium (ISM). Since the ISM is primarily hydrogen, it might seem that after sufficient time hydrogen would dominate the surface. However, if neutron stars have magnetic fields in the 10^{12}G range, the accretion will be funneled to the magnetic polar caps. This material will be prevented from diffusing across field lines to the rest of the star's surface, and some simulations have shown that the cap would be stable even against thermonuclear explosions. However, if the magnetic field is initially small then this would not be as strong an effect, and even if the star were born with very high fields it is possible that the material could fall "between the field lines" and thus spread out over the surface of the star.

If a sufficiently thick layer of hydrogen is built up on the surface, then low-temperature or "pycnonuclear" fusion might transform the hydrogen into helium, so that helium would be the dominant element. This could also be true of the helium→carbon reaction, or any of the other reactions in the fusion progression, or it could be that the heat generated would cause the hydrogen to fuse through to iron and we would end up with iron as the primary element again. In any case, the surface gravity of a neutron star is so large that density stratification will take place in $\sim 1 - 100$s. In addition, for the energy range considered in this paper, 1eV-10keV, only $\sim 10^{14}$g$= 10^{-19} M_{\odot}$ of matter is necessary for optical depth unity. Therefore the surface composition of a neutron star will be a pure element, and high-field atomic data must be computed for many elements to simulate the range of possible neutron star surfaces. A first step in this direction was taken by

Miller and Neuhauser (hereafter MN), who calculated wavefunctions, energies and radiative cross sections for hydrogen, helium and carbon in a variety of magnetic fields.

Because the ionization potential of atoms in strong magnetic fields is significantly greater than that at $B = 0$, one might expect that the number density of ions would be much smaller. However, Khersonskij 1987 showed that while for a surface temperature $T < 5 \times 10^5$K, the increase of magnetic field strength induces the decrease of the degree of ionization; for $T > 5 \times 10^5$K, the increase of field causes the increase of ionization. It is therefore important to consider all the ionization states of an atom when producing model atmospheres.

This paper extends the work of MN by calculating energies and bound-free cross sections for hydrogen, helium, carbon, nitrogen, silicon and their ions in fields typical of young neutron stars. In Section 2, I give a brief summary of the scaling arguments for hydrogen in strong magnetic fields. In Section 3, I discuss the method used for, and the results of, the calculations presented in this paper, including some rough error estimates. Finally, in Section 4, I present the conclusions.

2. Parameters in strong fields

In a very strong uniform magnetic field, the wavefunction of an atom may be approximated by a thin cylinder, with the long axis along the field. Accordingly, a cylindrical coordinate system is set up, with ρ being the radial coordinate, ϕ being the azimuthal coordinate, and z being the coordinate along the field. The quantum numbers for these coordinates are, respectively, n, m and ν.

As derived in, e.g., Ruderman 1971, a hydrogenic electron in its ground state $n = m = \nu = 0$ in the limit $B \to \infty$ has radial extent

$$\hat{\rho} = \left(\frac{\hbar c}{eB}\right)^{1/2} = 2.5 \times 10^{-10} B_{12}^{-1/2} \mathrm{cm} \qquad (1)$$

and longitudinal extent

$$l \sim \left(\frac{a_0/Z\hat{\rho}}{ln(a_0/Z\hat{\rho})} \right) \hat{\rho}, \tag{2}$$

where $a_0 = 5.1 \times 10^{-9}$cm is the Bohr radius and Z is the atomic number of the atom. The energy of this ground-state configuration is approximately

$$E \sim -Z^2 \frac{\hbar^2}{M a_0^2} \ln^2 \left(\frac{a_0}{Z\hat{\rho}} \right). \tag{3}$$

A state with $\nu > 0$ has roughly constant energy (Landau and Lifshitz 1977), so that, for example, the energy of a $\nu = 1$ state of hydrogen is about 10-13eV regardless of magnetic field, once the critical field is exceeded.

The critical field is defined as the field at which the magnetic force and Coulomb force are equal. This depends on the state that the electron is in, and is given by

$$B_m \approx \frac{Z^2}{(2m+1)^3} B_C, \tag{4}$$

where $B_C = 2.35 \times 10^9$G is the critical field for the ground state of hydrogen. The cylindrical approximation is truly valid only for $B \gg B_m$, but in practice it gives fair accuracy for $B > B_m$. The scaling of this formula means that for Rydberg states $m \gg 1$, the high-field approximation is valid even for magnetic white dwarfs, $B \sim 10^8$G. It also means that for $B = 5 \times 10^{12}$G, which is the field strength inferred from some cyclotron lines from X-ray pulsars, even iron ($Z = 26$) may be treated in the high-field limit. For the rest of this paper I shall take as my reference field $B_0 \equiv 4.7 \times 10^9G= 2B_C$, to be consistent with tradition.

3. Results and error analysis

3.1 Wavefunctions and energies

The wavefunctions and energies for ions with more than one electron are generated by a multiconfigurational Hartree-Fock method, modified for a cylindrical

coordinate system. This means that the wavefunction of the electron is expanded as

$$\Psi_{m\nu}(z,\rho,\phi) = \sum_n f_{nm\nu}(z)\Phi_{nm}(\rho,\phi), \tag{5}$$

where the Φ_{nm} are the Landau states,

$$\Phi_{nm}(\rho,\phi) = \frac{\sqrt{n!}}{\sqrt{2\pi(n+|m|)!\hat{\rho}^2}}\left(\frac{\rho}{\sqrt{2}\hat{\rho}}\right)^{|m|} e^{-\rho^2/4\hat{\rho}^2} L_n^{|m|}\left(\frac{\rho^2}{2\hat{\rho}}\right) e^{-im\phi}, \tag{6}$$

where $L_n^{|m|}$ are the associated Laguerre polynomials. The z wavefunctions $f_{nm\nu}$ are integrated over an integration box of length L with a number of grid points N, where the results presented in this paper were generated with $N = 512$ and $L = 400\hat{\rho}$. See MN for an analysis of truncation and grid size errors.

In this code, a simplifying assumption is made, that the ρ quantum number $n = 0$. This is because at the field strengths considered here, $B > 10^{12}$G; the energy required to raise an electron to an excited cyclotron state $n > 0$ is $E \approx 11.5\text{keV}nB_{12}$, where $B_{12} = \frac{B}{10^{12}\text{G}}$, and this energy is much larger than the thermal energy expected of a young neutron star, $T \sim 10^6$K ≈ 100eV. See MN for a discussion of the details of the Hartree-Fock method and of some of the errors involved.

The important parameter for error estimation is $\beta = \frac{B}{B_m}$. When $\beta \sim 1$ the $n = 0$ approximation may be accurate only to 10%, while for $\beta > 100$ it is accurate to better than 1%. Since $\beta \approx 5$ for silicon ($Z = 14$) at $B = 4.7 \times 10^{12}$G , the innermost electron ($m = \nu = 0$) is not calculated with great accuracy. However, it can be shown (e.g., in MN) that in the limit $B \to \infty$ an atom of atomic number Z in the ground state will have electrons in the states $m = 0 \ldots Z-1, \nu = 0$. Thus, the other electrons have $m > 0$, and since $B_m \sim \frac{1}{(2m+1)^3}$, the calculation is much better. Furthermore, for the purpose of constructing model atmospheres, the outer electrons are more important, since in a thermal bath at $T \sim 10^6$K=100eV, it is much more likely that an electron with a binding energy of a few hundred eV will

be ionized than an electron with $E_b \approx 5500$eV. Another way of saying this is that the cylindrical approximation is good for model atmosphere construction when the cyclotron energy is much greater than the typical thermal energy.

To get a better quantitative idea of the magnitude of errors in my calculation, in the first part of Table 1 I compare my results for the energies of the ground state and the first excited state of hydrogen-like ions with the results of Rösner *et al.*, scaled appropriately. This scaling is given by

$$E_Z(B) = Z^2 E_H(B/Z^2), \tag{7}$$

where $E_Z(B)$ is the energy of the hydrogenic atom with atomic number Z at magnetic field B and $E_H(B/Z^2)$ is the energy of hydrogen at magnetic field B/Z^2 (Rösner *et al.* 1984). In all cases the ground-state energies agree to within $< 10\%$, and the excited-state energies agree within $< 1\%$. This is enough accuracy to do model atmosphere calculations for neutron stars, because the input parameters such as magnetic field and surface temperature are more than 10% uncertain. In the first parts of Tables 2 through 14, I present my results for ions with $Z > 1$. In these tables, it is understood that the energy given for an electron in a state $(m\nu)$ is the energy that that electron has when all other electrons are in their ground state.

3.2 Bound-free cross sections

From MN, the bound-free cross section at a frequency ω is

$$\begin{aligned}\sigma(\omega) = 2\pi\alpha\omega \sum_{m\nu} \Theta(\omega + \epsilon_{m\nu}) \sqrt{\frac{M}{E}} \Big[& \gamma_+ m\hat{\rho}^2 \Big| \int f_{m\nu} g(p,z) dz \Big|^2 \\ & + \gamma_- (m+1)\hat{\rho}^2 \Big| \int f_{m\nu} g(p,z) dz \Big|^2 \\ & + \gamma_z \Big| \int f_{m\nu} g(p,z) z dz \Big|^2 \Big],\end{aligned} \tag{8}$$

where

α is the fine structure constant

Θ is the step function,

$$\Theta(x) = 0 \text{ for } x < 0, \qquad = 1 \text{ for } x \geq 0 \tag{9}$$

M is the mass of the electron

E is the kinetic energy of the electron

$g(p,z)$ is the free wavefunction of the electron with momentum $p = \sqrt{2ME}$ at position z.

γ_+, γ_- and γ_z are polarization coefficients, which are defined as the fractions of light interacting with the atom that are polarized in the right circular, left circular, and z directions, where "circular" is defined with respect to the magnetic field. In these calculations we take $\gamma_+ = \gamma_- = \gamma_z = \frac{1}{3}$. See Miller 1990 for a discussion of polarization effects across the surface of a neutron star.

In the second part of Table 1 I give the values of the bound-free oscillator strengths from the ground states of hydrogenic ions and compare them with the extrapolation of values given in MN. From Rösner *et al.* 1984 this scaling is

$$f(B,Z) = Z^0 f(B/Z^2, 1), \tag{10}$$

where the oscillator strength f is defined to be

$$\int \sigma(\omega) d\omega = \frac{2\pi^2 e^2}{mc} f. \tag{11}$$

The integral is evaluated at 100 values of frequency, logarithmically spaced from 1eV to 10keV, and increasing the number of frequencies to 1000 was found to change the oscillator strengths by less than 10%. Notice that Table 1b shows that the oscillator strengths are consistent to within 20% of what was given in MN. As with the energies, this error is acceptable because it is overwhelmed by the errors in the input parameters. Tables 2b through 14b give the oscillator strengths from the ground states of atoms with $Z > 1$.

4. Conclusions

Because neutron stars have extremely large magnetic fields, the prediction of the thermal spectra of these objects requires the generation of high-field atomic data, including energies and cross sections. The results presented in this paper provide the basis for the modeling of the atmospheres of neutron stars, which can significantly modify their thermal emission of soft X-rays. A future paper will present the predictions of these model atmospheres, with a particular emphasis on how they affect the interpretation of soft X-ray data from satellites such as Einstein, ROSAT and AXAF.

References

Forster, H., Strupat, W., Rösner, W., Wunner, G., Ruder, H., and Herold, H. 1984 *J. Phys. B: At. Mol. Phys.*, **17**, 1301.

Hernquist, L. 1985 *Ph.D. thesis*, California Institute of Technology.

Kara, S. M., and McDowell, M. R. C. 1980 *J. Phys. B: At. Mol. Phys.*, **13**, 1337.

Khersonskij, V. K. 1987, *Astron. Zh.*, **64**, 433.

Miller, M. C.1990 (in preparation).

Miller, M. C., and Neuhauser, D. 1990 (in preparation).

Neuhauser, D. 1986 *PhD thesis*, California Institute of Technology.

Neuhauser, D., Langanke, K., and Koonin, S. E. 1986 *Phys. Rev. A*, **33**, 2084.

O'Connell, R. F. 1979 *Phys. Lett.*, **70A**, 389.

Pröschel, P., Rösner, W., Wunner, G., Ruder, H., and Herold, H. 1982 *J. Phys. B: At. Mol. Phys.*, **15**, 1959.

Romani, R. W. 1987 *Astrophys. J.*, **313**, 718.

Rösner, W., Herold, H., Ruder, H., and Wunner, G. 1983 *Phys. Rev. A*, **28**, 2071.

Rösner, W., Wunner, G., Herold, H., and Ruder, H. 1984 *J. Phys. B: At. Mol. Phys.*, **17**, 29.

Ruder, H., Herold, H., Rösner, W., and Wunner, G. 1985 *Physica B and C* **127**, 11.

Ruderman, M. A. 1971 *Phys. Rev. Lett.*, **27**, 1306.

Shapiro, S., and Teukolsky, S. 1983 *Black Holes, White Dwarfs and Neutron Stars* (New York: Wiley).

Simola, J., and Virtamo, J. 1978 *J. Phys. B: At. Mol. Phys.*, **11**, 3309.

Wunner, G. 1986 *J. Phys. B: At. Mol. Phys.*, **19**, 1623.

Wunner, G., Geyer, F., and Ruder, H. 1987 *Astro. Sp. Sc.* **131**, 595.

Wunner, G., and Ruder, H. 1987 *Phys. Scr.*, **36**, 291.

Wunner, G., Ruder, H., and Herold, H. 1980 *Phys. Lett.* **79A**, 159.

— 1981 *J. Phys. B: At. Mol. Phys.*, **14**, 765.

Table 1

Binding energies and bound-free oscillator strengths for hydrogenic ions. The reference field is B0=4.7E9G. The energies in parentheses are the extrapolated values of Rosner et al. 1984, and the oscillator strengths in parentheses are the extrapolated values of Miller and Neuhauser 1990.

Energies

B/B0=200

Z	m	nu=0	nu=1
1	0	158(159)	13(13)
2	0	408(412)	52(50)
6	0	1653(1773)	382(378)
7	0	2050(2162)	496(494)

B/B0=500

Z	m	nu=0	nu=1
1	0	208(208)	13(13)
2	0	546(545)	52(52)
6	0	2313(2393)	419(415)
7	0	2871(2968)	552(552)

B/B0=1000

Z	m	nu=0	nu=1
1	0	252(253)	13(13)
2	0	676(670)	53(53)
6	0	2850(3051)	439(439)
7	0	3669(3754)	586(585)
14	0	8714(9367)	2060(2038)

Oscillator strengths

B/B0=200

Z	m	nu=0
1	0	0.28(0.29)
2	0	0.19(0.22)
6	0	0.10
7	0	0.11

B/B0=500

Z	m	nu=0
1	0	0.33(0.34)
2	0	0.25(0.27)
6	0	0.13(0.16)
7	0	0.13(0.15)

B/B0=1000

Z	m	nu=0
1	0	0.37(0.37)
2	0	0.30(0.30)
6	0	0.17(0.20)
7	0	0.14(0.18)
14	0	0.03

Table 2

Binding energies and bound-free oscillator strengths for helium-like ions. The reference field is B0=4.7E9G, and all energies are given in eV.

B/B0=200

		Energies		Oscillator strengths
Z	m	nu=0	nu=1	nu=0
2	0	271	12	0.49
	1	156	12	0.37
6	0	1500	290	0.12
	1	962	246	0.09
7	0	1870	380	0.13
	1	1194	338	0.09

B/B0=500

		Energies		Oscillator strengths
Z	m	nu=0	nu=1	nu=0
2	0	365	12	0.47
	1	212	13	0.37
6	0	2060	290	0.20
	1	1366	275	0.12
7	0	2622	420	0.16
	1	1701	382	0.12

B/B0=1000

		Energies		Oscillator strengths
Z	m	nu=0	nu=1	nu=0
2	0	447	12	0.55
	1	265	14	0.45
6	0	2580	310	0.21
	1	1800	240	0.15
7	0	3363	460	0.17
	1	2202	408	0.14
14	0	8312	1800	0.03
	1	5570	1601	0.06

Table 3

Binding energies and bound-free oscillator strengths for lithium-like ions. The reference field is B0=4.7E9G, and all energies are given in eV.

B/B0=200

		Energies		Oscillator strengths
Z	m	nu=0	nu=1	nu=0
6	0	1335	200	0.15
	1	838	170	0.11
	2	637	157	0.09
7	0	1686	290	0.16
	1	1073	260	0.11
	2	816	232	0.08

B/B0=500

		Energies		Oscillator strengths
Z	m	nu=0	nu=1	nu=0
6	0	1949	200	0.23
	1	1182	180	0.20
	2	909	173	0.18
7	0	2374	290	0.19
	1	1517	280	0.15
	2	1170	261	0.12

B/B0=1000

		Energies		Oscillator strengths
Z	m	nu=0	nu=1	nu=0
6	0	2400	200	0.25
	1	1500	180	0.22
	2	1150	180	0.19
7	0	3034	310	0.20
	1	1954	290	0.17
	2	1523	278	0.15
14	0	8022	1650	0.05
	1	5225	1350	0.06
	2	4200	1298	0.06

Table 4

Binding energies and bound-free oscillator strengths for beryllium-like ions. The reference field is B0=4.7E9G, and all energies are given in eV.

B/B0=200

		Energies		Oscillator strengths
Z	m	nu=0	nu=1	nu=0
6	0	1287	115	0.22
	1	715	105	0.17
	2	534	95	0.14
	3	425	91	0.13
7	0	1568	200	0.20
	1	939	180	0.13
	2	713	165	0.11
	3	574	151	0.10

B/B0=500

		Energies		Oscillator strengths
Z	m	nu=0	nu=1	nu=0
6	0	1637	105	0.28
	1	1003	105	0.22
	2	765	105	0.19
	3	609	98	0.18
7	0	2176	200	0.23
	1	1319	180	0.18
	2	1020	180	0.15
	3	827	168	0.17

B/B0=1000

		Energies		Oscillator strengths
Z	m	nu=0	nu=1	nu=0
6	0	2005	105	0.40
	1	1255	105	0.31
	2	955	105	0.27
	3	800	100	0.22
7	0	2757	200	0.25
	1	1696	180	0.24
	2	1316	180	0.18
	3	1080	173	0.18
14	0	7601	1350	0.05
	1	5013	1250	0.08
	2	3979	1150	0.07
	3	3354	1065	0.05

Table 5

Binding energies and bound-free oscillator strengths for boron-like ions. The reference field is B0=4.7E9G, and all energies are given in eV.

B/B0=200

		Energies		Oscillator strengths
Z	m	nu=0	nu=1	nu=0
6	0	1064	53	0.30
	1	592	45	0.26
	2	427	44	0.26
	3	338	44	0.21
	4	268	42	0.20
7	0	1442	125	0.20
	1	810	105	0.20
	2	595	95	0.17
	3	485	95	0.14
	4	397	89	0.13

B/B0=500

		Energies		Oscillator strengths
Z	m	nu=0	nu=1	nu=0
6	0	1460	45	0.36
	1	831	45	0.33
	2	604	45	0.34
	3	479	43	0.28
	4	385	45	0.27
7	0	1987	115	0.29
	1	1144	105	0.26
	2	855	105	0.22
	3	692	98	0.19
	4	573	97	0.23

B/B0=1000

		Energies		Oscillator strengths
Z	m	nu=0	nu=1	nu=0
6	0	1850	43	0.49
	1	1050	43	0.46
	2	810	42	0.38
	3	600	42	0.42
	4	500	40	0.32
7	0	2503	105	0.31
	1	1470	105	0.30
	2	1106	105	0.26
	3	897	95	0.26
	4	749	99	0.23
14	0	7396	1250	0.08
	1	4707	1050	0.11
	2	3683	950	0.08
	3	3178	950	0.07
	4	2746	872	0.08

Table 6

Binding energies and bound-free oscillator strengths for carbon-like ions. The reference field is B0=4.7E9G, and all energies are given in eV.

B/B0=200

		Energies		Oscillator strengths
Z	m	nu=0	nu=1	nu=0
6	0	1011	12	0.42
	1	499	11	0.48
	2	331	10	0.60
	3	247	10	0.46
	4	193	10	0.44
	5	144	10	0.44
7	0	1278	60	0.28
	1	697	50	0.24
	2	490	45	0.25
	3	386	45	0.25
	4	316	42	0.23
	5	256	41	0.19

B/B0=500

		Energies		Oscillator strengths
Z	m	nu=0	nu=1	nu=0
6	0	1373	10	0.58
	1	693	10	0.63
	2	466	10	0.60
	3	350	10	0.57
	4	275	10	0.54
	5	208	10	0.51
7	0	1760	45	0.34
	1	977	45	0.40
	2	695	43	0.32
	3	549	43	0.33
	4	454	43	0.30
	5	371	44	0.25

B/B0=1000

		Energies		Oscillator strengths
Z	m	nu=0	nu=1	nu=0
6	0	1712	10	0.74
	1	880	10	0.74
	2	597	10	0.70
	3	452	10	0.68
	4	357	10	0.62
	5	272	10	0.56
7	0	2222	43	0.51
	1	1247	42	0.44
	2	896	42	0.48
	3	713	43	0.38
	4	592	43	0.35
	5	487	45	0.30
14	0	7106	1050	0.08
	1	4429	870	0.10
	2	3417	780	0.10
	3	2913	770	0.08
	4	2550	730	0.07
	5	2272	706	0.08

Table 7

Binding energies and bound-free oscillator strengths for nitrogen-like ions. The reference field is B0=4.7E9G, and all energies are given in eV.

B/B0=200

		Energies		Oscillator strengths
Z	m	nu=0	nu=1	nu=0
7	0	1190	10	0.45
	1	603	10	0.43
	2	398	10	0.46
	3	295	10	0.50
	4	232	10	0.42
	5	186	10	0.47
	6	142	10	0.41

B/B0=500

		Energies		Oscillator strengths
Z	m	nu=0	nu=1	nu=0
7	0	1635	10	0.48
	1	843	10	0.53
	2	562	10	0.66
	3	420	10	0.62
	4	332	10	0.51
	5	269	10	0.57
	6	207	10	0.59

B/B0=1000

		Energies		Oscillator strengths
Z	m	nu=0	nu=1	nu=0
	0	2055	10	0.81
	1	1075	10	0.84
	2	724	10	0.72
	3	543	10	0.67
	4	433	10	0.69
	5	352	10	0.65
	6	273	10	0.59
14	0	6843	870	0.11
	1	4188	720	0.12
	2	3204	660	0.12
	3	2703	650	0.11
	4	2351	610	0.09
	5	2115	600	0.07
	6	1885	564	0.07

Table 8

Binding energies and bound-free oscillator strengths for oxygen-like silicon. The reference field is B0=4.7E9G, and all energies are given in eV.

Energies

B/B0=1000
Ground energy=30298

m	nu=0	nu=1
0	6629	730
1	3984	600
2	3006	550
3	2464	500
4	2155	500
5	1895	455
6	1727	455
7	1557	439

Oscillator strengths

B/B0=1000

m	nu=0
0	0.12
1	0.13
2	0.17
3	0.13
4	0.11
5	0.093
6	0.093
7	0.086

Table 9

Binding energies and bound-free oscillator strengths for fluorine-like silicon. The reference field is B0=4.7E9G, and all energies are given in eV.

Energies

B/B0=1000
Ground energy=31571

m	nu=0	nu=1
0	6381	550
1	3760	455
2	2791	420
3	2267	390
4	1949	380
5	1707	350
6	1540	340
7	1410	340
8	1273	330

Oscillator strengths

B/B0=1000

m	nu=0
0	0.12
1	0.16
2	0.14
3	0.15
4	0.13
5	0.13
6	0.14
7	0.12
8	0.098

Table 10

Binding energies and bound-free oscillator strengths for neon-like silicon. The reference field is B0=4.7E9G, and all energies are given in eV.

Energies

B/B0=1000
Ground energy=32595

m	nu=0	nu=1
0	6186	420
1	3568	340
2	2598	310
3	2070	280
4	1741	260
5	1531	260
6	1377	260
7	1238	240
8	1135	240
9	1024	236

Oscillator strengths

B/B0=1000

m	nu=0
0	0.16
1	0.20
2	0.18
3	0.20
4	0.16
5	0.17
6	0.16
7	0.15
8	0.14
9	0.12

Table 11

Binding energies and bound-free oscillator strengths for sodium-like silicon. The reference field is B0=4.7E9G, and all energies are given in eV.

Energies

B/B0=1000
Ground energy=33396

m	nu=0	nu=1
0	5994	290
1	3372	220
2	2405	200
3	1882	180
4	1572	180
5	1351	170
6	1200	170
7	1085	170
8	991	170
9	893	155
10	801	155

Oscillator strengths

B/B0=1000

m	nu=0
0	0.17
1	0.20
2	0.23
3	0.30
4	0.28
5	0.20
6	0.18
7	0.20
8	0.19
9	0.18
10	0.17

Table 12

Binding energies and bound-free oscillator strengths for magnesium-like silicon. The reference field is B0=4.7E9G, and all energies are given in eV.

Energies

B/B0=1000
Ground energy=33998

m	nu=0	nu=1
0	5822	180
1	3198	125
2	2232	115
3	1715	105
4	1394	98
5	1180	95
6	1030	95
7	912	90
8	823	90
9	749	90
10	680	90
11	602	90

Oscillator strengths

B/B0=1000

m	nu=0
0	0.17
1	0.28
2	0.30
3	0.31
4	0.32
5	0.31
6	0.28
7	0.25
8	0.42
9	0.31
10	0.24
11	0.22

Table 13

Binding energies and bound-free oscillator strengths for aluminum-like silicon. The reference field is B0=4.7E9G, and all energies are given in eV.

Energies

B/B0=1000
Ground energy=34421

m	nu=0	nu=1
0	5656	80
1	3037	51
2	2065	45
3	1549	43
4	1235	43
5	1019	39
6	869	39
7	757	39
8	672	39
9	603	39
10	544	39
11	488	39
12	423	39

Oscillator strengths

B/B0=1000

m	nu=0
0	0.28
1	0.28
2	0.38
3	0.43
4	0.40
5	0.40
6	0.43
7	0.37
8	0.47
9	0.40
10	0.39
11	0.35
12	0.37

Table 14

Binding energies and bound-free oscillator strengths for silicon-like silicon. The reference field is B0=4.7E9G, and all energies are given in eV.

Energies

B/B0=1000
Ground energy=34683

m	nu=0	nu=1
0	5502	13
1	2885	10
2	1911	9
3	1397	9
4	1080	9
5	868	9
6	718	9
7	609	9
8	525	9
9	460	9
10	407	9
11	360	9
12	314	9
13	262	9

Oscillator strengths

B/B0=1000

m	nu=0
0	0.28
1	0.45
2	0.44
3	0.71
4	0.53
5	0.73
6	0.74
7	0.85
8	0.66
9	0.81
10	0.69
11	0.60
12	0.69
13	0.60

Chapter 3: Model Atmospheres for Neutron Stars

M C Miller†

†Theoretical Astrophysics, California Institute of Technology, Pasadena, California 91125 USA

Abstract. While the presence of an atmosphere on a neutron star will not significantly modify its total thermal emission, it may change the emission in the sensitivity bands of detectors such as Einstein or ROSAT so that the inferred surface temperature (from a blackbody curve) may be quite different from the actual surface temperature. This in turn may affect deduced cooling curves. Previous calculations of model atmospheres of neutron stars have used atomic data calculated for zero magnetic field. However, many neutron stars are expected to have extremely high magnetic fields, on the order of $B \geq 10^{12}$G, and it is important to take this into account. This paper uses atomic data in high magnetic fields computed using a multiconfigurational Hartree-Fock code, and the data was presented in Miller 1990. The effects of ionization and polarization in strong magnetic fields are discussed, and the prospects for observation by satellites are investigated.

1. Introduction

SN1987A is now more than three years old, and as the expanding gas shell that surrounds it becomes optically thin, there is the possibility that a central neutron star will be observed. Because of its youth, this object would have a relatively high surface temperature, so that its thermal flux might be observable. The planned ROSAT and AXAF missions may be able to detect such an object, and they have great enough sensitivity that they may be able to detect thermal radiation from other sources, such as the Crab or Vela pulsars. The determination of surface temperatures from X-ray observations will set constraints on the cooling curves of neutron stars, and thus will give valuable clues to the interior structure of these objects (see e.g. Tsuruta 1986). Preliminary models of neutron star atmospheres (Romani 1987) indicate that even more stringent limits may be placed on the cooling curves, because the surface temperature inferred from the flux in the Einstein sensitivity band is much greater than the actual surface temperature. However, these models have not included the effect of magnetic fields.

Ginga observations of the gamma-ray bursts GB870303 and GB880205 show (Murakami *et al.* 1988) absorption features at ~20keV and ~40keV, which may be interpreted as being due to cyclotron absorption in a magnetic field $B > 10^{12}$G. This is more convincing than previous claims of cyclotron resonance in gamma-ray bursts (which had only one harmonic), though it is somewhat suspicious that the same energies are observed in two separate bursts. Fields of this strength dominate the physics of the surface, and in particular they shift the energy levels of the atoms. A great deal of work has been done to compute the wavefunctions, energy levels and radiative cross sections for hydrogen in high fields (e.g. Simola and Virtamo 1978, O'Connel 1979, Kara and McDowell 1980, Wunner *et al.* 1980, Rösner *et al.* 1983, Rösner *et al.* 1984, Forster *et al.* 1984, Ruder *et al.* 1985, Wunner 1986, Wunner and Ruder 1987), and similar calculations have been done for helium and

carbon (Miller and Neuhauser). The need to consider many different compositions is due to the large variety of processes that can contribute to the makeup of the surface. For example, iron could be the dominant element because current models predict that the mass cut of the supernova occurs in the iron layer. Hydrogen could be important because it is the most abundant element accreted once the neutron star starts interacting with the interstellar medium. Other elements such as helium or carbon could contribute, either because the neutron star might accrete from the supernova shells or because fusion may take place on the star's surface. The situation is somewhat simplified because the lightest element present will dominate the opacity. An optical depth of unity in X-rays requires only about 10^{14}g of material (Romani 1987), and the surface gravity is high enough that gravitational separation will take place in only $\sim 1 - 100$s (Alcock and Illarionov 1980), so only pure element surface compositions need be considered.

In this paper, we use cross sections computed from the wavefunctions of atoms and ions in high fields to construct model atmospheres for neutron stars. We consider relatively low temperatures, $T = 10^5$ to 10^6K, consistent with the upper limits derived from X-ray observations. In Section 2, we describe our method for producing local thermodynamic equilibrium (LTE) models, including the Khersonskij 1987 high-field modification of the Saha ionization equation. In Section 3, we produce spectra for several combinations of parameters and discuss the effect on observable lines of the variation of the magnetic field over the surface of the star, and in Section 4 we consider the effect of these results on color temperatures and cooling curves.

2. Model Atmospheres

2.1 Iteration procedure and temperature correction

The calculation of our LTE model atmospheres follows the standard treatment given by Mihalas (1978) for plane parallel atmospheres. The assumption that the

atmosphere is plane parallel is much better for neutron stars than for main sequence stars, because for soft X-rays at optical depth unity, the atmosphere has a thickness < 1cm, small compared to the neutron star radius of $\sim 10^6$ cm. The computation works on a grid of 100 zones, arranged logarithmically in Rosseland optical depth from 10^{-3} to 10^2. The iteration towards the temperature profile starts with an initial guess, taken as that of gray opacity,

$$T = T_0(\tau_R + q)^{1/4}, \tag{1}$$

where τ_R is the Rosseland optical depth and $q \approx 0.71044$ to ensure agreement with the exact gray solution at large depth. The photon frequencies are also arranged logarithmically, with 100 levels from 1eV to 10keV. Hydrostatic equilibrium is imposed by

$$\frac{d\mathrm{P}}{d\tau_R} = \frac{g_s}{\kappa_R(\tau_R)}, \tag{2}$$

where g_s is the surface gravity, P is the pressure and κ_R is the Rosseland opacity. The equation of state is used to determine the density from the pressure. It is demonstrated in Section 2.3 below that on the surface an ideal gas equation of state holds, so that

$$P = nkT. \tag{3}$$

Following Mihalas (1978), the flux is computed at each level of the atmosphere from

$$F_\nu(\tau) = 2\int_\tau^\infty B_\nu[T(t)]E_2(t-\tau)dt - 2\int_0^\tau B_\nu[T(t)]E_2(\tau - t)dt, \tag{4}$$

where $B[T(t)]$ is the Planck function and $E_2(t-\tau)$ is the second exponential function. Note that this assumes that the source function is equal to the Planck function. This is reasonably accurate, because in the frequency range considered, absorption dominates scattering.

The number density of neutral atoms, singly ionized atoms, etc. in each level of the atmosphere is determined by solving the ionization equation, and when the flux

is calculated, the Lucy-Unsöld procedure is used to impose flux constancy. This method estimates the temperature correction at a given level by

$$\Delta T(\tau) \approx \frac{T(\tau)^{-3}}{16\sigma_R}\left(\frac{\kappa_J}{\kappa_P}\left[3\int_0^\tau \frac{\kappa_F(\tau')}{\kappa_R(\tau')}\Delta F(\tau')d\tau + 2\Delta F(0)\right] - \frac{\kappa_R}{\kappa_P}\frac{d\Delta F(\tau)}{d\tau_R}\right), \quad (5)$$

where $\kappa_R, \kappa_F, \kappa_P$and κ_J are the Rosseland, flux, Planck and absorption mean opacities. The approximation $\kappa_J = \kappa_P$ was found to give sufficient accuracy. After the new temperature profile is found, hydrostatic equilibrium is reestablished, the ionization equations are solved again, a new flux table is computed, and the process is iterated. Five iterations are usually sufficient to produce flux constancy to within $< 1\%$ throughout the atmosphere.

2.2 Line broadening in strong magnetic fields

In the high-density, high-temperature environment of a neutron star's atmosphere, spectral lines will be substantially broadened. Because of the complexities involved in an accurate calculation of broadening, this effect will be ignored in this paper. However, in this section some rough estimates are made to determine when line opacity is important.

Because the Rosseland mean opacity is weighted by the derivative of the Planck function with respect to temperature, $\frac{dB_\nu}{dT}$, the greatest weight is put on frequencies near $\hbar\omega = 4kT$. We consider transitions from the ground state to the first excited state, so the line center is at about 150eV to 250eV if the magnetic field is between $B = 10^{12}$G and $B = 5 \times 10^{12}$G. If the temperature is between $T = 10^5$K and $T = 10^6$K, the greatest weight is put on $\hbar\omega = 4kT$ ≈30eV to 350eV, which is $\sim 10 - 100$eV away from the center of the line, so collisional broadening is most important. The opacity at this frequency from bound-bound transitions will be compared to the opacity from bound-free transitions, so that an order-of-magnitude estimate of the importance of bound-bound transitions may be made.

The assumption is made that the change in frequency that is due to an encounter may be described by the Weisskopf approximation

$$\Delta\omega = \frac{C_p}{r^p}, \tag{6}$$

where r is the distance between the atom and perturber, and for example $p = 2$ is appropriate for the linear Stark effect, whereas $p = 3$ represents resonance broadening. It is assumed that when the frequency is within some critical frequency of the line center,

$$\Delta\omega < \Delta\omega_g, \tag{7}$$

the cross section has a Lorentz form,

$$\sigma \propto \frac{1/2\pi\tau}{(\Delta\omega)^2 + (1/2\tau)^2}, \tag{8}$$

where τ is the mean time between collisions. The critical frequency $\Delta\omega_g$ is assumed to be the Weisskopf frequency

$$\Delta\omega_g \approx \Delta\omega_w = \left(\frac{v^p}{C_p\psi_p^p}\right)^{1/p}, \tag{9}$$

where ψ_p is a phase shift: $\psi_2 = \pi$, $\psi_3 = 2$. Outside of this frequency, $\Delta\omega > \Delta\omega_g$, it is assumed that statistical broadening theory is applicable. The frequency dependence is different in a neutron star atmosphere than in laboratories, because the strong magnetic field constrains the atoms, ions and electrons to move in one dimension. It is therefore necessary to rederive $\sigma(\Delta\omega)$ in one dimension, and this is now done using the approximation that the nearest neighbor is responsible for the frequency shift.

The probability $W(r)$ that the nearest neighbor lies at a distance r is

$$W(r) = n_1 e^{-rn_1}. \tag{10}$$

Here n_1 is the linear number density of the perturbers along the field line, so that if the number density is $n\text{cm}^{-3}$ and the area of the magnetic flux tube is $A\text{cm}^2$, then $n_1 = nA\text{cm}^{-1}$. Here A is roughly given by

$$A = \pi\hat{\rho}^2,$$

where

$$\hat{\rho} = \left(\frac{\hbar c}{eB}\right) = 2.5 \times 10^{-10}\frac{B}{10^{12}\text{G}}\text{cm} \tag{11}$$

is the radius of the first Landau level. Defining the normal phase shift $\Delta\omega_0$ by

$$\Delta\omega_0 = \frac{C_p}{r_0^p}, \tag{12}$$

where r_0 is the mean interparticle distance $r_0 = \frac{1}{n_1}$, we see that

$$\left(\frac{\Delta\omega}{\Delta\omega_0}\right)^{1/p} = \frac{r_0}{r}. \tag{13}$$

Setting $\beta = \frac{\Delta\omega}{\Delta\omega_0}$ and substituting, we find that

$$W(\beta)d\beta = \frac{1}{p}\beta^{-1-1/p}e^{-\beta^{-1/p}}d\beta. \tag{14}$$

This compares with the three-dimensional value of

$$W(\beta)d\beta = \frac{3}{p}\beta^{-1-3/p}e^{-\beta^{-3/p}}d\beta, \tag{15}$$

so in the presence of a strong magnetic field, the line opacity drops off less sharply. The cross section integrated over all frequencies is

$$\int_0^\infty \sigma d\omega = \frac{2\pi^2 e^2}{mc}f, \tag{16}$$

where the oscillator strength $f \approx 1$. Using this and the assumptions above, the line cross section for $\Delta E >$1eV and $n_7 < 1$, where ΔE is the "distance" from the line center and $n_1 = 10^7 n_7\text{cm}^{-1}$ is

Stark broadening

$$\sigma_S \approx 3 \times 10^{-18} n_7 C_2^{1/2} \left(\frac{\Delta E}{1eV}\right)^{-3/2} \text{cm}^2, \tag{17}$$

Resonance broadening

$$\sigma_R \approx 10^{-15} n_7 C_3^{1/3} \left(\frac{\Delta E}{1eV}\right)^{-4/3} \text{cm}^2. \tag{18}$$

In three dimensions, $C_2 \approx 1\text{cm}^2/\text{s}$ and $C_3 \approx 5 \times 10^{-10}\text{cm}^3/\text{s}$.

To compare the bound-bound cross section to the bound-free cross section, we take as an example hydrogen at $B = 10^{12}$G. Here σ_S and σ_R are respectively the Stark and resonance cross sections of the transition $(m = 0,\ \nu = 0)$ to $(m = 0,\ \nu = 1)$ at the frequency $\hbar\omega = 4kT$. This is compared to the combined ionization cross sections σ_{bf} from the $(m = 0,\ \nu = 0)$ and $(m = 0,\ \nu = 1)$ states. The densities that are used to calculate σ_S and σ_R are the densities at unit Rosseland optical depth, which were calculated without including the line opacities. At $B = 10^{12}$G, the excitation energy of the $(m = 0,\ \nu = 1)$ state is 145eV, so this state is assumed to have $e^{-145\text{eV}/kT}$ of the population of the ground state, and $\Delta E = |145\text{eV} - 4kT|$.

At $T = 10^5\text{K} \Rightarrow 4kT = 34.6\text{eV}$,

$\rho = 120\text{g/cm}^3 \Rightarrow n_7 = 2.4$

$\sigma_s \approx 6 \times 10^{-21}\text{cm}^2$

$\sigma_r \approx 4 \times 10^{-21}\text{cm}^2$

$\sigma_{\text{bf}} \approx 4 \times 10^{-21}\text{cm}^2$

At $T = 3 \times 10^5\text{K} \Rightarrow 4kT = 104\text{eV}$,

$\rho = 0.4\text{g/cm}^3 \Rightarrow n_7 = 0.008$

$\sigma_s \approx 9 \times 10^{-23}\text{cm}^2$

$\sigma_r \approx 4 \times 10^{-23}\text{cm}^2$

$\sigma_{\text{bf}} \approx 1 \times 10^{-22}\text{cm}^2$

At $T = 10^6\text{K} \Rightarrow 4kT = 346\text{eV}$,

$\rho = 0.2\text{g/cm}^3 \Rightarrow n_7 = 0.004$

$\sigma_s \approx 4 \times 10^{-24}\text{cm}^2$

$\sigma_r \approx 3 \times 10^{-24}\text{cm}^2$

$\sigma_{\text{bf}} \approx 4 \times 10^{-20}\text{cm}^2$

From this, it is apparent that lines may have a very significant effect at low temperatures (because of the lack of other opacity sources), but that at high temperatures they may be ignored.

2.3 Equation of state in the atmosphere

In this paper the equation of state is assumed to be that of an ideal gas. In this section this assumption is justified by showing that in the photosphere the contributions to the pressure from electron degeneracy and ion corrections is negligible.

For a degenerate electron gas in one dimension, the number of states in a volume V and a range of z momenta Δp_z is given by

$$n = \frac{eBV\Delta p_z}{h^2 c} \tag{19}$$

(Landau and Lifshitz 1977), so the density and pressure are given by

$$n_e = \frac{eB}{h^2 c}\int_{-\infty}^{\infty} f\,dp_z \tag{20}$$

and

$$P = \frac{eB}{h^2 c}\int_{-\infty}^{\infty} pvf\,dp_z, \tag{21}$$

and for complete degeneracy the occupation number f is

$$\begin{aligned} f &= 1 \text{ for } |p| \le p_F \\ f &= 0 \text{ for } |p| > p_F \end{aligned} \tag{22}$$

where p_F is the Fermi momentum. Therefore,

$$n_e = \frac{2eB}{h^2 c} p_F. \tag{23}$$

The energies considered are much less than the electron rest mass m, so $v \approx p/m$ and

$$P \approx \frac{2eB}{3h^2 cm} p_F^3 \approx 7 \times 10^{17} B_{12}^{-2} n_{27}^3, \tag{24}$$

where $B = 10^{12} B_{12}\mathrm{G}$ and $n_e = 10^{27} n_{27} \mathrm{cm}^{-3}$. The pressure of an ideal gas is

$$P = nkT \approx 10^{17} n_{27} T_6, \tag{25}$$

where the temperature is $T = 10^6 T_6 \mathrm{K}$, so the two are equal at about $n_{27} = 0.4$ and degeneracy pressure may be ignored when $n_{27}^2 \ll 1$.

The interactions between atoms become important when the mean distance between atoms is comparable to the size of the ions. The outer electron of a neutral atom of atomic number Z in a strong magnetic field has an orbital radius of

$$\rho = \sqrt{(2Z-1)}\hat{\rho}$$

and a length along the field of (Miller and Neuhauser 1990)

$$l \approx \left(\frac{a_0/\hat{\rho}}{\ln(a_0/\hat{\rho})} \right) \hat{\rho}, \tag{26}$$

where a_0 is the Bohr radius, $a_0 = 5 \times 10^{-9} \mathrm{cm}$. The average distance between atoms is

$$r \approx \frac{1}{nA}, \tag{27}$$

where $A = \pi\rho^2 = \pi(2Z-1)\hat{\rho}^2$. The condition $r \gg l$ then yields $n_{27} \ll \frac{5}{2Z-1}$.

In order to determine whether these conditions are satisfied, it is necessary to estimate the number density in the photosphere. This may be done from the equation of hydrostatic equilibrium (2), which can be written in the form

$$\frac{dP}{d\tau} = \frac{g_s}{\sigma/\mu}, \tag{28}$$

where σ is some average cross section and μ is the mass of an atom. This may be directly integrated, and if an ideal gas equation of state $P = nkT$ is assumed, the number density is

$$n = \frac{g_s}{kT\sigma/\mu}\tau. \tag{29}$$

For typical values $g_s = 3 \times 10^{14}\mathrm{cm/s^2}$, $T = 10^5\mathrm{K}$, $\sigma = 10^{-21}\mathrm{cm^2}$ and $\mu = 10^{-23}\mathrm{g}$, the number density at the lower extreme of the atmosphere, $\tau = 100$, is $n = 2 \times 10^{25}\mathrm{cm^{-3}}$. Therefore, the conditions above are satisfied, and to a good approximation the equation of state is that of an ideal gas. Figure 1 compares the pressures given by various equations of state at a variety of values of the electron density. From this diagram, it is evident that the strong magnetic field plays an important part in the non-degeneracy of the atmosphere, and if the magnetic field were to decay away, the pressure would be dominated by electron degeneracy. Furthermore, at a frequency which has very low cross section (such as the higher frequencies in our model, $\omega \sim$10keV), the density at optical depth unity may be high enough that degenerate pressure is important at the 10% level.

2.4 High-field ionization

For a general multielectron atom, it is necessary to determine the number densities of all of the various ions of the atom. Khersonskij (1987) derived a high-field ionization equation to replace the Saha equation for hydrogen.

For a hydrogen atom, the neutral hydrogen density n_H at temperature T and magnetic field B is determined by

$$\frac{n_H}{n_p n_e} = \frac{1}{2}\left(\frac{2\pi\hbar^2}{m_e kT}\right)^{3/2} \frac{\sinh\eta_p}{\eta_p}\frac{\coth\eta_e}{\eta_e} e^{E_a/kT} f_H(B,T), \tag{30}$$

where

n_p is the proton density,

n_e is the electron density,

m_e is the mass of the electron,

$\eta_p = \frac{\hbar\omega_p}{2kT}$, where ω_p is the cyclotron energy, $\omega_p = \frac{eB}{m_p c}$,

$\eta_e = \frac{\hbar\omega_e}{2kT}$,

E_a is the magnitude of the ground state energy, and the partition function f_H is

$$f_H(B,T) = \sum_{s=0}^{\infty} e^{-\frac{E_a+\epsilon_s+m\hbar\omega_p}{kT}}, \tag{31}$$

where ϵ_s is the energy of the sth excited state, $\epsilon_s < 0$

and

$m\hbar\omega_p$ is the correction for finite proton mass, where m is the azimuthal quantum number.

For $Z > 1$, the natural generalization (corresponding to the Saha equation) is to replace m_p with m_N, the mass of the nucleus and replace

$$\frac{n_H}{n_p n_e} \tag{32}$$

with

$$\frac{n_r}{n_{r+1} n_e}, \tag{33}$$

where n_r is the number density of the r-times ionized ion.

For hydrogen, one can calculate the ionized fraction,

$$x_p = \frac{n_p}{n_t} = 1 - x_H, \tag{34}$$

where n_t is the total density of baryons, from

$$x_p = \sqrt{\frac{1}{4(Kn_t)^2} + \frac{1}{Kn_t}} - \frac{1}{2Kn_t} \tag{35},$$

where

$K \equiv \frac{n_H}{n_p n_e}$.

For example, for $B = 10^{12}$G and $T = 10^5$K, $x_p = 0.058$, whereas for $B = 10^{13}$G and $T = 10^6$K, $x_p = 2.2 \times 10^{-5}$, all assuming a total number density of $n_t = 10^{21}\text{cm}^{-3}$.

For an atom with atomic number Z, the ionization equations are of the form

$$\frac{n_r}{n_{r+1} n_e} = K_r, \tag{36}$$

where K_r is a constant given by the equations above. The total number density is

$$n_t = n_0 + n_1 + \ldots + n_Z, \tag{37}$$

and charge conservation gives

$$n_e = n_1 + 2n_2 + \ldots + Z n_Z. \tag{38}$$

We solve these equations by an iterative averaging method, which provides convergence at a level of 10^{-5} in less than ten steps.

Numerically, it is found that for hydrogen at $\rho = 1\text{g/cm}^3$ (appropriate for $\tau_R = 1$) and $T < 6 \times 10^5$K, an increase in magnetic field causes a decrease in ionization, while for $T > 6 \times 10^5$K, an increase in B causes an increase in ionization. This is because as the field increases, the binding energy increases but the phase space decreases, and at $T \approx 6 \times 10^5$K the two effects balance. However, for atoms with $Z > 1$ at $T < 10^6$K, an increase in magnetic field causes a decrease in ionization. Figures 2a, 2b, 2c and 2d show the fractions of neutral atoms at various values of the magnetic field and temperature for hydrogen, helium, carbon and nitrogen.

Therefore, for a given magnetic field, temperature, and total number density, the number densities of the ions may be calculated. For a given ion, it is assumed

that the ground state and excited states are distributed according to a Boltzmann law,

$$n \propto e^{-E/kT}. \tag{39}$$

3. Spectra

Model atmospheres have been calculated for surface compositions of pure hydrogen, pure helium, pure carbon, and pure nitrogen at equatorial magnetic fields of 9.4×10^{11}G, 2.35×10^{12}G and 4.7×10^{12}G (these values for B are multiples of the critical field at which magnetic effects dominate). Because the magnetic field varies over the surface of the star, it is important to account for this effect. It is also interesting to investigate the importance of polarization; these effects are considered in the following sections.

3.1 Interpolation of model atmospheres

If we assume that neutron stars have roughly dipolar magnetic fields, then the strength of the field varies by a factor of two from the magnetic equator to the magnetic pole. The presence of higher multipoles would create an even larger variation in the magnetic field. Since for our calculations we assume that the field is of such a strength that it dominates the energetics of the atom, the energy levels of atoms will be shifted dramatically between the equator and the poles. In order to account for this, it would seem reasonable to calculate cross section vs. frequency tables for many intermediate field strengths, then sum these over the surface of the star, appropriately weighted by projected area. However, the calculation of cross section tables for a given magnetic field B and atomic number Z is a process that takes several hours, and would be computationally more intensive than desirable. It is therefore worthwhile to search for approximations at intermediate fields.

The approximation we will make is that the cross sections are shifted in frequency by the amount that the ground state energy level changes, and in magnitude such that the integrated cross section is constant,

$$\int \sigma(B_1,\nu)d\nu = \int \sigma(B_2,\nu)d\nu. \tag{40}$$

Another way of saying this is that we assume that the oscillator strength of a given transition, $f = \frac{mc}{\pi e^2}\int \sigma d\nu$, is roughly constant with respect to magnetic field. For example, we would assume that for hydrogen

$$\sigma(B = 4.7\times 10^{12}G, \frac{253}{208}\nu) = \frac{208}{253}\sigma(B = 2.35\times 10^{12}G, \nu), \tag{41}$$

where $\sigma(B,\nu)$ is the cross section as a function of magnetic field and frequency. In order to make this approximation relevant to ions with $Z > 1$, we work from the Ruderman scaling formula (1), where B_c is the critical field, $B_0 = 2.35\times 10^9$G, in Ruderman's derivation but in our case B_c is determined from numerical simulations. Between 2.35×10^{12}G and 4.7×10^{12}G, the best fit to hydrogen ground state energies is given by $B_c = 2.8\times 10^9$G. Therefore, the ratio of the binding energy at an intermediate field, $B_{\rm int}$, to the binding energy at the low field, $B_{\rm low} = 2.35\times 10^{12}$G, is given approximately by

$$\frac{E_{\rm int}}{E_{\rm low}} \approx \frac{\ln^2(B_{\rm int}/(Z^2B_0))}{\ln^2(B_{\rm low}/(Z^2B_0))} \tag{42}$$

and our estimate for the cross section at intermediate field is

$$\sigma(B_{\rm int}, \frac{E_{\rm int}}{E_{\rm low}}\nu) = \sigma(B_{\rm low},\nu). \tag{43}$$

This approximation assumes that the scaling of energies is hydrogenic. This is fairly accurate for the outer electron of an atom, but breaks down for the inner electrons. However, this should not detract significantly from the computations because the ionization energies of the inner electrons are in the several hundred eV range, which

is substantially higher than the typical photon energy $\hbar\omega \sim 10\text{eV}-100\text{eV}$ from a thermal bath at $T \sim 10^5 - 10^6\text{K}$.

3.2 Effects of polarization

Calculations of radiative cross sections in strong magnetic fields, as might be found on the surface of a neutron star, have used the implicit assumption that if the radiation field is isotropic and unpolarized, then all polarization components will make equal contributions to the cross section. However, as indicated below, for bound-free interactions the component of polarization that is linear and parallel to the magnetic field axis (which we call the B polarization) is dominant. In this section, we first give an estimate of the ratio of the cross sections due to B and circular polarizations (where "circular" is defined with respect to the direction of the field, not the propagation direction of the photon), then estimate the impact of this ratio on the ionization process.

In a strong magnetic field, an atom is stretched along the field, with its length scale across the field given by

$$\hat{\rho} \approx 2.5 \times 10^{-10} B_{12}^{-1/2} \text{cm}, \tag{44}$$

where $B_{12} = \frac{B}{10^{12}\text{G}}$ and its length scale along the field given by

$$l \approx \left(\frac{a_0/Z\hat{\rho}}{\log(a_0/Z\hat{\rho})} \right) \hat{\rho}, \tag{45}$$

where a_0 is the Bohr radius, $a_0 \approx 5 \times 10^{-9}\text{cm}$, and Z is the atomic number of the atom. For example, for $Z = 1$ and $B_{12} = 1$, $l \approx 7\hat{\rho}$. Henceforth we will consider the hydrogen atom, $Z = 1$. We will use a cylindrical coordinate system, where z is the coordinate for the cylindrical axis, ρ is the radial coordinate, Φ is the azimuthal coordinate, and ν, n and m are their respective quantum numbers. We will assume that $n = 0$.

It is intuitively reasonable that for bound-free absorption, the B polarization should have a greater cross section than the circular polarization, because it is interacting with the long axis of the atom. To get an idea of how great the difference is, we will look at Coulomb wavefunctions in the limit of low kinetic energy, $E = \frac{p^2}{2M}$ small. In a strong field, the Schroedinger equation along the field is

$$-\frac{\hbar^2}{2m}\frac{\partial^2\psi}{\partial z^2} - \frac{e^2}{z}\psi = E\psi.$$

Using the substitutions

$$\rho = \frac{\sqrt{2mE}}{\hbar}z \text{ and } -2\eta = \frac{e^2}{\hbar}\sqrt{\frac{2m}{E}},$$

this becomes

$$\frac{d^2g}{d\rho^2} + \left(1 - \frac{2\eta}{\rho}\right)g = 0,$$

where $g(z)$ is the z-component of the wavefunction. This is the differential equation for the Coulomb functions, and in the limit $\rho \to 0$ and $\eta \to -\infty$ this becomes (see e.g. Abramowitz and Stegun 1972)

$$g(z) \approx \frac{z}{a_0} - \left(\frac{z}{a_0}\right)^2, \tag{46}$$

where $g(z)$ is the unbound wavefunction of the electron (this approximation is valid for $z < a_0$).

The circular cross section is given by

$$\begin{aligned}
\sigma_+ &\propto \left|\hat{\rho}\int_{-\infty}^{\infty} f_{m\nu}(z)g(z)dz\right|^2 \\
&= \left|\hat{\rho}\int_{-\infty}^{\infty} e^{-|z|/l}\left(\frac{z}{a_0} + \left(\frac{z}{a_0}\right)^2\right)dz\right|^2, \qquad (47) \\
&= \left|\frac{\hat{\rho}}{a_0}\int_{-\infty}^{\infty} e^{-|z|/l}\frac{z^2}{a_0}dz\right|^2
\end{aligned}$$

where $f_{m\nu}(z)$ is the z component of the bound wavefunction of the electron. We are considering only the ground state

$$f_{m\nu} = f_{00} \approx e^{-|z|/l}. \tag{48}$$

Similarly, the B polarization cross section is

$$\begin{aligned}\sigma_B &\propto |\int_{-\infty}^{\infty} z f_{m\nu}(z) g(z) dz|^2 \\ &= |\int_{-\infty}^{\infty} z e^{-|z|/l} (\frac{z}{a_0} + \left(\frac{z}{a_0}\right)^2) dz|^2 \\ &= \left|\int_{-\infty}^{\infty} e^{-|z|/l} \frac{z^2}{a_0} dz\right|^2.\end{aligned} \tag{49}$$

Therefore, the ratio is

$$\frac{\sigma_B}{\sigma_+} \approx \left(\frac{a_0}{\hat{\rho}}\right)^2, \tag{50}$$

which has a value of about 400 for $B = 10^{12}$G. This compares to a numerically determined value of about 10000 at the absorption edge, where the greater value is due to the increased binding energy in a strong magnetic field. The approximations used above are valid for

$$E \ll E_{\text{ground}}, \tag{51}$$

where E is the kinetic energy of the free electron and E_{ground} is the ground-state binding energy of the atom, about 160eV for $B = 10^{12}$G. In practice, the cross section that is due to B polarization remains much greater than that due to circular polarization even at higher energies, so that, for example, at $B = 4.7 \times 10^{12}$G, $E = 1000$eV, $\sigma_B = 5.4 \times 10^{-21}\text{cm}^2$ and $\sigma_+ = 3.4 \times 10^{-25}\text{cm}^2$. A similar ratio holds for ionization from excited states, so that it is a good approximation to assume that $\sigma_B \gg \sigma_+$ for all frequencies considered.

The total bound-free cross section has the form

$$\sigma_{\text{bf}} \sim \gamma_+ \sigma_+ + \gamma_- \sigma_- + \gamma_B \sigma_B, \tag{52}$$

where γ_+, γ_- and γ_B are the fractions of the light polarized in the right circular, left circular and magnetic field directions, respectively. A calculation done for a dipolar field indicates (see Appendix I) that in a strong field $\gamma_B \approx 0.4$, and since for $\sigma_B \gg \sigma_+$

$$\sigma_{bf} \approx \gamma_B \sigma_B,$$

the total cross section is about 20% greater than if the γ 's were equal.

We found that the surface gravity has a small effect on the unredshifted spectrum, as was also true in the nonmagnetic case (Romani 1986). In Figure 3 we see that the emergent spectrum for helium is very similar for surface gravities of 10^{14} and 10^{15}cm s^{-2} for $B = 4.7 \times 10^{12}$G and a surface temperature of 3×10^5K. As in the nonmagnetic case, what change there is in the spectrum is probably due to increased pressure ionization below the absorption edges in the high-gravity case. In the other spectra presented below, a surface gravity of 3×10^{14}cm s^{-2} is assumed.

In Figures 4, 5, 6 and 7 we show the unredshifted spectra from atmospheres with varying compositions and magnetic fields at an effective temperature of $T = 10^6$K. In Figures 8, 9, 10 and 11 we show the temperature as a function of Rosseland optical depth from these atmospheres, and in Figures 12, 13, 14 and 15 we show the pressure as a function of Rosseland optical depth.

4. Color temperatures and cooling curves

In Table 1 we list the blackbody temperatures associated with the various magnetic field values and surface compositions of the model atmospheres. In this table, $T_{\rm E}$ is defined as the temperature of the blackbody curve which gives the same number of counts as the model atmosphere in the sensitivity range of the *Einstein* IPC (0.5 to 5.0 keV), while $T_{\rm R}$ is defined similarly for the *ROSAT* HRI (0.1 to 2.0 keV). Here the response curve for the *Einstein* IPC is taken from Harnden *et al.* (1984)

and the response curve for the *ROSAT* HRI is taken from the ROSAT Mission Description, Table 4.4. We note that the ratio of blackbody temperature to effective temperature is very close to 1, with a minimum of 0.73 and a maximum of 1.37. This is in contrast to the results of Romani, who found that for $B = 0$ the temperature of a blackbody with the same number of counts in the Einstein band as the model atmosphere could be much higher than the effective temperature of the star. This is due to two effects which increase the opacity. First, the presence of a magnetic field shifts the energy levels of atoms upward so that the ionization edge is closer to the observed frequencies, which means that the opacity is higher. Second, in a strong field the bound-free cross section drops off as ν^{-2}, not ν^{-3} as in the non-magnetic case. Since the opacity is higher, the levels of the atmosphere which contribute to the spectrum are higher up, and consequently are cooler. Therefore, the flux is much closer to blackbody flux at the frequencies of interest.

Except in a few cases, X-ray observations of pulsars have provided only upper limits to their thermal flux. Exceptions include RCW 103, with an estimated blackbody temperature of 2.7×10^6K (Tuohy and Garmire 1980); PSR 1929+10, with $T_{\rm BB} \approx 2.0 \times 10^5$K (Helfand 1983); and PSR 0656+14, with $T_{\rm BB} \approx 3 - 6 \times 10^5$K (Cordova *et al.* 1989). Non-magnetic calculations indicated that the presence of an atmosphere could significantly affect the resultant surface temperature of these objects. In particular, if the surface temperature is much less than the blackbody temperature the star will have had to cool more quickly than is expected in the standard cooling model (see Tsuruta 1986 for a review). This may mean that the interior of neutron stars is composed of exotic states of matter such as pion condensates or quark matter, or it may just mean that effects in the standard model such as reheating of the star by differential superfluid rotation (see, e.g., Lamb and Shibazaki 1989) have not been fully taken into account.

Our results seem to indicate that the presence of an atmosphere does not significantly modify the blackbody temperature. This gives a reprieve to standard cooling models, which now have until the launches of ROSAT and AXAF to explain why neutron stars seem to cool faster than they ought.

Appendix I. Calculation of the polarization coefficients

Assuming that the source of radiation is initially isotropic and unpolarized, what fraction of the light that reaches the observer is right circular, left circular and B polarized after interacting with the atom? Our coordinates are set up so that the z axis is along the line of sight, and the magnetic field is in the $y-z$ plane and makes an angle of ψ with the z axis. As indicated in the figure, we assume that the initial ray comes from a direction that makes an angle of θ with the line of sight and ϕ with the x axis. Since the initial ray is unpolarized, it has equal components along both directions perpendicular to the initial direction. To determine the polarization coefficients γ_B, γ_+, and γ_-, we integrate the projections of these components along the $\hat{\mathbf{e}}_B, +$ and $-$ directions, multiplied by a weight function and normalized.

If we assume that the magnetic field is given by

$$\mathbf{B} = B_0 \hat{\mathbf{e}}_B, \tag{53}$$

where

$$\hat{\mathbf{e}}_B = (0, \sin\psi, \cos\psi), \tag{54}$$

then the polarization unit vectors are given by

$$\hat{\mathbf{e}}_B = (0, \sin\psi, \cos\psi), \tag{55}$$

$$\hat{\mathbf{e}}_+ = \frac{1}{\sqrt{2}}(1, i\cos\psi, -i\sin\psi), \tag{56}$$

$$\hat{\mathbf{e}}_- = \frac{1}{\sqrt{2}}(1, -i\cos\psi, i\sin\psi). \tag{57}$$

From the diagram, the initial direction of the ray is

$$\hat{\mathbf{e}} = (\cos\phi\sin\theta, \sin\phi\sin\theta, \cos\theta), \tag{58}$$

so the initial polarization will be composed of

$$\epsilon_{\perp 1} = \frac{1}{\sqrt{2}}(\sin\phi, -\cos\phi, 0) \tag{59}$$

and

$$\epsilon_{\perp 2} = \frac{1}{\sqrt{2}}(\cos\theta\cos\phi, \cos\theta\sin\phi, -\sin\theta), \tag{60}$$

so that

$$|\epsilon_{\perp 1}|^2 + |\epsilon_{\perp 2}|^2 = 1.$$

Following Collins, we note that the electric field of the incoming wave will cause the atom to oscillate, and this motion coupled with the magnetic field will cause a secondary oscillation. Thus, the atom may be considered to have a dipole moment consisting of two parts,

$$\mathbf{D} = \mathbf{D}_{\mathrm{E}} + \mathbf{D}_{\mathrm{M}}, \tag{61}$$

where

$$\mathbf{D}_{\mathrm{E}} \propto \mathbf{E} \tag{62}$$

and

$$\mathbf{D}_{\mathrm{M}} \propto \mathbf{E} \times \mathbf{x}, \tag{63}$$

where

$$\mathbf{x} = \frac{e\mathbf{B}}{m_N c}/\omega = \frac{\omega_c}{\omega}\hat{\mathbf{e}}_B, \tag{64}$$

and m_N is the mass of the nucleus. Since the gyrofrequency of the nucleus, ω_c, is only $\approx$ 6eV at $B = 10^{12}$G (and we will typically consider frequencies higher than that), we will expand only to first order in $x = |\mathbf{x}|$.

The new (unnormalized) components of polarization are

$$\hat{\mathbf{e}}_{\perp 1} = \frac{1}{\sqrt{2}}(\epsilon_{\perp 1} + x(\epsilon_{\perp 1} \times \hat{\mathbf{e}}_B)) \tag{65}$$

and

$$\hat{\mathbf{e}}_{\perp 2} = \frac{1}{\sqrt{2}}(\epsilon_{\perp 2} + x(\epsilon_{\perp 2} \times \hat{\mathbf{e}}_B)). \tag{66}$$

The normalization for both of these is roughly $\frac{1}{\sqrt{1+x^2}}$, which we will approximate as 1.

To get the polarization coefficients, we note that, e.g.,

$$\gamma_B = \int_0^{2\pi} \int_0^{\pi} (|\hat{\mathbf{e}}_B \cdot \hat{\mathbf{e}}_{\perp 1}|^2 + |\hat{\mathbf{e}}_B \cdot \hat{\mathbf{e}}_{\perp 2}|^2) w(\theta, \phi, \psi) \sin\theta d\theta d\phi / N, \tag{67}$$

where N is the normalization factor and $w(\theta, \phi, \psi)$ is a weight factor (such as $w(\theta, \phi, \psi) = 1 + \cos^2\theta$ for Thomson scattering). To check the validity of these assumptions, we will first calculate the polarization coefficients for the isotropic case, $w(\theta, \phi, \psi) = 1$.

$$\gamma_B = \frac{1}{2} \int_0^{2\pi} \int_0^{\pi} (\cos^2\phi \sin^2\psi + \cos^2\theta \sin^2\phi \sin^2\psi + \sin^2\theta \cos^2\psi$$
$$-2\sin\theta\cos\theta\sin\phi\sin\psi\cos\psi) \sin\theta d\theta d\phi / 4\pi$$
$$= \frac{1}{3} + \mathcal{O}(x^2) \tag{68}$$

$$\gamma_+ = \frac{1}{4} \int_0^{2\pi} \int_0^{\pi} (\sin^2\phi + \cos^2\phi\cos^2\psi + \cos^2\theta\cos^2\phi + \cos^2\theta\sin^2\phi\cos^2\psi +$$
$$\sin^2\theta\sin^2\psi + 2\sin\theta\cos\theta\sin\phi\sin\psi\cos\psi + O(x)) \sin\theta d\theta d\phi / 4\pi$$
$$= \frac{1}{3} + \mathcal{O}(x^2) \tag{69}$$

$$\gamma_+ = \gamma_-, \tag{70}$$

so the coefficients are all equal, as they should be. Note that the terms of order x integrate to 0.

As indicated in the previous section, for bound-free absorption the cross section that is due to B polarization is much greater than that due to circular polarization. This is the case we will consider, but we note in passing that for bound-bound absorption this assumption is decidedly incorrect, since transition rules may forbid absorption that is due to B polarization at certain frequencies. Thus, in a treatment of radiative transfer that includes energies less than the binding energy of the atom, the full formula for polarization coefficients given below with $r > 0$ must be used.

The differential cross section for unpolarized light may be determined by adding the differential cross sections that are due to the two polarization components (see e.g. Rybicki and Lightman pg. 90 and following):

$$\begin{aligned}\frac{d\sigma}{d\Omega} \propto (1-\hat{e}_{\perp 1,z}^2)[(\hat{\mathbf{e}}_{\perp 1}\cdot\hat{\mathbf{e}}_B)^2 + r(1-(\hat{\mathbf{e}}_{\perp 1}\cdot\hat{\mathbf{e}}_B)^2)] \\ + (1-\hat{e}_{\perp 2,z}^2)[(\hat{\mathbf{e}}_{\perp 2}\cdot\hat{\mathbf{e}}_B)^2 + r(1-(\hat{\mathbf{e}}_{\perp 2}\cdot\hat{\mathbf{e}}_B)^2)]\end{aligned}, \tag{71}$$

where $r \equiv \frac{\sigma_+}{\sigma_B}$ and $\hat{e}_{\perp 1,z}$ is the z-component of the first polarization vector. For an isotropic cross section, $r = 1$, while for our case, $r \ll 1$. The weight function is

$$w(\theta,\phi,\psi) \propto \frac{d\sigma}{d\Omega}, \tag{72}$$

and the normalization factor is

$$N = \int_0^{2\pi}\int_0^{\pi} w(\theta,\phi,\psi)\sin\theta d\theta d\phi = \frac{\pi}{15}(36(1-r)\sin^2\psi + 8(1-r)\cos^2\psi + 80r). \tag{73}$$

The coefficients become

$$\begin{aligned}\gamma_B = \frac{1}{2}\int_0^{2\pi}\int_0^{\pi}[\cos^2\phi\sin^2\psi + \cos^2\theta\sin^2\phi\sin^2\psi + \sin^2\theta\cos^2\psi \\ -2\sin\theta\cos\theta\sin\phi\sin\psi\cos\psi]w(\theta,\phi,\psi)\sin\theta d\theta d\phi/N \\ = \frac{\frac{4}{7}(1-r)+\frac{22}{7}(1-r)\sin^2\psi + r(6+\sin^2\psi)}{2(1-r)+7(1-r)\sin^2\psi+20r} + O(x^2),\end{aligned} \tag{74}$$

$$\gamma_+ = \gamma_- = \frac{1}{2}(1-\gamma_B). \tag{75}$$

Notice that, miraculously, x only shows up in terms of order x^2 or higher.

For example, for $\psi = 0$ and $r = 0$, this gives

$$\gamma_B = \frac{2}{7}, \gamma_+ = \gamma_- = \frac{5}{14}, \tag{76}$$

and for $\psi = \pi/2$ and $r = 0$,

$$\gamma_B = \frac{26}{63}, \gamma_+ = \gamma_- = \frac{37}{126}. \tag{77}$$

The average value for γ_B over the surface of a neutron star with a dipolar field and a rotation axis aligned with the magnetic axis is about 0.40. The total bound-free cross section has the form

$$\sigma_{\rm bf} \sim \gamma_+\sigma_+ + \gamma_-\sigma_- + \gamma_z\sigma_z, \tag{78}$$

so the cross sections are on average about 20% greater than in the isotropic case.

Appendix II. Projected area of the surface elements of the star

In order to calculate the thermal spectrum of a neutron star properly, we need to figure out how much of the projected surface area of the star has a magnetic field strength in a range dB around B, calculate the spectrum from that area, and integrate over the star. In this appendix, we use Newtonian straight-line optics. For a real neutron star, general relativity would have to be used, which would increase the apparent area of the star. We work with coordinates set up so that the z-axis is lined up with the magnetic axis and the line of sight is defined to be in the x-z plane. The projected area of a surface element at a direction (θ, ϕ) is its real area times the dot product of its normal vector with the vector of the line of sight. Let

$$\hat{r} = (\sin\theta\cos\phi, \sin\theta\sin\phi, \cos\theta) \tag{79}$$

be the normal vector of the surface element, and

$$\hat{q} = (\sin\psi, 0, \cos\psi) \tag{80}$$

be the vector of the line of sight, where ψ is the angle between the magnetic axis and the line of sight. Then the contribution from the surface element is

$$\hat{r}\cdot\hat{q} = \sin\theta\cos\phi\sin\psi + cos\theta\cos\psi. \tag{81}$$

To determine the projected area of the surface with a given magnetic field, we first need to determine how much is visible, since the star will block out its own back side. For a given ψ and θ the range of observable ϕ's is determined by the solutions to $\hat{r} \cdot \hat{q} = 0$:

$$\cos\phi = -\frac{\cos\theta\cos\psi}{\sin\theta\sin\psi}, \tag{82}$$

so ϕ runs from $-\phi_1$ to ϕ_1, where

$$\phi_1 = \cos^{-1}\left[-\frac{\cos\theta\cos\psi}{\sin\theta\sin\psi}\right]. \tag{83}$$

When the expression in brackets is less than -1, the allowed angles run from $-\pi$ to π, wheras when the expression is greater than +1, there are no allowed angles. For a dipolar field, the magnetic field strength is given by

$$|B| = B_{\rm eq}\sqrt{1+3\cos^2\theta}, \tag{84}$$

where $B_{\rm eq}$ is the equatorial field. Thus, if the field varies in strength from B_1 to B_2, the angle varies from

$$\theta_1 = \cos^{-1}\sqrt{\frac{1}{3}\left(\frac{B_1}{B_{\rm eq}}\right)^2 - 1)} \tag{85}$$

to

$$\theta_2 = \cos^{-1}\sqrt{\frac{1}{3}\left(\frac{B_2}{B_{\rm eq}}\right)^2 - 1)}. \tag{86}$$

The band from $\pi-\theta_1$ to $\pi-\theta_2$ also encompasses these fields, so the total projected area is

$$\begin{aligned} A(B_1,B_2) = &\int_{\theta_1}^{\theta_2}\int_{-\phi_1}^{\phi_1}(\sin\theta\cos\phi\sin\psi+\cos\theta\cos\psi)\sin\theta d\phi d\theta \\ &+\int_{\pi-\theta_2}^{\pi-\theta_1}\int_{\phi_1-\pi}^{\pi-\phi_1}(\sin\theta\cos\phi\sin\psi+\cos\theta\cos\psi)\sin\theta d\phi d\theta. \end{aligned} \tag{87}$$

If θ_1 and θ_2 are close together, we may approximate this double integral by setting $\theta = (\theta_1 + \theta_2)/2$, so that

$$A(B_1, B_2) \approx (\theta_2 - \theta_1) \sin\theta \Big[\int_{-\phi_1}^{\phi_1} (\sin\theta \cos\phi \sin\psi + \cos\theta \cos\psi) d\phi + \int_{\phi_1 - \pi}^{\pi - \phi_1} (\sin\theta \cos\phi \sin\psi - \cos\theta \cos\psi) d\phi) \Big], \tag{88}$$

where the minus sign in the second integral is because $\cos(\pi - \theta) = -\cos(\theta)$. In our simulations we use ten intermediate fields to approximate the surface, though there was almost no difference between using ten and five.

References

Abramowitz, M., and Stegun, I. A. 1972, *Handbook of Mathematical Functions* (New York:Dover).

Alcock, C., and Illarionov, A. 1980, *Ap. J.*, **235**, 534.

Cordova, F., Hjellming, R. M., Mason, K. O., and Middleditch, J. 1989 *Ap. J.* submitted.

Forster, H., Strupat, W., Rösner, W., Wunner, G., Ruder, H., and Herold, H. 1984, *J. Phys. B: At. Mol. Phys.*, **17**, 1301.

Helfand, D. J. 1983, *Supernova Remnants and Their X-ray Emission*, eds. J. Danziger and P. Gorenstein (Dordrecht: Reidel), p. 471.

Kara, S. M., and McDowell M. R. C. 1980, *J. Phys. B: At. Mol. Phys.*, **13**, 1337.

Khersonskij, V. K., 1987, *Astron. Zh.*, **64**, 433.

Mihalas, D. 1978, *Stellar Atmospheres* (San Francisco:Freeman).

Miller, M. C., and Neuhauser, D. 1990, California Institute of Technology, preprint.

Murakami, T., Fujii, M., Hayashida, K., Itoh, M., Nishimura, J., Yamagami, T., Conner, J. P., Evans, W. D., Fenimore, E. E., Klebesadel, R. W., Yoshida, A., Kondo, I., and Kawai, N. 1988 *Nature*, **335**, 234.

O'Connel, R. F. 1979, *Phys. Lett.*, **70A**, 389.

Romani, R. W. 1987, *Ap. J.*, **313**, 718.

Rösner, W., Herold, H., Ruder, H., and Wunner, G. 1983, *Phys. Rev. A*, **28**, 2071.

Rösner, W., Wunner, G., Herold, H., and Ruder, H. 1984, *J. Phys. B: At. Mol. Phys.*, **17**, 29.

Ruder, H., Herold, H., Rösner, W., and Wunner, G. 1985, *Physica B&C*, **127**, 11.

Simola, J., and Virtamo J. 1978, *J. Phys. B: At. Mol. Phys.*, **11**, 3309.

Tsuruta, S. 1986 *Comments Ap.*, **11**, 151.

Tuohy, I., and Garmire, G. 1980, *Ap. J. (Letters)*, **239**, L107.

Wunner, G. 1986, *J. Phys. B: At. Mol. Phys.*, **19**, 1623.

Wunner, G., and Ruder, H. 1987, *Phys. Scr.*, **36**, 291.

Wunner, G., Ruder, H., and Herold, H. 1980, *J. Phys. B: At. Mol. Phys.*, **14**, 765.

Table caption

Table 1: We list the blackbody temperatures associated with the various magnetic field values and surface compositions of the model atmospheres. In this table, $T_{\rm E}$ is defined as the temperature of the blackbody curve which gives the same number of counts in the sensitivity range of the *Einstein* IPC (0.5 to 5.0 keV) as the spectrum does, while $T_{\rm R}$ is defined similarly for the *ROSAT* HRI (0.1 to 2.0 keV).

Figure captions

Figure 1: We compare the pressures given by: an ideal gas; electron degeneracy at a magnetic field $B = 0$; and electron degeneracy at a magnetic field $B = 10^{12}$G, as a function of electron density n_e.

Figures 2: We show the fraction of neutral atoms at a density of $\rho = 1\text{g/cm}^3$ for hydrogen, helium, carbon and nitrogen at a variety of temperatures and magnetic fields. The ionization fraction at $B = 0$ is included for comparison.

Figure 3: We compare the unredshifted spectra of helium at surface gravities of 10^{14} and 10^{15}cm/s^2 for $B = 4.7 \times 10^{12}$G and $T = 3.0 \times 10^5$K. This figure demonstrates that the surface gravity does not have a significant effect on the unredshifted spectrum, and as a result we have set $g = 3 \times 10^{14}\text{cm/s}^2$ in the calculations listed in Table 1.

Figure 4: We graph the ratio of the unredshifted spectrum of hydrogen to the spectrum of a blackbody at $T_{\text{eff}} = 1.0 \times 10^6$K and $B = 9.4 \times 10^{11}$G, 2.35×10^{12}G and 4.7×10^{12}G.

Figure 5: We graph the ratio of the unredshifted spectrum of helium to the spectrum of a blackbody at $T_{\text{eff}} = 1.0 \times 10^6$K and $B = 9.4 \times 10^{11}$G, 2.35×10^{12}G and 4.7×10^{12}G.

Figure 6: We graph the ratio of the unredshifted spectrum of carbon to the spectrum of a blackbody at $T_{\text{eff}} = 1.0 \times 10^6$K and $B = 9.4 \times 10^{11}$G, 2.35×10^{12}G and 4.7×10^{12}G.

Figure 7: We graph the ratio of the unredshifted spectrum of nitrogen to the spectrum of a blackbody at $T_{\text{eff}} = 1.0 \times 10^6$K and $B = 9.4 \times 10^{11}$G, 2.35×10^{12}G and 4.7×10^{12}G.

Figure 8: We graph temperature vs. Rosseland optical depth for hydrogen at an effective temperature of $T_{\text{eff}} = 10^6$K at equatorial magnetic field strengths of $B = 9.4 \times 10^{11}$G, $B = 2.35 \times 10^{12}$G and $B = 4.7 \times 10^{12}$G.

Figure 9: We graph temperature vs. Rosseland optical depth for helium at an effective temperature of $T_{\text{eff}} = 10^6$K at equatorial magnetic field strengths of $B = 9.4 \times 10^{11}$G, $B = 2.35 \times 10^{12}$G and $B = 4.7 \times 10^{12}$G.

Figure 10: We graph temperature vs. Rosseland optical depth for carbon at an effective temperature of $T_{\text{eff}} = 10^6$K at equatorial magnetic field strengths of $B = 9.4 \times 10^{11}$G, $B = 2.35 \times 10^{12}$G and $B = 4.7 \times 10^{12}$G.

Figure 11: We graph temperature vs. Rosseland optical depth for nitrogen at an effective temperature of $T_{\text{eff}} = 10^6$K at equatorial magnetic field strengths of $B = 9.4 \times 10^{11}$G, $B = 2.35 \times 10^{12}$G and $B = 4.7 \times 10^{12}$G.

Figures 12: We graph pressure vs. Rosseland optical depth for hydrogen at an effective temperature of $T_{\text{eff}} = 10^6$K, at equatorial magnetic field strengths of $B = 9.4 \times 10^{11}$G, $B = 2.35 \times 10^{12}$G and $B = 4.7 \times 10^{12}$G.

Figures 13: We graph pressure vs. Rosseland optical depth for helium at an effective temperature of $T_{\text{eff}} = 10^6$K, at equatorial magnetic field strengths of $B = 9.4 \times 10^{11}$G, $B = 2.35 \times 10^{12}$G and $B = 4.7 \times 10^{12}$G.

Figures 14: We graph pressure vs. Rosseland optical depth for carbon at an effective temperature of $T_{\text{eff}} = 10^6$K, at equatorial magnetic field strengths of $B = 9.4 \times 10^{11}$G, $B = 2.35 \times 10^{12}$G and $B = 4.7 \times 10^{12}$G.

Figures 15: We graph pressure vs. Rosseland optical depth for nitrogen at an effective temperature of $T_{\text{eff}} = 10^6$K, at equatorial magnetic field strengths of $B = 9.4 \times 10^{11}$G, $B = 2.35 \times 10^{12}$G and $B = 4.7 \times 10^{12}$G.

TABLE 1
Temperatures of blackbodies giving the same count rates as model atmospheres

B(Gauss)	$T_{\rm eff}$(K)	Surface Composition	Einstein	Rosat
9.4×10^{11}	10^6	H	1.3×10^6	9.3×10^5
		He	8.7×10^6	1.1×10^6
		C	7.8×10^5	1.1×10^6
		N	7.8×10^5	1.1×10^6
2.35×10^{12}	10^6	H	1.3×10^6	1.0×10^5
		He	8.7×10^5	1.1×10^6
		C	7.1×10^5	1.1×10^6
		N	7.1×10^5	1.1×10^6
4.7×10^{12}	10^6	H	1.0×10^6	1.1×10^6
		He	8.3×10^5	1.1×10^6
		C	7.4×10^5	1.1×10^6
		N	7.6×10^5	1.1×10^6

Figure 1

Pressure vs. density for various eqns. of state

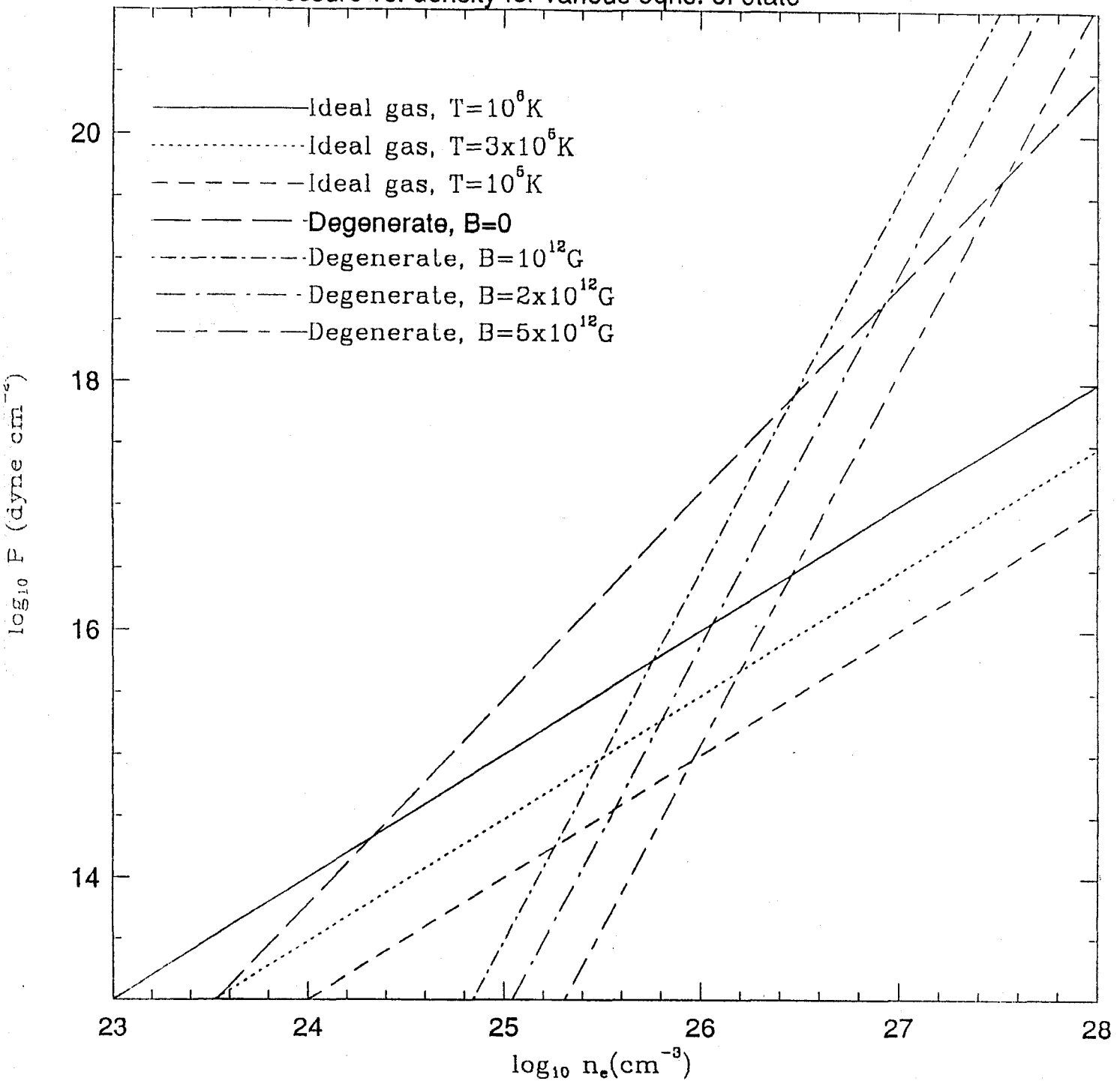

Figure 2a

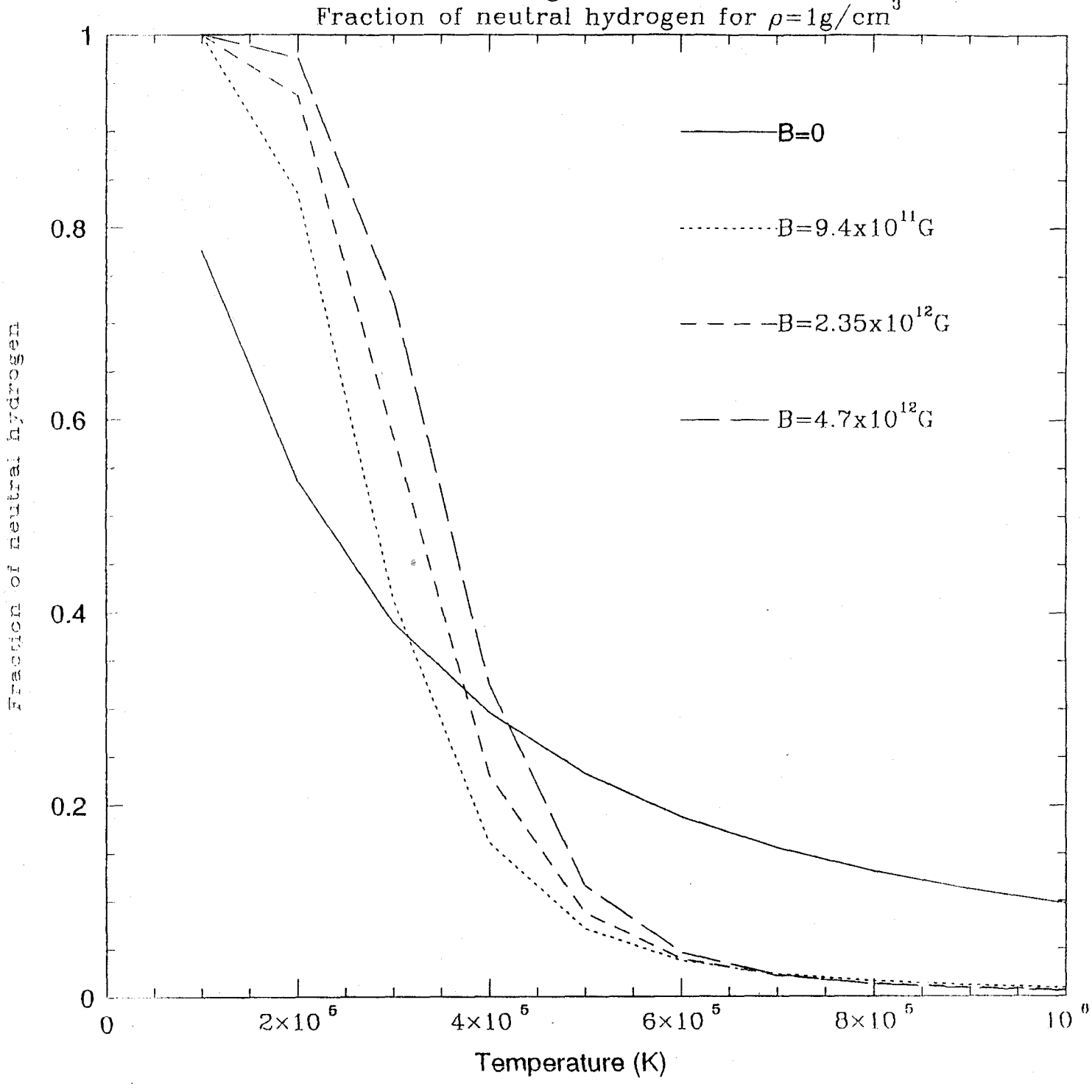
Fraction of neutral hydrogen for ρ=1g/cm^3
B=0
B=9.4x10^{11}G
B=2.35x10^{12}G
B=4.7x10^{12}G
Fraction of neutral hydrogen
Temperature (K)
0
0.2
0.4
0.6
0.8
1
2×10^5
4×10^5
6×10^5
8×10^5
10^6

Figure 2b

Fraction of neutral helium for ρ=1g/cm^3

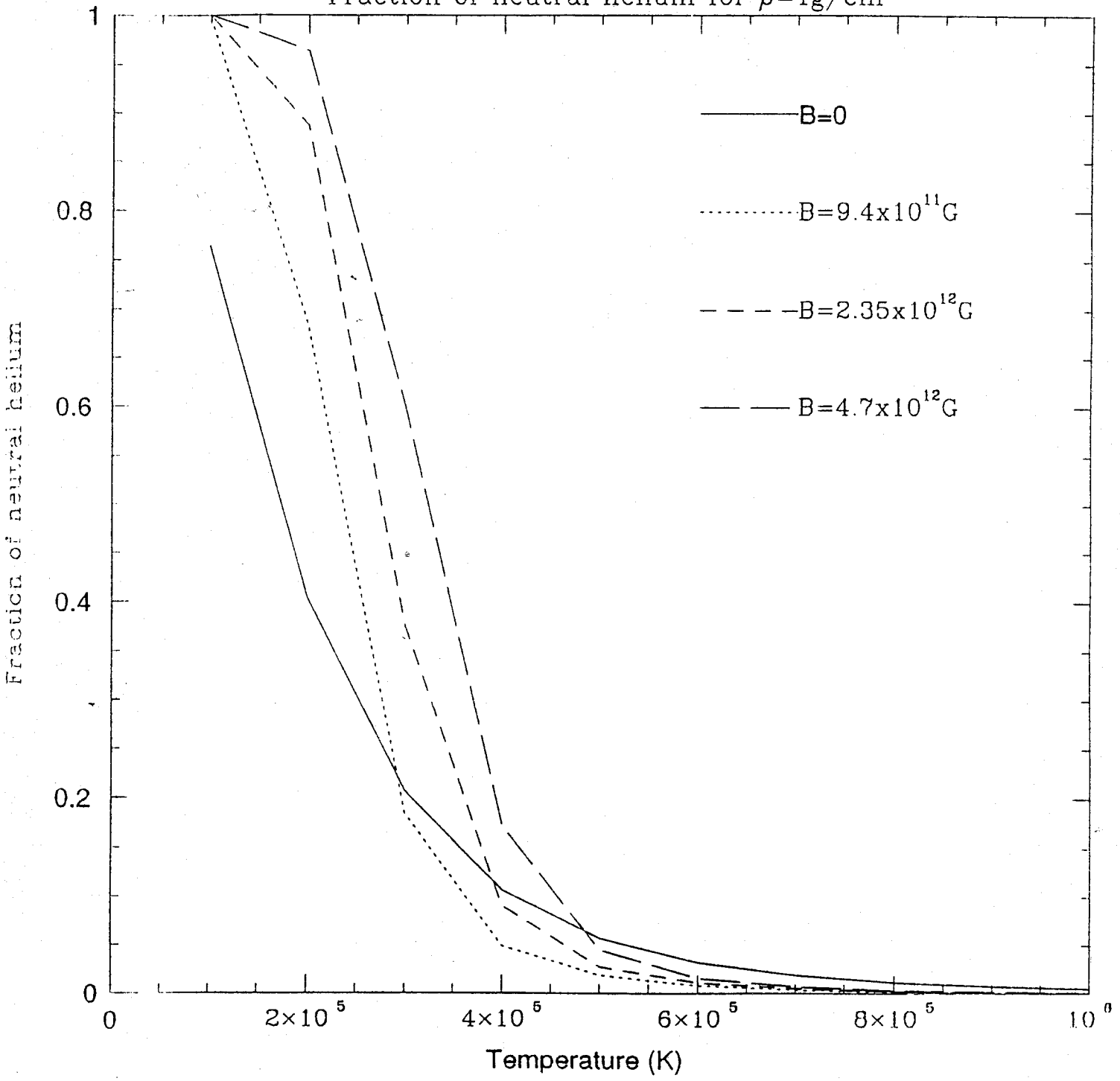

Figure 2d

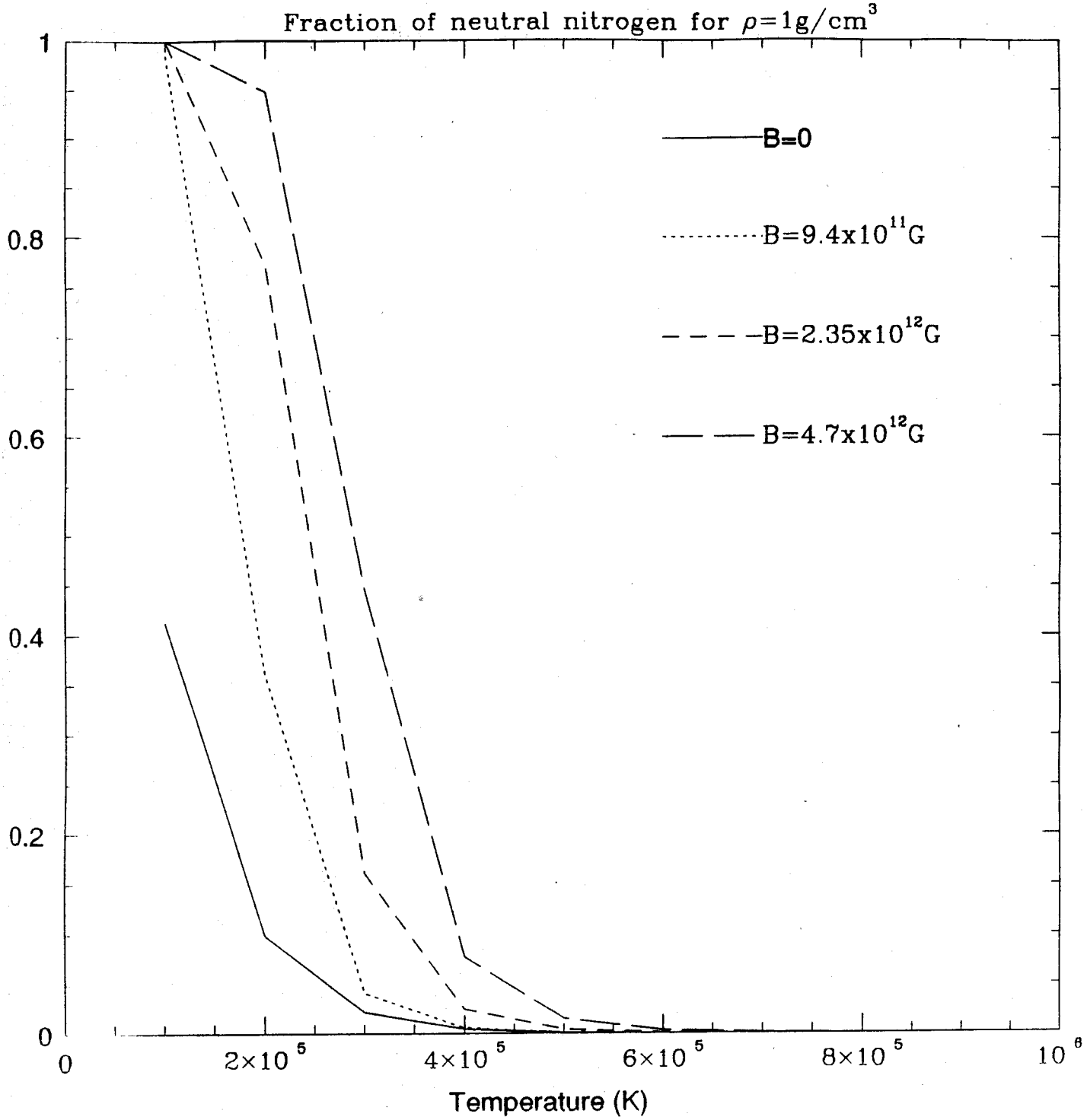
Fraction of neutral nitrogen for ρ=1g/cm^3
1
0.8
0.6
0.4
0.2
0
0
2×10^5
4×10^5
6×10^5
8×10^5
10^6
Temperature (K)
B=0
B=9.4x10^{11}G
B=2.35x10^{12}G
B=4.7x10^{12}G

Figure 3

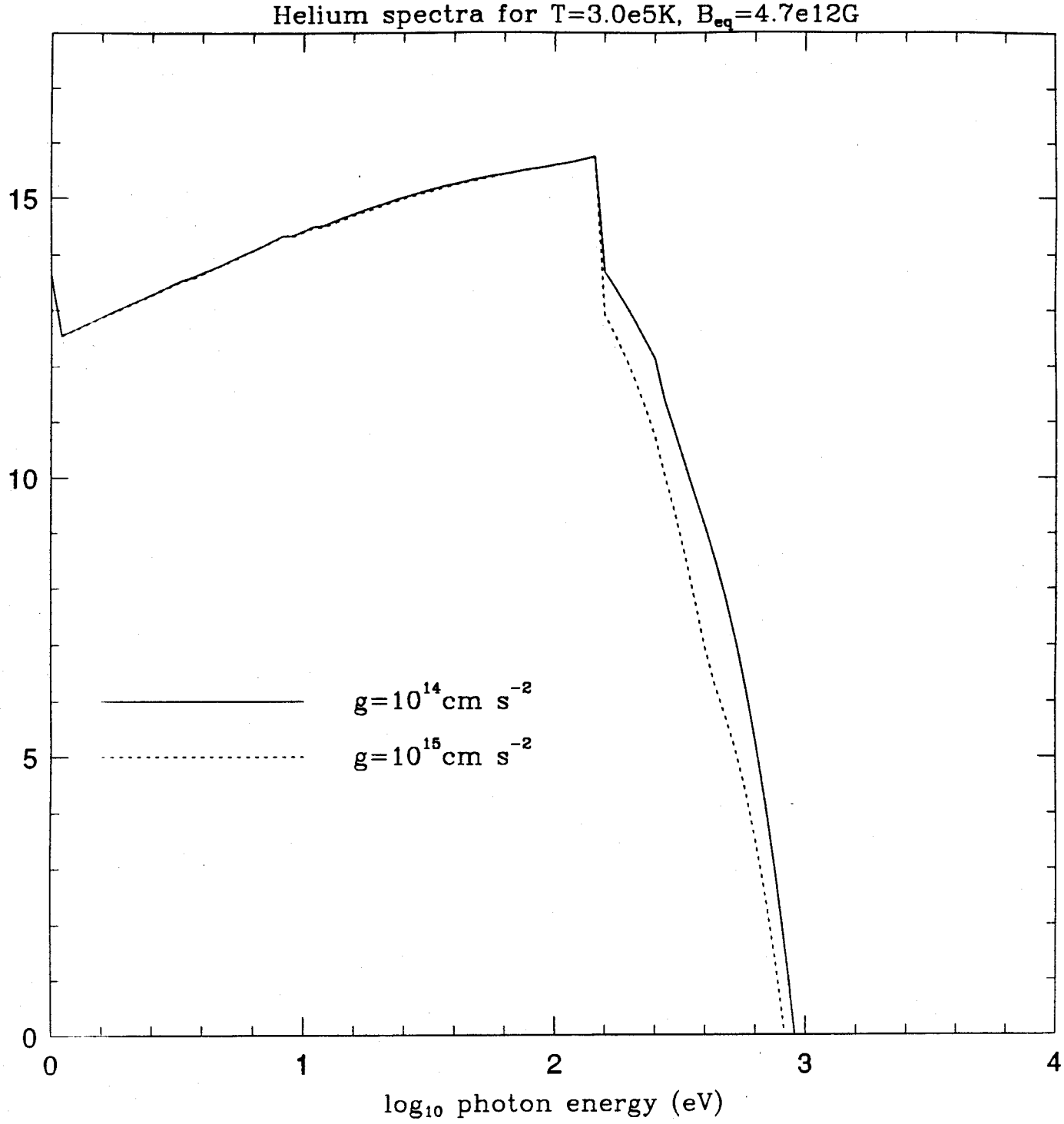
Helium spectra for T=3.0e5K, B_{eq}=4.7e12G
15
10
5
0
0
1
2
3
4
$g=10^{14}$cm s^{-2}
$g=10^{15}$cm s^{-2}
$\log_{10}$ photon energy (eV)

Figure 4

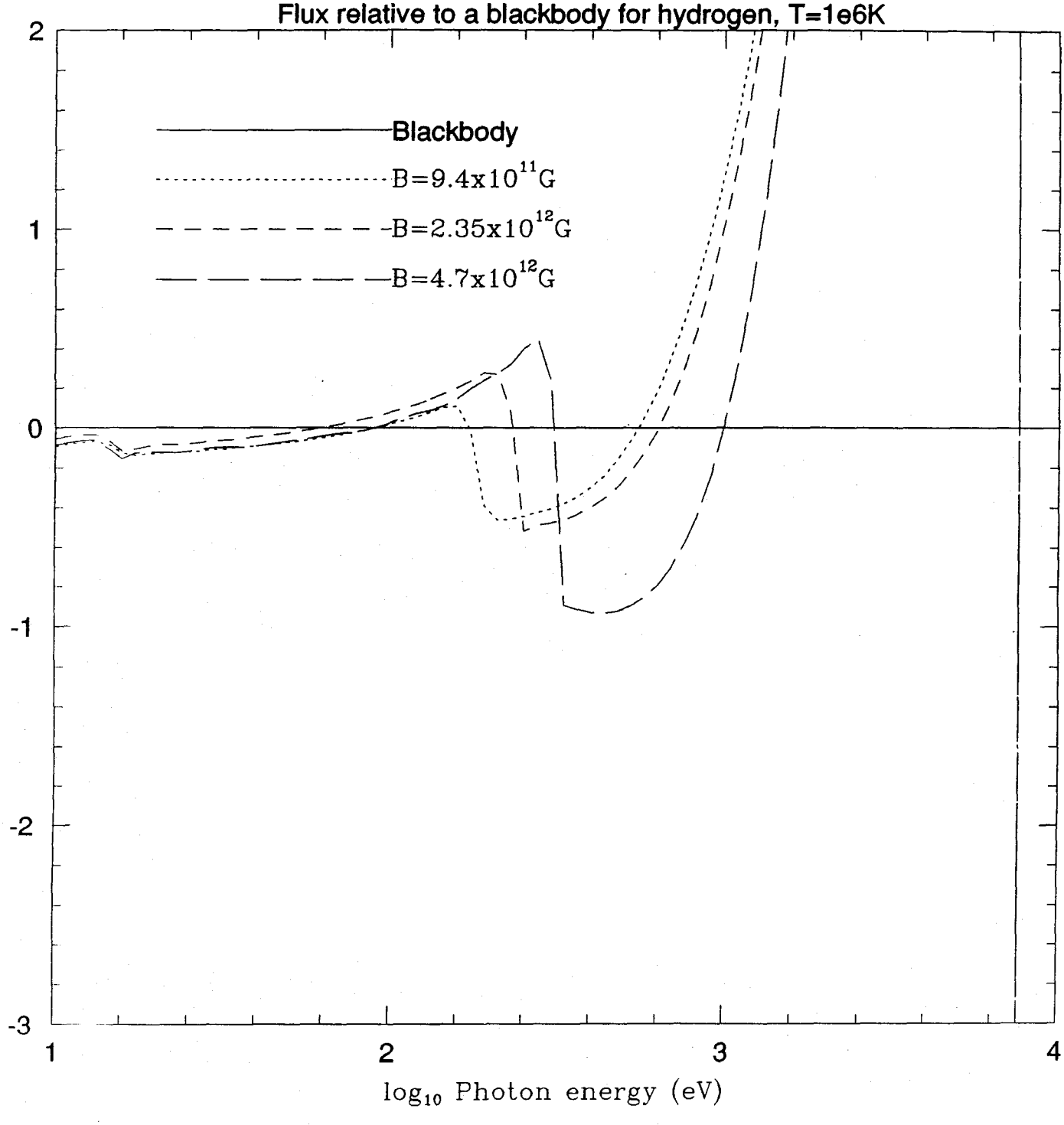
Flux relative to a blackbody for hydrogen, T=1e6K
Blackbody
B=9.4x10^11G
B=2.35x10^12G
B=4.7x10^12G
2
1
0
-1
-2
-3
1
2
3
4
log10 Photon energy (eV)

Figure 5

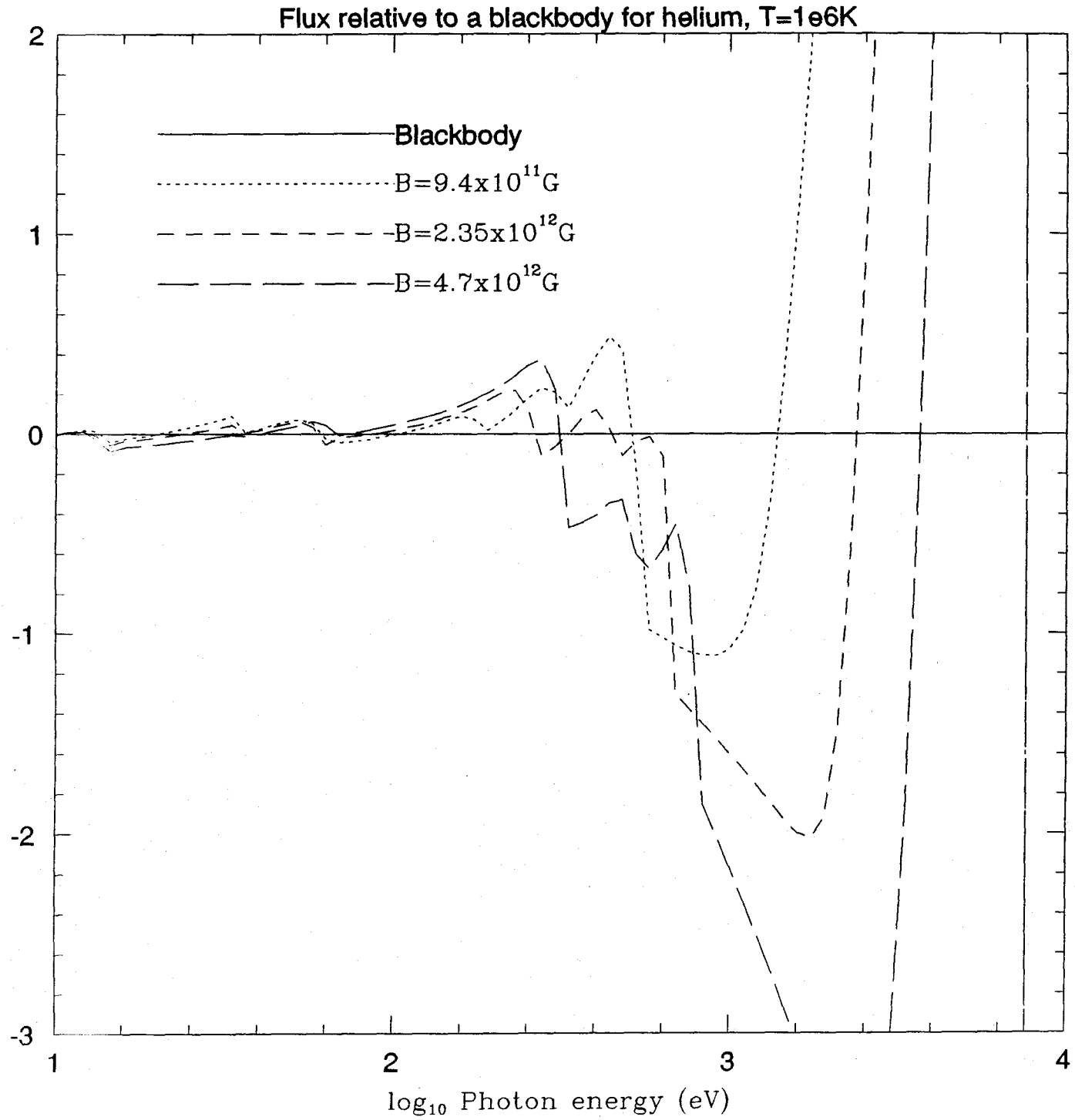
Flux relative to a blackbody for helium, T=1e6K
Blackbody
B=9.4x10^11G
B=2.35x10^12G
B=4.7x10^12G
2
1
0
-1
-2
-3
1
2
3
4
log10 Photon energy (eV)

Figure 6

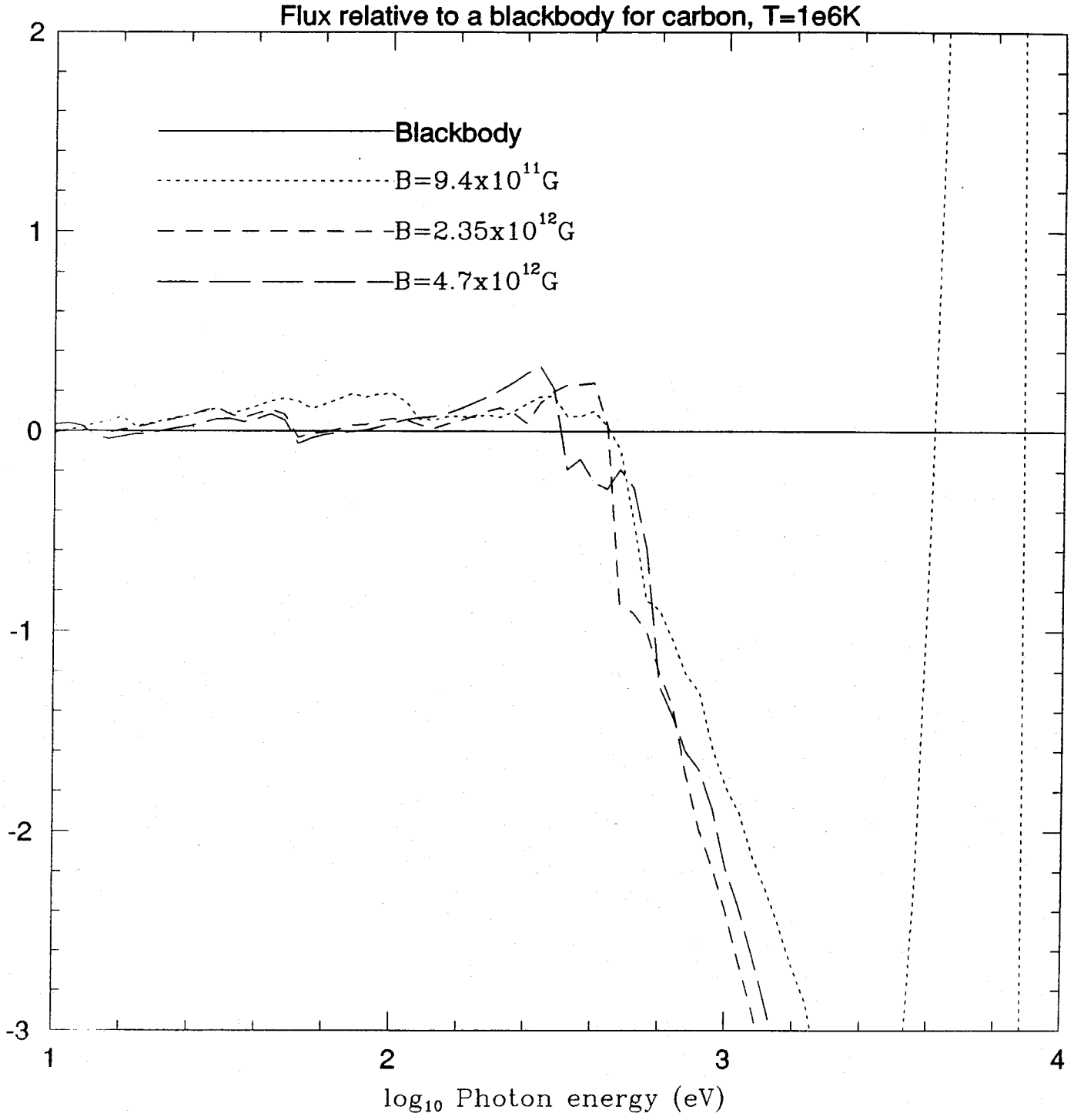
Flux relative to a blackbody for carbon, T=1e6K
Blackbody
B=9.4x10^11G
B=2.35x10^12G
B=4.7x10^12G
2
1
0
-1
-2
-3
1
2
3
4
log10 Photon energy (eV)

Figure 7

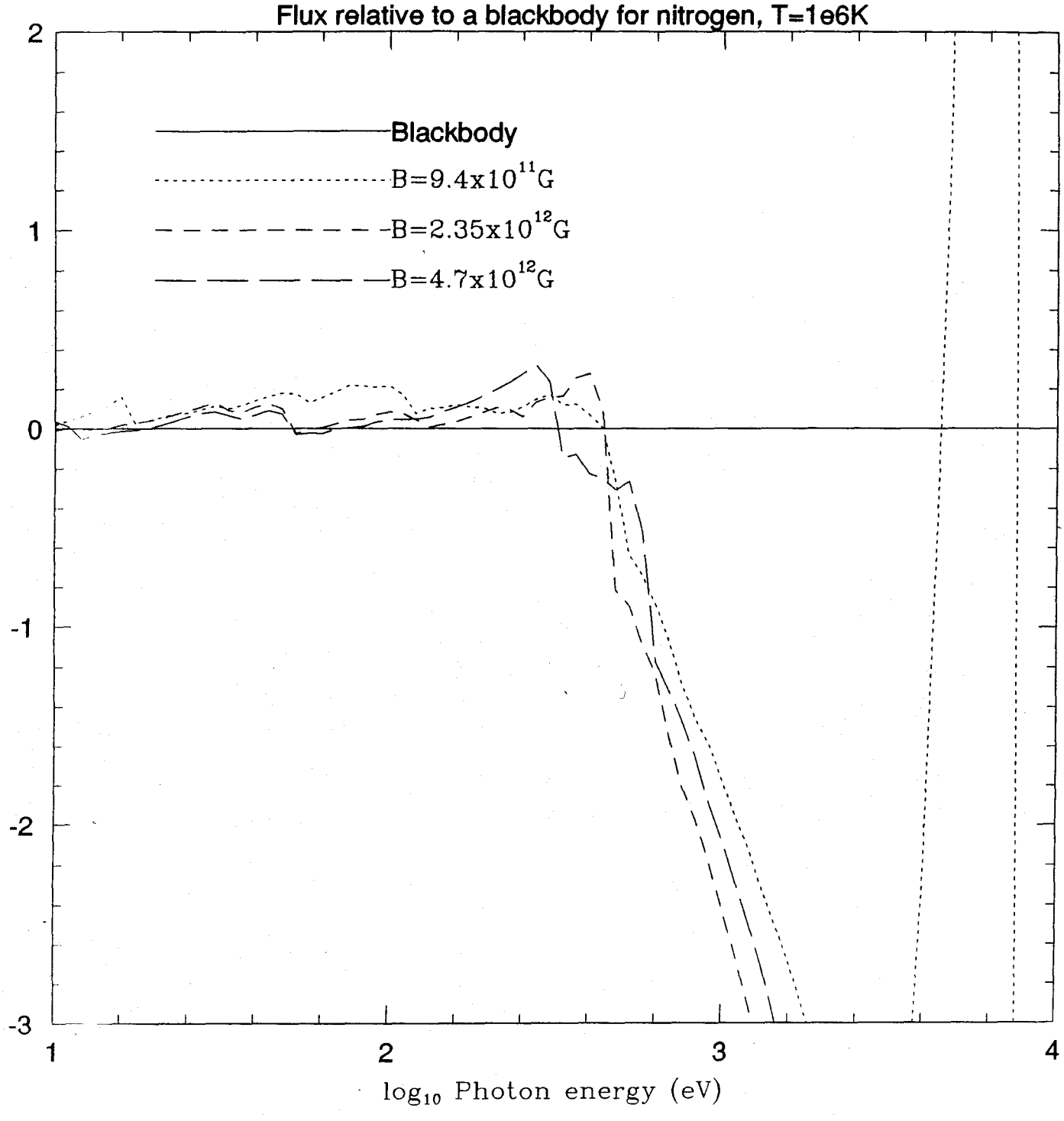
Flux relative to a blackbody for nitrogen, T=1e6K
Blackbody
B=9.4x10^11G
B=2.35x10^12G
B=4.7x10^12G
2
1
0
-1
-2
-3
1
2
3
4
log10 Photon energy (eV)

Figure 8

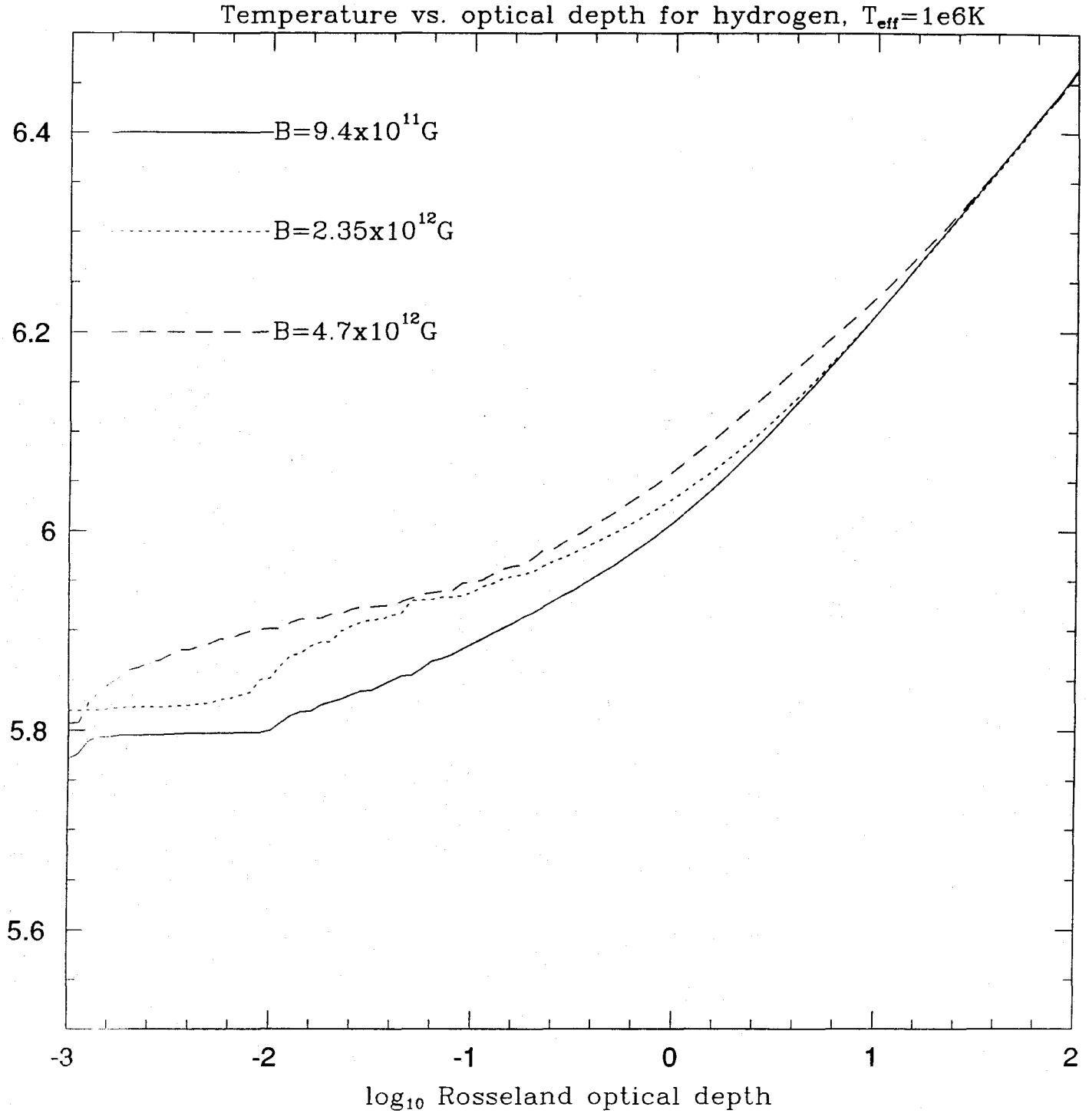
Temperature vs. optical depth for hydrogen, T_{eff}=1e6K
B=9.4x10^11G
B=2.35x10^12G
B=4.7x10^12G
6.4
6.2
6
5.8
5.6
-3
-2
-1
0
1
2
log10 Rosseland optical depth

Figure 9

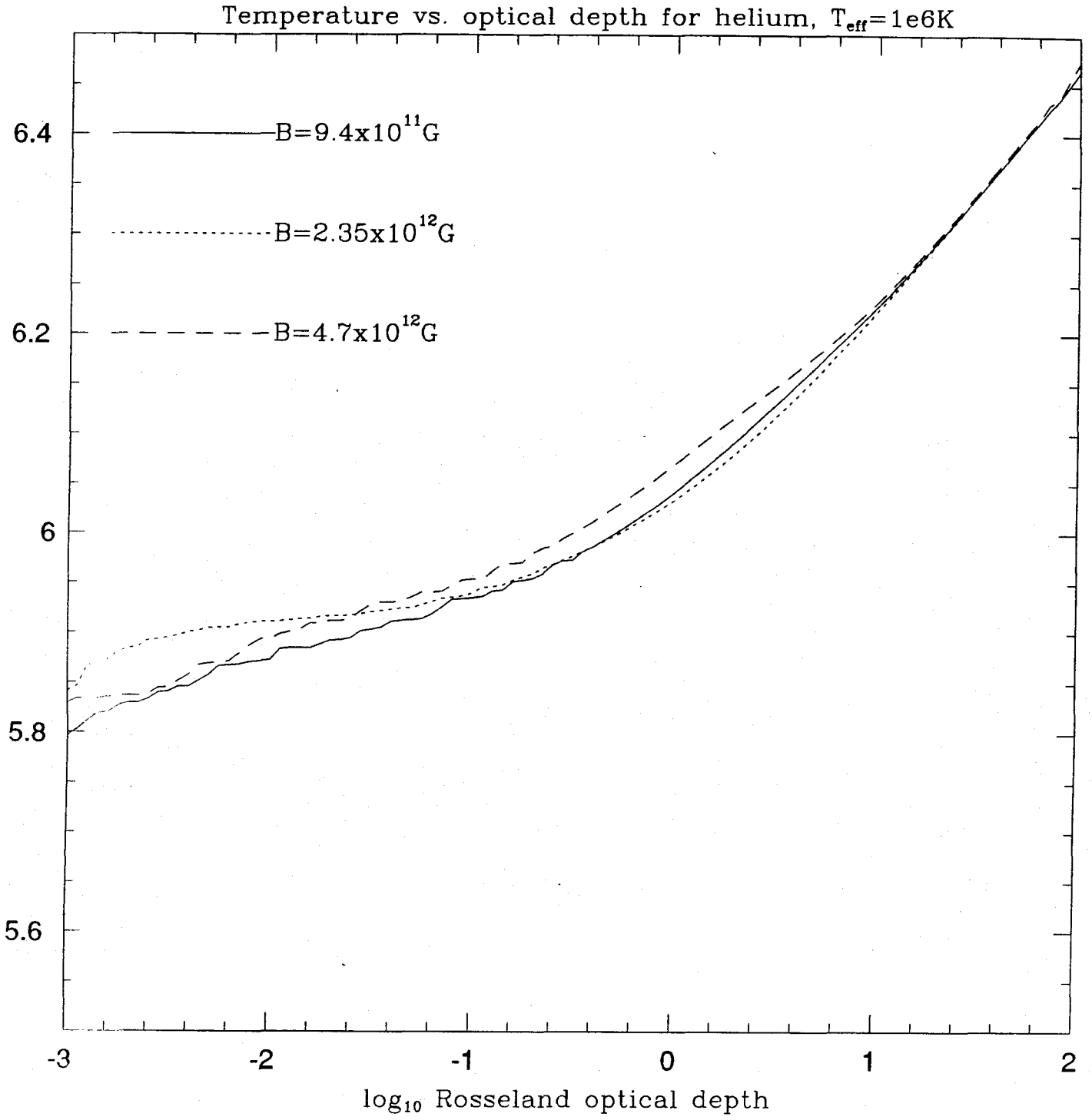
Temperature vs. optical depth for helium, T_{eff}=1e6K
B=9.4x10^11G
B=2.35x10^12G
B=4.7x10^12G
6.4
6.2
6
5.8
5.6
-3
-2
-1
0
1
2
log10 Rosseland optical depth

Figure 10

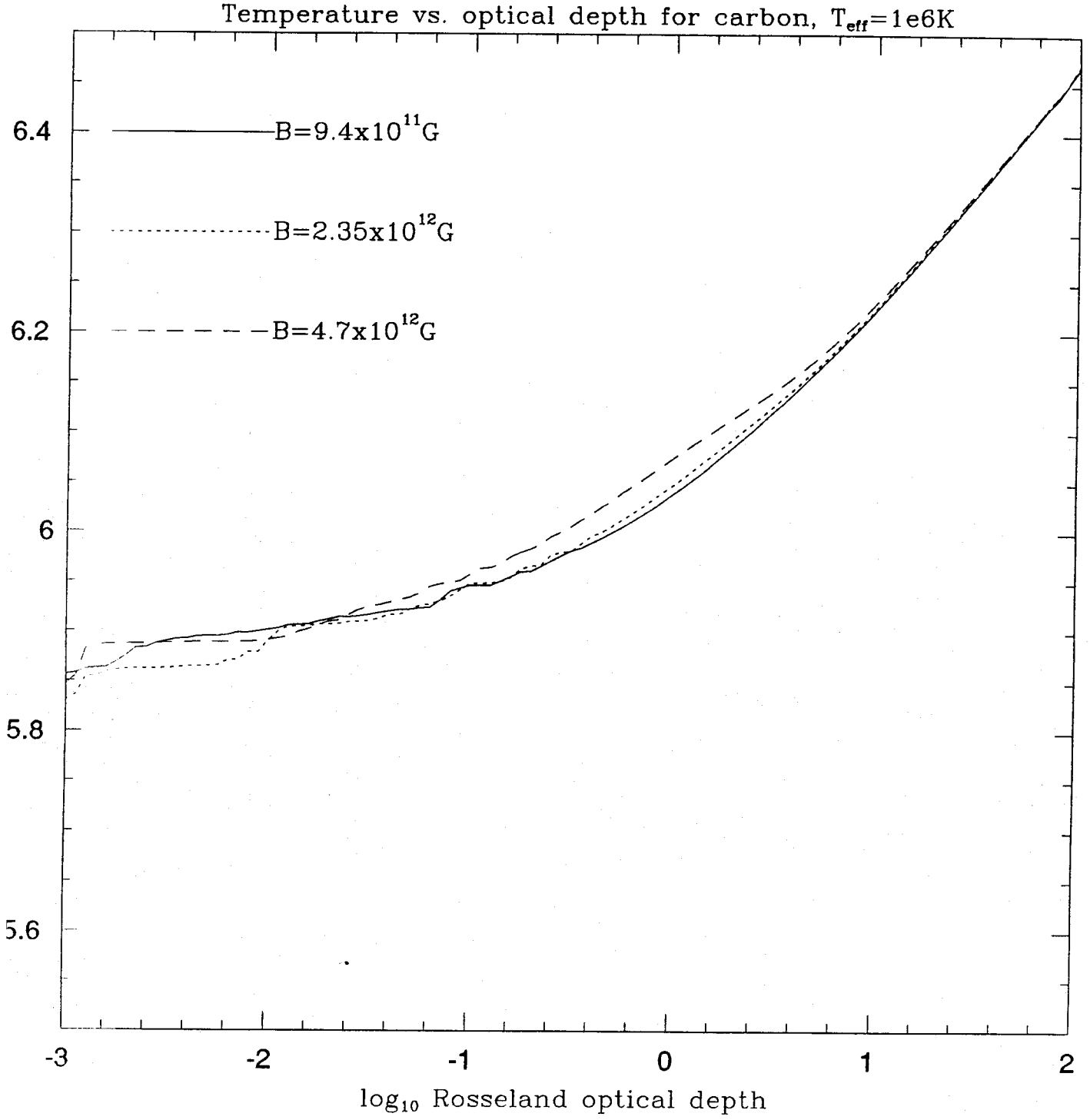
Temperature vs. optical depth for carbon, T_{eff}=1e6K
B=9.4x10^11G
B=2.35x10^12G
B=4.7x10^12G
6.4
6.2
6
5.8
5.6
-3
-2
-1
0
1
2
log10 Rosseland optical depth

Figure 11

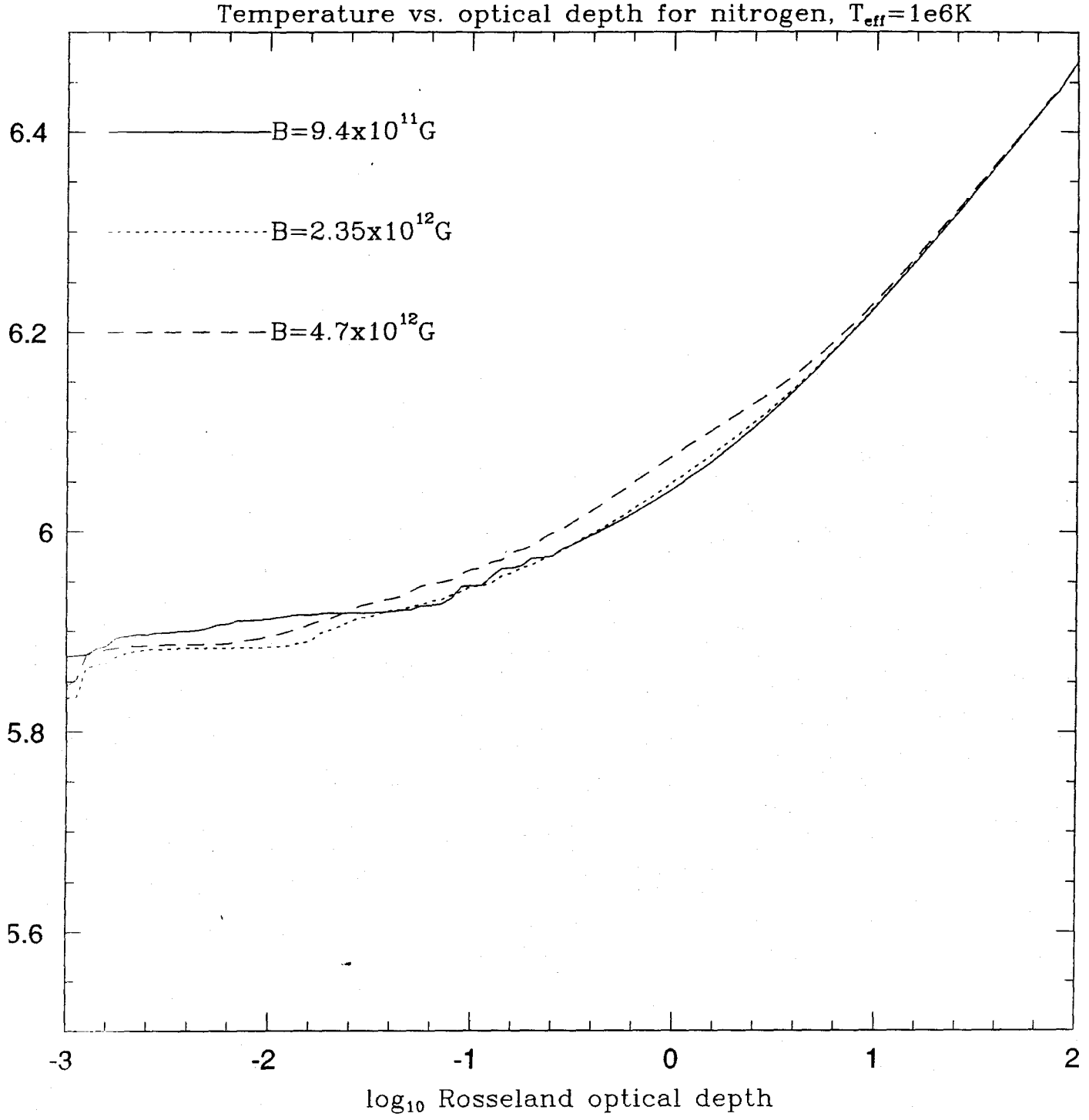
Temperature vs. optical depth for nitrogen, T_{eff}=1e6K
B=9.4x10^11G
B=2.35x10^12G
B=4.7x10^12G
6.4
6.2
6
5.8
5.6
-3
-2
-1
0
1
2
log10 Rosseland optical depth

Figure 12

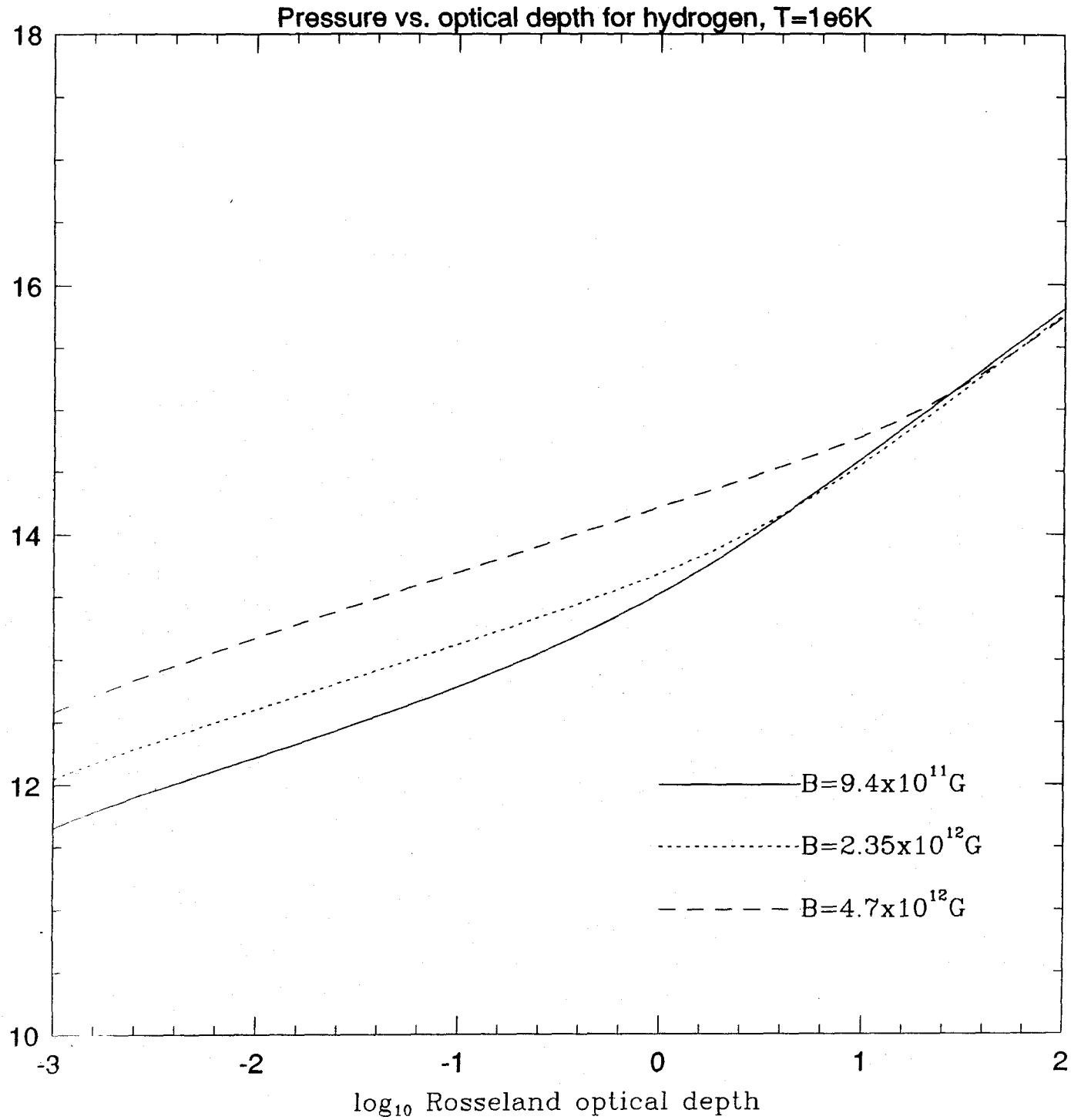
Pressure vs. optical depth for hydrogen, T=1e6K
18
16
14
12
10
-3
-2
-1
0
1
2
B=9.4x10^11G
B=2.35x10^12G
B=4.7x10^12G
log10 Rosseland optical depth

Figure 13

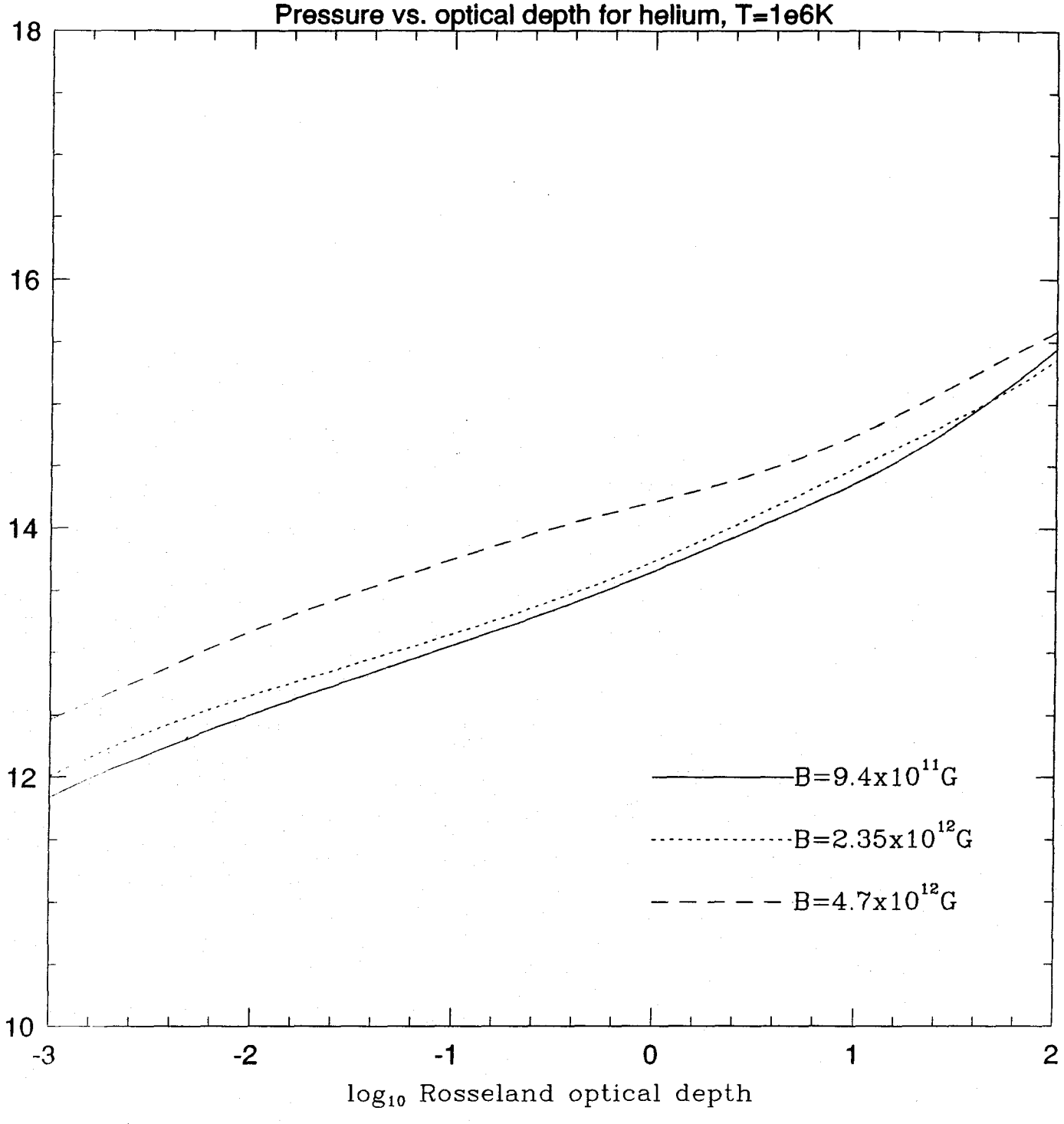
Pressure vs. optical depth for helium, T=1e6K
18
16
14
12
10
-3
-2
-1
0
1
2
B=9.4x10^11G
B=2.35x10^12G
B=4.7x10^12G
log10 Rosseland optical depth

Figure 14

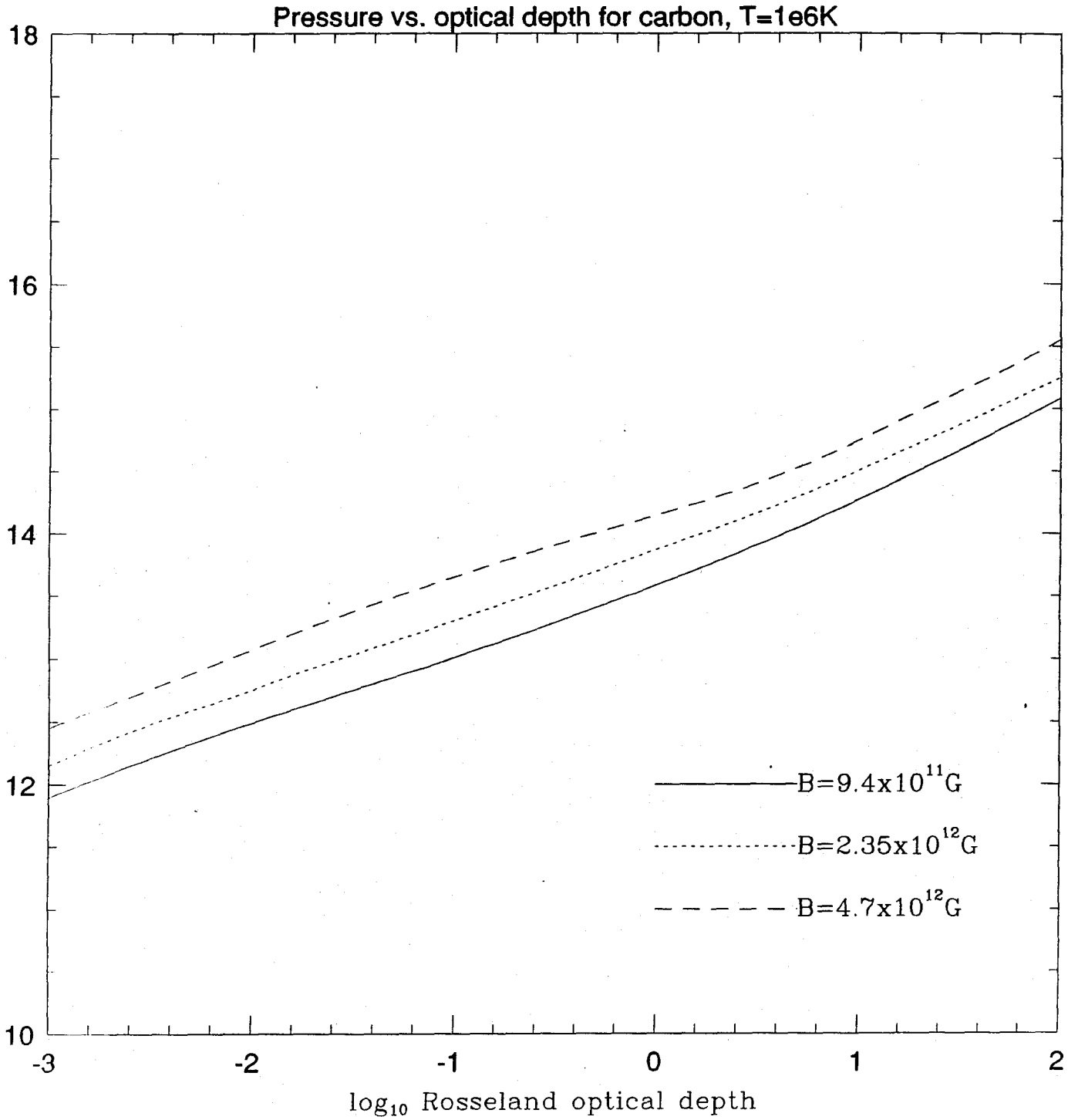
Pressure vs. optical depth for carbon, T=1e6K
18
16
14
12
10
-3
-2
-1
0
1
2
log10 Rosseland optical depth
B=9.4x10^11G
B=2.35x10^12G
B=4.7x10^12G

Figure 15

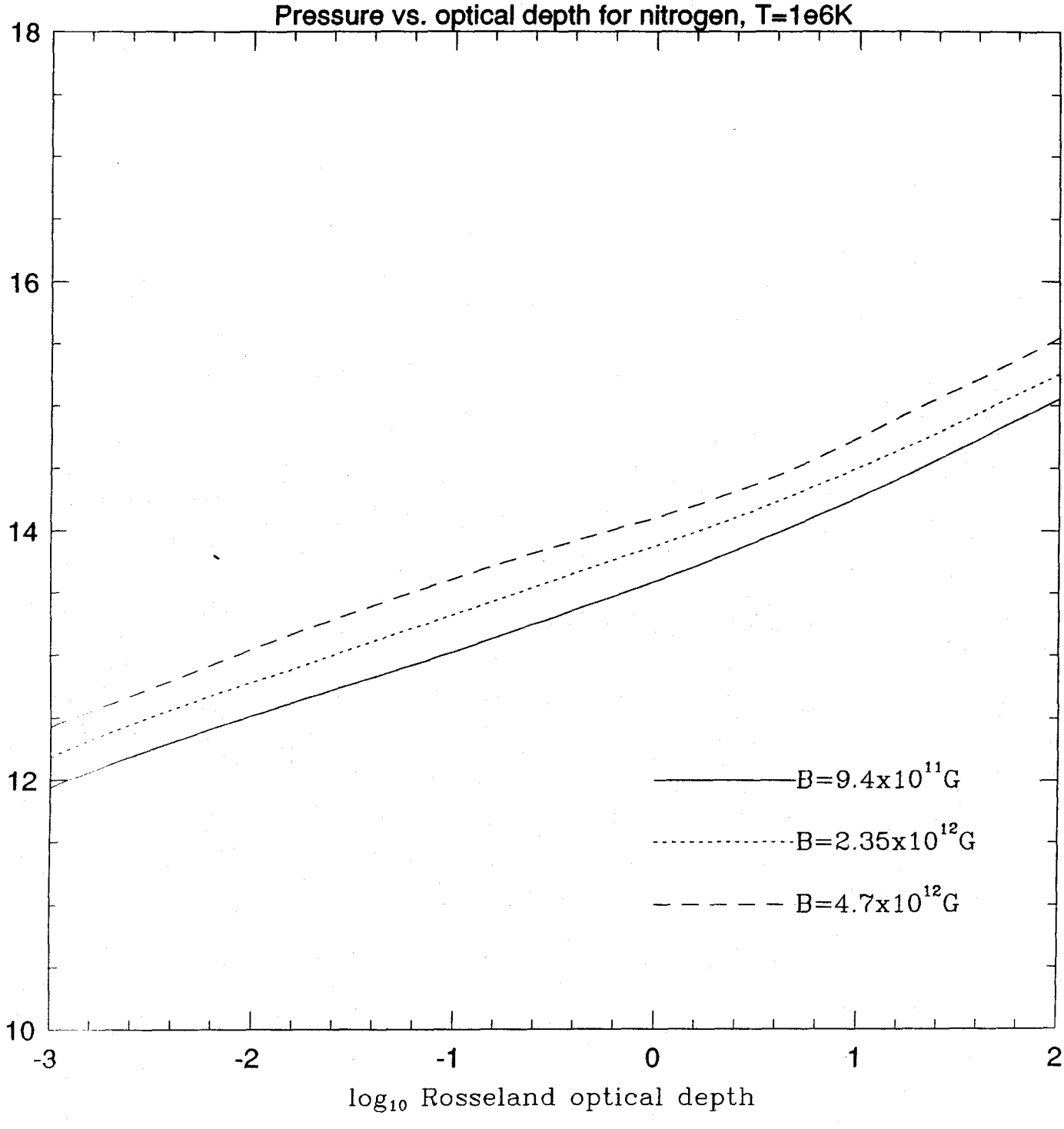
Pressure vs. optical depth for nitrogen, T=1e6K
18
16
14
12
10
-3
-2
-1
0
1
2
B=9.4x10^11G
B=2.35x10^12G
B=4.7x10^12G
log10 Rosseland optical depth

Chapter 4: Highly Ionized Atoms in Gamma-ray Bursts

M C Miller†

†Theoretical Astrophysics, California Institute of Technology, Pasadena, California 91125 USA

Classification number 3120D

Abstract. The X-ray spectra of gamma-ray bursts in the energy range 1keV-20keV may have identifiable lines from highly ionized elements, and the observation of these lines could help in the determination of the surface magnetic field, gravitational redshift and composition of neutron stars. This paper attempts to aid in the identification of such lines by calculating the energies of the ground state and one or two excited states of hydrogen and helium-like atoms in strong magnetic fields $B \geq 10^{12}$G. The energies are calculated with a high-field multiconfigurational Hartree-Fock code, as described in Miller and Neuhauser 1990. The hydrogen-like atoms are compared with previous results, and error estimates are made for the helium-like energies.

1. Introduction

Absorption features at a few tens of keV have been seen in some observations of gamma-ray bursts (Mazets et al. 1981,1982, Dennis et al. 1982, Hueter 1987). These features have usually been single, but recently the Ginga satellite observed two gamma-ray bursts with lines at about 19.5keV and 39keV (Murakami *et al.* 1988). Though it is somewhat suspicious that two events should produce the same profiles, the natural interpretation of these features, given a neutron star model of gamma-ray bursts, is that they are the fundamental and first harmonic of a cyclotron resonance. If this is true, it implies a surface magnetic field of $B > 10^{12}$G. However, it is difficult to provide a better estimate of the field because the line is gravitationally redshifted by an unknown amount. The precise determination of the surface field, as well as the gravitational redshift, would be aided by the identification of another type of line.

Because gamma-ray bursts are very energetic events, with a typical energy flux estimated to be $\sim 10^{37} \left(\frac{d}{100\text{pc}}\right)^2$erg/s, where d is the distance to the source, it is reasonable to expect that the emitting region will contain highly ionized atoms. If the atomic number Z of these atoms is high enough, atomic absorption of photons will produce absorption features in the 1-10keV range. Since the energies of these features and the energies of cyclotron lines scale differently with magnetic field (see Section 2), identification of these lines would uniquely determine the magnetic field and gravitational redshift at the emitting region. This could, in turn, give valuable clues about the equation of state and evolution of neutron stars. The determination of lines in gamma-ray bursts would be similar to the attempted identification of the 4.1keV absorption feature in the X-ray burster MXB 1636-536 by Ebisuzaki (1987). In this paper, Ebisuzaki attempted to fit helium-like iron, chromium and titanium (calculated for zero magnetic field) to this feature, and thus deduce the gravitational

redshift. However, in gamma-ray bursts and some X-ray bursters such as Her X-1, the magnetic field will shift the lines and thus complicate the identification process.

In order to assist with the determination of atomic absorption lines in events such as gamma-ray bursts, this paper gives the energies of various states of several highly ionized atoms in a few strong magnetic fields. While it may be likely that iron, with $Z = 26$, will dominate the surface (because it is the equilibrium nucleus at zero pressure), other values of Z have been considered for illustrative purposes. In Section 2 the method used to generate these energies is briefly stated and some of the important parameters and scaling laws in very strong magnetic fields are covered. In addition, the results are given and the errors are estimated. Finally, Section 3 presents the conclusions.

2. Approximations and method

2.1 Scaling laws

In this paper, the magnetic field is assumed to be large, so the electrons move in Landau orbits around the field, and the nucleus acts as a perturbation. Therefore, the wavefunction of an atom may be approximated as a thin cylinder, with the long axis along the field. Accordingly, a cylindrical coordinate system is set up, with ρ being the radial coordinate, ϕ being the azimuthal coordinate, and z being the coordinate along the field. The quantum numbers for these coordinates are, respectively, n, m and ν.

This approximation is valid when the magnetic field greatly exceeds a critical field, with the critical field defined as the field at which the magnetic force and Coulomb force are equal. This depends on the state that the electron is in, and is given by (Miller and Neuhauser 1990)

$$B_m \approx \frac{Z^2}{(2m+1)^3} B_C, \tag{1}$$

where $B_C = 2.35 \times 10^9$G is the critical field for the ground state of hydrogen. The cylindrical approximation is truly valid only for $B \gg B_m$, but in practice it gives fair accuracy for $B > B_m$. The scaling of this formula means that for Rydberg states $m \gg 1$ the high-field approximation is valid even for very magnetic white dwarfs, $B \sim 10^8$G. It also means that for $B = 5 \times 10^{12}$G, which is the field strength inferred from some cyclotron lines from X-ray pulsars, even iron ($Z = 26$) may be treated in the high-field limit. For the rest of this paper the reference shall be taken to be $B_0 \equiv 4.7 \times 10^9\text{G} = 2B_C$, in accordance with tradition.

A hydrogenic electron in its ground state $n = m = \nu = 0$ in the limit $B \to \infty$ has a binding energy that is approximately given by (Ruderman 1970)

$$E \sim -Z^2 \frac{\hbar^2}{M a_0^2} \ln^2 \left(\frac{a_0}{Z\hat{\rho}} \right) \tag{2}$$

(Ruderman 1971) where

Z is the atomic number,

M is the mass of the electron,

a_0 is the Bohr radius, $a_0 \approx 5 \times 10^{-9}$cm, and

$\hat{\rho}$ is the length scale across the field, $\hat{\rho} = \left(\frac{\hbar c}{eB} \right)^{1/2} \approx 2.5 \times 10^{-10} B_{12}^{-1/2}$cm, where $B_{12} = \frac{B}{10^{12}\text{G}}$. A state with $\nu > 0$ has roughly constant energy (Landau and Lifshitz 1977), so that, for example, the energy of a $\nu = 1$ state of hydrogen is about 10-13eV regardless of magnetic field, once the critical field is exceeded.

2.2 Method and results

The results in this paper were generated with a high-field multiconfigurational Hartree-Fock method. This method was described in detail in Miller and Neuhauser 1990 (hereafter referred to as MN), and I will not repeat that analysis. However, some of the basic points are worth restating. The wavefunction of an atom is expanded in a cylindrical basis:

$$\Psi_{m\nu}(z, \rho, \phi) = \sum_n f_{nm\nu}(z) \Phi_{nm}(\rho, \phi), \tag{3}$$

where the Φ_{nm} are the Landau states,

$$\Phi_{nm}(\rho,\phi)=\frac{\sqrt{n!}}{\sqrt{2\pi(n+|m|)!\hat{\rho}^2}}\Big(\frac{\rho}{\sqrt{2}\hat{\rho}}\Big)^{|m|}e^{-\rho^2/4\hat{\rho}^2}L_n^{|m|}\Big(\frac{\rho^2}{2\hat{\rho}}\Big)e^{-im\phi} \qquad (4)$$

and $L_n^{|m|}$ are the associated Laguerre polynomials. In the limit $\beta=\frac{B}{B_m}\gg 1$, the $n>0$ states contribute little because the energy required to excite an atom to an $n>0$ state is $11.5\mathrm{keV}nB_{12}$, which is much greater than the binding energy for $\beta\gg 1$ (Rösner *et al.* 1984). Thus, in MN and this paper the assumption has been made that $n=0$. However, for the atomic numbers and magnetic fields considered in this paper, this assumption is not always good. For example, for $Z=28$ and $B=10^{12}\mathrm{G}$, $\beta\approx 0.2$ for the $m=\nu=0$ state of hydrogen. Therefore, mixing of $n>0$ states is important for $m=\nu=0$.

Since it is difficult to get an analytic estimate of the errors incurred using the $n=0$ approximation, an attempt has been made to estimate the error in the energies of the $m=\nu=0$ states of atoms by comparing my results for hydrogenic atoms with those of Rösner et al. 1984, which is done using the scaling formula

$$E(B,Z)=Z^2E(B/Z^2,1). \qquad (5)$$

Since Rösner et al. 1984 did full expansions with $n>0$, their results are highly accurate and may be taken as the standard against which all high-field hydrogenic calculations must be tested. Since the major determinant of error in my calculations is the parameter β (see MN for a discussion), the errors for hydrogenic atoms are the errors one would expect for the $m=\nu=0$ state of any atom. Similarly, the values for the energy of the $m=0$, $\nu=1$ state of hydrogen have been compared with Rösner et al. 1984. Because in this state the electron is, on the average, much farther from the nucleus than it is in the ground state (as it is for any $m>0$ or $\nu>0$ state), the effective β is much higher, and the approximations used in this paper are better.

The energies were determined by an integration over a one- dimensional integration box of length L with a number of grid points N. The results presented here were calculated with $N = 1024$, $L = 100\hat{\rho}$ for the $\nu = 0$ states and $N = 1024$, $L = 400\hat{\rho}$ for the $\nu = 1$ states. Table 1 gives the binding energies of the ground and first excited states in several magnetic fields for hydrogen-like silicon, chromium, iron, cobalt and nickel. The numbers in parentheses are the extrapolated values of Rösner et al. 1984, and linear interpolation was used between the values given in their tables. It can be seen that for $B = 10^{12}$G the ground-state energies are accurate only to within $\sim 20\%$, while at 10^{13}G they deviate from Rösner et al. 1984 by only 6%. However, the excited state $m = 0$, $\nu = 1$ has much greater accuracy, with a maximum difference $< 4\%$ and a typical agreement better than 1%. Tables 2a, 2b and 2c give the binding energies of the helium-like ground state and two excited states of the same elements in the same fields, and here the total energy of the atom (i.e. the energy necessary to ionize it completely) is also given.

3. Conclusions

If gamma-ray bursts are observed by detectors with good resolution in the energy range 1keV-100keV, it is possible that the detections of cyclotron lines and atomic lines may allow reasonably accurate estimates of the magnetic field and gravitational redshift of the neutron star. This paper has presented the energies of some highly ionized states of atoms in various magnetic fields, and if the magnetic field is large ($B > 5 \times 10^{12}$G), these numbers will allow for a reasonably precise (10%) determination of the parameters B and $1 + z$. However, for smaller fields ($B \sim 1 \times 10^{12}$G) and high atomic number ($Z > 20$) it is necessary to consider the mixing of $n > 0$ states for accuracy better than 25%.

It may be quite difficult to determine the atomic number from the positions of the lines, especially if only one or two atomic lines are detected. If cyclotron lines

are also detected, it will be possible to set limits on the magnetic field, and thus the atomic number. However, as is apparent from the tables, atoms with similar atomic number have very similar line structures, and exceptional energy resolution would be required to differentiate between, for example, iron (Z=26) and cobalt (Z=27). Thus, it may be necessary to make assumptions about the surface composition to determine the redshift and magnetic field.

References

Ebisuzaki, T. 1987, *Publ. Astron. Soc. Japan*, **39**, 287.

Golenetskii, S. V., Guryan, Yu. a., Dumov, G. B., Dyatchkov, A. V. *et al.* 1986. Preprint 1026, Fiz. Tekh. Inst. Ioffe, 31pp. Leningrad: Akad. Nauk SSSR.

Mazets, E. P., Golenetskii, S. V., Aptekar, R. L., Guryan, Yu. A., and Illinskii, V. N. 1981, *Nature*, **290**, 378.

Miller, M. C., and Neuhauser, D. 1990, California Institute of Technology, preprint.

Murakami, T. *et al.* 1988, *Nature*, **335**, 234.

Rösner, W., Wunner, G., Herold, H., and Ruder, H. 1984, *J. Phys. B: At. Mol. Phys.*, **17**, 29.

Ruderman, M. A. 1971 *Phys. Rev. Lett.*, **27**, 1306.

Table 1

Binding energies of hydrogen-like atoms in strong fields. The states are labelled by their m-value, then their nu-value. The energies in parentheses are the extrapolated values of Rosner et al. 1984.

		Energies (eV)		Zero field values (eV)	
Z	B(G)	00	01	00	01
14	1e12	4955(5579)	1596(1606)	2666	666
	2e12	6491(6999)	1805(1809)		
	3e12	7576(8018)	1922(1921)		
	5e12	9170(9562)	2059(2056)		
	1e13	11802(12079)	2221(2216)		
24	1e12	9439(11961)	3716(3801)	7834	1958
	2e12	12496(14568)	4340(4394)		
	3e12	14680(16495)	4708(4736)		
	5e12	17922(19509)	5165(5183)		
	1e13	23346(24522)	5750(5731)		
26	1e12	10373(13518)	4197(4328)	9194	2298
	2e12	13753(16293)	4923(4994)		
	3e12	16172(18431)	5355(5402)		
	5e12	19767(21725)	5895(5924)		
	1e13	25794(27372)	6595(6598)		
27	1e12	10844(14324)	4443(4598)	9914	2479
	2e12	14387(17183)	5222(5304)		
	3e12	16925(19395)	5688(5737)		
	5e12	20698(22858)	6272(6306)		
	1e13	27031(28807)	7033(7044)		
28	1e12	11317(15130)	4692(4862)	10662	2666
	2e12	15025(18107)	5527(5625)		
	3e12	17682(20396)	6027(6085)		
	5e12	21636(23961)	6657(6684)		
	1e13	28277(30163)	7481(7483)		

Table 2a

Binding energies of the 00,10 state of helium-like atoms in strong fields. The states are labelled by their m-value, then their nu-value. The zero-field values for silicon and chromium were taken from Bashkin and Stoner, "Atomic Energy Levels and Grotrian Diagrams", 1975 (New York:Elsevier).

		Energies(eV)			Zero field values(eV)	
Z	B(G)	total	00	10	00	10
14	1e12	7946	4761	2991	2438	2438
	2e12	10465	6229	3975		
	3e12	12254	7265	4678		
	5e12	14894	8785	5724		
	1e13	19276	11290	7475		
24	1e12	15163	9233	5724	7482	7482
	2e12	20182	12216	7686		
	3e12	23786	14345	9106		
	5e12	29159	17503	11237		
	1e13	38203	22783	14856		
26	1e12	16661	10166	6288		
	2e12	22208	13470	8455		
	3e12	26198	15833	10026		
	5e12	32154	19343	12387		
	1e13	42198	25223	16405		
27	1e12	17415	10636	6571		
	2e12	23230	14103	8842		
	3e12	27414	16584	10489		
	5e12	33665	20273	12966		
	1e13	44217	26458	17186		
28	1e12	18173	11108	6856		
	2e12	24256	14740	9231		
	3e12	28636	17340	10954		
	5e12	35185	21209	13549		
	1e13	46249	27701	17972		

Table 2b

Binding energies of the 01,10 state of helium-like atoms in strong fields. The states are labelled by their m-value, then their nu-value. The zero-field values for silicon and chromium were taken from Bashkin and Stoner, "Atomic Energy Levels and Grotrian Diagrams", 1975 (New York:Elsevier).

			Energies(eV)		Zero field values(eV)	
Z	B(G)	total	01	10	01	10
14	1e12	4631	1446	3037	573	2100
	2e12	5857	1621	4054		
	3e12	6705	1716	4786		
	5e12	7933	1824	5879		
	1e13	9935	1949	7720		
24	1e12	9467	3538	5752	1793	6000
	2e12	12079	4114	7740		
	3e12	13890	4450	9183		
	5e12	16517	4862	11354		
	1e13	20801	5384	15055		
26	1e12	10509	4015	6313		
	2e12	13427	4690	8506		
	3e12	15452	5089	10099		
	5e12	18391	5583	12498		
	1e13	23187	6215	16595		
27	1e12	11037	4259	6595		
	2e12	14112	4987	8891		
	3e12	16246	5419	10560		
	5e12	19345	5955	13075		
	1e13	24403	6646	17373		
28	1e12	11570	4507	6879		
	2e12	14803	5289	9278		
	3e12	17049	5754	11023		
	5e12	20310	6335	13655		
	1e13	25632	7087	18155		

Table 2c

Binding energies of the 00,11 state of helium-like atoms in strong fields. The states are labelled by their m-value, then their nu-value. The zero-field values for silicon and chromium were taken from Bashkin and Stoner, "Atomic Energy Levels and Grotrian Diagrams", 1975 (New York:Elsevier).

		Energies (eV)			Zero field values (eV)	
Z	B(G)	total	00	11	00	11
14	1e12	6105	4782	1188	2100	573
	2e12	7824	6282	1376		
	3e12	9013	7344	1485		
	5e12	10733	8908	1615		
	1e13	13518	11497	1776		
24	1e12	12123	9185	2775	6000	1793
	2e12	15726	12187	3333		
	3e12	18243	14333	3674		
	5e12	21910	17524	4111		
	1e13	27900	22872	4696		
26	1e12	13396	10102	3127		
	2e12	17410	13423	3774		
	3e12	20218	15802	4173		
	5e12	24314	19342	4688		
	1e13	31016	25287	5384		
27	1e12	14040	10564	3306		
	2e12	18262	14047	3999		
	3e12	21218	16544	4429		
	5e12	25533	20261	4984		
	1e13	32599	26508	5739		
28	1e12	14687	11029	3488		
	2e12	19120	14674	4228		
	3e12	22227	17298	4688		
	5e12	26763	21185	5285		
	1e13	34197	27738	6101		